Title 40 CFR Part 191
Compliance Certification
Application
for the
Waste Isolation Pilot Plant

Appendix TFIELD

United States Department of Energy
Waste Isolation Pilot Plant

Carlsbad Area Office
Carlsbad, New Mexico

Generation of an Ensemble of Culebra Transmissivity Fields Conducted to Steady-State and Transient Pressure Data Using GRASP-INV

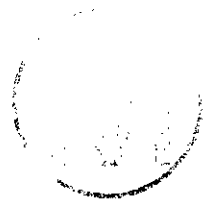

CONTENTS

FIGURES

TABLES

ACRONYMS

2-D	two-dimensional
3-D	three-dimensional
amsl	above mean sea level
CCDF	complementary cumulative distribution function
CDF	cumulative distribution function
CS	conditionally simulated
DST	drill stem tests
iCs	indicator categorical simulation
IK	indicator kriging
MG	multiGaussian
OK	ordinary kriging
PA	performance assessment
RF	random function
RV	random variable
sGs	sequential Gaussian simulation
SK	simple kriging
TFIELD	transmissivity field
UTM	universal transverse merator
WIPP	Waste Isolation Pilot Plant

1 THIS PAGE INTENTIONALLY LEFT BLANK

APPENDIX TFIELD

TFIELD.1 Introduction

Major sources of data for the Waste Isolation Pilot Plant (WIPP) performance assessment calculations are the results of site-characterization activities, which began at the WIPP site in 1976. Since 1983, when full construction of the facility was started, site-characterization activities have had the objectives of updating or refining the overall conceptual models of the geologic, hydrologic, and structural behavior of the WIPP site and providing data adequate for use in the WIPP performance assessment (Lappin 1988; see Appendix SUM). This appendix addresses the conceptual model and data used by the U.S. Department of Energy (DOE) for transmissivity variation in the Culebra member of the Rustler Formation (hereafter referred to as the Culebra), an important factor in groundwater flow and transport. Because some uncertainty about the parameters controlling groundwater flow and transport will always remain, the WIPP performance assessment calculations employ Monte Carlo techniques to address this uncertainty. This approach requires that cumulative distribution functions be selected for numerous imprecisely known input parameters. An input parameter needed to simulate far-field flow and transport through the Culebra, which the DOE considers to be the principal pathway for offsite transport, is transmissivity. This appendix focuses on the theory and application of a numerical model, GRASP-INV, used to generate transmissivity fields for the Culebra for use in the performance assessment calculations.

GRASP-INV is used to generate and subsequently calibrate conditionally simulated (CS) transmissivity fields. Because each CS field has similar broad features but distinctly different small-scale variations, the GRASP-INV code produces numerous, equally probable, transmissivity fields calibrated to the observed head data. The unique features present within each calibrated field are related to the uncertainty of the transmissivity field. The DOE has incorporated this uncertainty into the Monte Carlo analysis by drawing one field for each system calculation by sampling.

The objectives of this appendix are (1) to describe the analysis of the pertinent Culebra hydrogeologic data used to develop the initial model parameters, (2) to present the methodology used to generate the transmissivity fields, and (3) to discuss the results of the application of GRASP-INV.

TFIELD.2 Site Description

TFIELD.2.1 WIPP Site Description

The WIPP site lies within the geologic region known as the Delaware Basin. The upper seven formations present at or in the vicinity of the WIPP site are, in descending order, the Gatuña Formation, the Dockum Group, the Dewey Lake Red Beds, the Rustler Formation, the Salado Formation, the Castile Formation, and the Bell Canyon Formation (hereafter referred to as the Gatuña, the Dockum, the Dewey Lake, the Rustler, the Salado, the Castile, and the Bell

Canyon, respectively) (Figure TFIELD-1). The repository horizon lies within the bedded salt of the Salado.

The Rustler consists of beds of halite, siltstone, anhydrite, and dolomite. It is divided into five separate members based on lithology. The Culebra, one of these five members, has been identified through extensive field site-characterization efforts as the most transmissive, laterally continuous hydrogeologic unit above the Salado and is considered to be the principal pathway for offsite radionuclide transport in the subsurface following drilling and abandonment of a borehole intruding through the waste. Based upon observations of outcrops, core, and detailed shaft mapping, the Culebra can be characterized, at least locally, as a fractured medium at the WIPP site. As the amount of fracturing and development of secondary porosity increases, the Culebra transmissivity generally increases. The occurrence of enhanced transmissivity zones due to fracturing was shown to have an important effect on groundwater velocities by LaVenue and RamaRao (1992). Thus, distinguishing the zones in the model domain where transmissivity has not been affected by fracturing and is therefore low, from the zones where the transmissivity has been increased as a result of fracturing, is one of the primary objectives of this modeling exercise.

TFIELD.2.2 Culebra Hydrologic Data

Over the past 16 years, a significant effort has been directed toward field investigations at the WIPP site. Numerous boreholes in and immediately surrounding the WIPP-site area have been drilled and tested within the Culebra in support of these investigations (Figure TFIELD-2). From these boreholes, estimates for hydrogeologic parameters such as formation elevation, transmissivity, fluid density, and storativity have been obtained. In addition, an exhaustive set of water-level measurements for hydraulically undisturbed conditions as well as hydraulically disturbed conditions (that is, transient hydraulic tests) has been recorded. The field investigations have been instrumental in providing estimates of the variability of the hydrogeologic properties within the Culebra. The following sections will review the data that have been obtained from the field program and qualified under the Sandia National Laboratory Quality Assurance Program.

TFIELD.2.2.1 Culebra Elevation Data

The elevation of the Culebra has been documented in Cauffman et al. (1990). It contains the ground-surface elevations and the depths to the Culebra from which the Culebra elevations at the borehole locations in the WIPP area were calculated. Table TFIELD-1 contains an augmented list of the Culebra elevations used in this model. The Culebra, which dips toward the southeast (Figure TFIELD-3), has spatially varying characteristics across the WIPP-site area. The elevations of the center of the Culebra range from approximately 1970 feet (600 meters) above mean sea level (amsl) northeast of the WIPP site to approximately 3180 feet (970 meters) amsl northwest of the WIPP site.

System	Series	Group	Formation	Member
Recent	Recent		Surficial Deposits	
Quaternary	Pleistocene		Mescalero Caliche	
			Gatuña	
Triassic		Dockum	Undivided	
Permian	Ochoan		Dewey Lake Redbeds	
			Rustler	Forty-niner
				Magenta Dolomite
				Tamarisk
				Culebra Dolomite
				unnamed
			Salado	
			Castile	
	Guadalupian	Delaware Mountain	Bell Canyon	
			Cherry Canyon	
			Brushy Canyon	

CCA-TFI001-0

Figure TFIELD-1. Geologic Column Representative of WIPP Area (after Powers et al. 1978)

THIS PAGE INTENTIONALLY LEFT BLANK

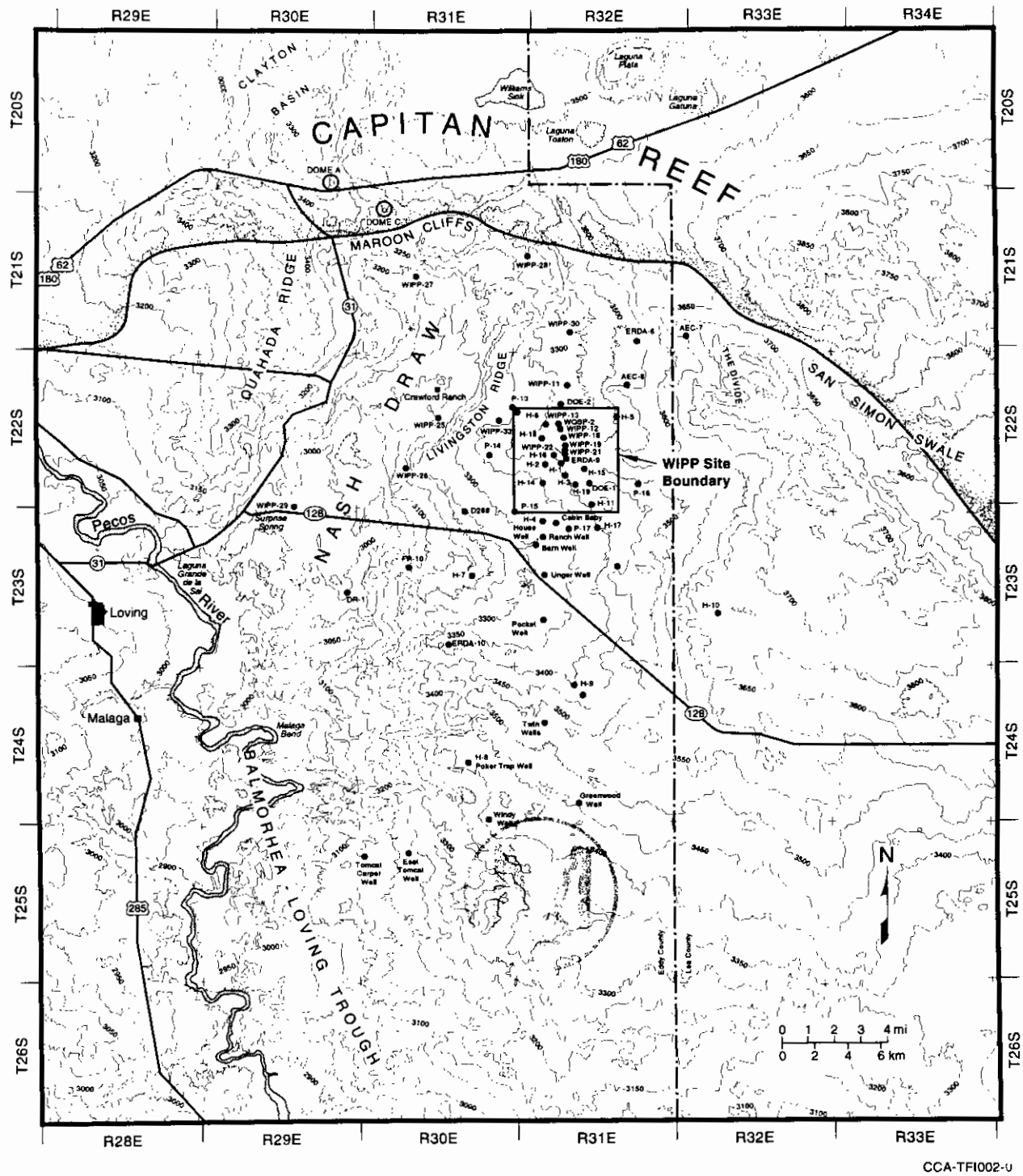

Figure TFIELD-2. Map of WIPP Site and Surrounding Area

1 THIS PAGE INTENTIONALLY LEFT BLANK

Table TFIELD-1. Center of Culebra Elevations

UTM E (meter)	UTM N (meter)	Elevation (m amsl)	Borehole
613423.	3581684.	826.13	H-1
612663.	3581641.	836.31	H-2A
612651.	3581651.	836.56	H-2B1
612661.	3581649.	836.25	H-2B2
612666.	3581668.	836.58	H-2C
613729.	3580895.	825.17	H-3B1
613701.	3580906.	823.37	H-3B2
613705.	3580876.	824.07	H-3B3
612407.	3578469.	861.01	H-4A
612380.	3578483.	862.48	H-4B
612406.	3578499.	862.73	H-4C
616888.	3584776.	791.58	H-5A
616872.	3584801.	791.53	H-5B
616903.	3584802.	790.74	H-5C
610580.	3584982.	832.64	H-6A
610594.	3585008.	832.73	H-6B
610610.	3584983.	832.84	H-6C
608124.	3574648.	886.37	H-7B1
608095.	3574640.	886.33	H-7C
608683.	3563556.	863.16	H-8B
608664.	3563537.	862.96	H-8C
613958.	3568260.	836.38	H-9A
613989.	3568261.	836.43	H-9B
613974.	3568234.	836.53	H-9C
622975.	3572473.	705.07	H-10B
622976.	3572443.	704.89	H-10C
615346.	3579130.	813.21	H-11B1
615348.	3579107.	812.67	H-11B2
615367.	3579127.	812.46	H-11B3
615313.	3579131.	815.44	H-11B4

Table TFIELD-1. Center of Culebra Elevations (Continued)

UTM E (meter)	UTM N (meter)	Elevation (m amsl)	Borehole
617023.	3575452.	789.27	H-12
612341.	3580354.	849.47	H-14
615315.	3581859.	794.98	H-15
613369.	3582212.	821.79	H-16
615718.	3577513.	812.42	H-17
612264.	3583166.	826.82	H-18
614514.	3580718	812.30	H-19
615203.	3580333.	802.72	DOE-1
613683.	3585294.	787.38	DOE-2
612338.	3580341.	851.40	P-1
615316.	3581848.	794.82	P-2
612799.	3581898.	831.81	P-3
614935.	3580319.	808.57	P-4
613685.	3583535.	809.64	P-5
610609.	3581084.	855.02	P-6
612308.	3578478.	860.36	P-7
613830.	3578467.	841.49	P-8
615356.	3579125.	811.67	P-9
617087.	3581203.	781.67	P-10
617016.	3583457.	786.66	P-11
610456.	3583452.	832.56	P-12
610531.	3585029.	832.10	P-13
609084.	3581976.	846.05	P-14
610624.	3578747.	879.58	P-15
612695.	3577321.	856.89	P-16
613926.	3577466.	842.85	P-17
618367.	3580350.	777.64	P-18
617681.	3582418.	781.59	P-19
618532.	3583768.	788.46	P-20
616898.	3584849.	792.07	P-21

Table TFIELD-1. Center of Culebra Elevations (Continued)

UTM E (meter)	UTM N (meter)	Elevation (m amsl)	Borehole
613791.	3586475.	783.49	W-11
613710.	3583524.	807.35	W-12
612644.	3584247.	820.79	W-13
613735.	3583179.	810.43	W-18
613739.	3582782.	812.47	W-19
613743.	3582319.	815.68	W-21
613739.	3582653.	814.67	W-22
606385.	3584028.	839.10	W-25
604014.	3581162.	900.45	W-26
604426.	3593079.	875.43	W-27
611266.	3594680.	888.07	W-28
596981.	3578694.	899.14	W-29
613721.	3589701.	849.01	W-30
621126.	3589381.	845.59	AEC-7
617525.	3586442.	818.74	AEC-8
618220.	3589008.	858.83	ER-6
613696.	3581958.	820.92	ER-9
606685.	3570515.	878.15	ER-10
613191.	3578049.	856.88	CB-1
614953.	3567454.	837.78	ENGLE
606462.	3569415.	881.66	USGS1
605841.	3569887.	892.19	USGS4
605879.	3569888.	894.13	USGS8
608702.	3578877.	883.32	D-268
607461.	3590055.	883.94	FFG-107
599239.	3572224.	905.80	FFG-153
601859.	3573206.	907.16	FFG-165
604215.	3568693.	926.54	FFG-181
603881.	3562585.	841.50	FFG-188
629277.	3596967.	599.54	FFG-225

Table TFIELD-1. Center of Culebra Elevations (Continued)

UTM E (meter)	UTM N (meter)	Elevation (m amsl)	Borehole
620854.	3597026.	678.74	FFG-236
627179.	3589332.	717.34	FFG-244
592523.	3591566.	922.94	FFG-426
595800.	3585222.	961.21	1-DANF
601312.	3588916.	969.23	1-DUNC
612561.	3583427.	825.61	WQSP-1
613776.	3583973.	805.28	WQSP-2
614686.	3583518.	799.52	WQSP-3
614728.	3580766.	809.18	WQSP-4
613668.	3580353.	830.03	WQSP-5
612605.	3580736.	844.39	WQSP-6

TFIELD.2.2.2 Culebra Fluid-Density Data

The fluid-density data deemed representative of the Culebra were described by Cauffman et al. (1990). These data are repeated in Table TFIELD-2. Densities ranging from 1.00 to 1.03 grams per cubic centimeter occur in a wide region extending from boreholes WIPP-28 to H-7 (Figure TFIELD-4). Higher fluid densities are located east of this region with values ranging from 1.04 to 1.16 grams per cubic centimeter (Figure TFIELD-4).

In this model, formation-fluid densities are assigned to grid blocks and held constant over the 15-year simulation. Thus, in the simulation, the formation-fluid densities appear to represent steady-state conditions. It should be noted that geochemical investigations (Lambert and Harvey 1987; Chapman 1986; Lambert and Carter 1987; and Lambert 1987) suggest that the chemical constituents within the Culebra flow field are currently not at steady state. However, the time period for reaching steady state is considered to be several thousand years. Thus, for a small unit of time, such as 15 years, the fluid-density conditions would appear to be fixed. Conceptually, one may consider this phenomenon similar to the flow of glass in a window, which will shift over many years, yet seems fixed on a daily basis. Therefore, the decision was made to hold formation-fluid densities constant over the simulation time period.

The decision to assign a fluid-density value to each grid block (rather than using one value for all) also meant that the effects of variable fluid densities on the present-day flow field (that is, the calculated pressures and Darcy velocities) were included in the Culebra transmissivity fields produced by GRASP-INV.

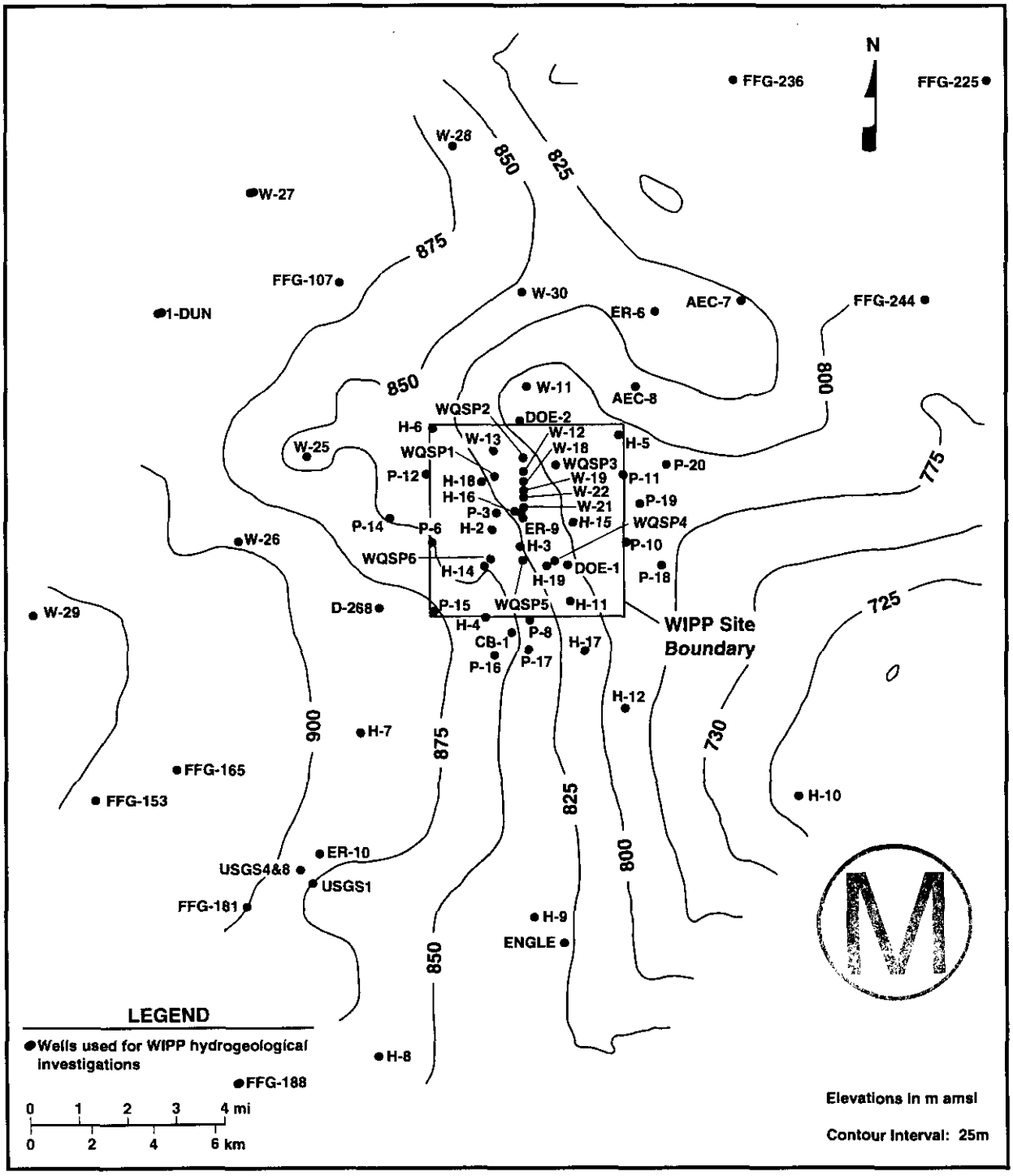

CCA-TFI003-0

Figure TFIELD-3. Center-of-Culebra Elevations at the WIPP Area Boreholes

1 THIS PAGE INTENTIONALLY LEFT BLANK

Table TFIELD-2. Culebra-Fluid Density and Transmissivity Values

UTM E (meters)	UTM N (meters)	Fluid Density (grams per cubic meter)	Log_{10} Transmissivity (log_{10} meters per square second)	Borehole
613423.	3581684.	1.022	-6.03	H-1
612651.	3581651.	1.006	-6.07	H-2
613729.	3580895.	1.035	-5.62	H-3
612380.	3578483.	1.014	-6.01	H-4
616872.	3584801.	1.102	-6.67	H-5
610594.	3585008.	1.038	-4.40	H-6
608124.	3574648.	1.000	-3.05	H-7
608683.	3563556.	1.000	-5.05	H-8
613989.	3568261.	1.000	-3.97	H-9
622975.	3572473.	1.047	-6.11	H-10
615346.	3579130.	1.078	-4.06	H-11
617023.	3575452.	1.095	-6.71	H-12
612341.	3580354.	1.010	-6.49	H-14
615315.	3581859.	1.154	-6.85	H-15
613369.	3582212.	NA	-6.07	H-16
615718.	3577513.	1.100	-6.63	H-17
612264.	3583166.	1.017	-5.73	H-18
614514.	3580718.	1.067	-5.54	H-19
609084.	3581976.	1.018	-3.41	P-14
610624.	3578747.	1.015	-7.01	P-15
613926.	3577466.	1.061	-5.97	P-17
618367.	3580350.	NA	-10.12	P-18
613710.	3583524.	NA	-6.98	W-12
612644.	3584247.	1.046	-4.13	W-13
613735.	3583179.	NA	-6.49	W-18
613739.	3582782.	1.059	-6.19	W-19
613743.	3582319.	NA	-6.57	W-21
613739.	3582653.	NA	-6.40	W-22
606385.	3584028.	1.009	NA	W-25

Table TFIELD-2. Culebra-Fluid Density and Transmissivity Values (Continued)

UTM E (meters)	UTM N (meters)	Fluid Density (grams per cubic meter)	Log_{10} Transmissivity (log_{10} meters per square second)	Borehole
604014.	3581162.	1.009	NA	W-26
604426.	3593079.	NA	-3.67	W-27
611266.	3594680.	1.032	-3.59	W-28
613721.	3589701.	1.018	-6.73	W-30
614953.	3567454.	1.001	-4.34	ENGLE
606462.	3569459.	1.000	-3.26	USGS1
605841.	3569887.	1.000	NA	USGS4
605879.	3569888.	1.000	NA	USGS8
615203.	3580333.	1.088	-4.93	DOE-1
613683.	3585294.	1.041	-4.02	DOE-2
612561.	3583427.	1.053	-4.48	WQSP-1
613776.	3583973.	1.06	-4.93	WQSP-2
614686.	3583518.	1.14	NA	WQSP-3
614728.	3580766.	1.08	-5.28	WQSP-4
613668.	580353.	1.03	-5.93	WQSP-5
612605.	580736.	1.019	-6.67	WQSP-6
621126.	3589381.	NA	-6.76	AEC-7
613696.	3578049.	NA	-6.52	CB-1
608702.	3578877.	NA	-5.67	D-268
613696.	3581958	NA	-6.31	ER-9

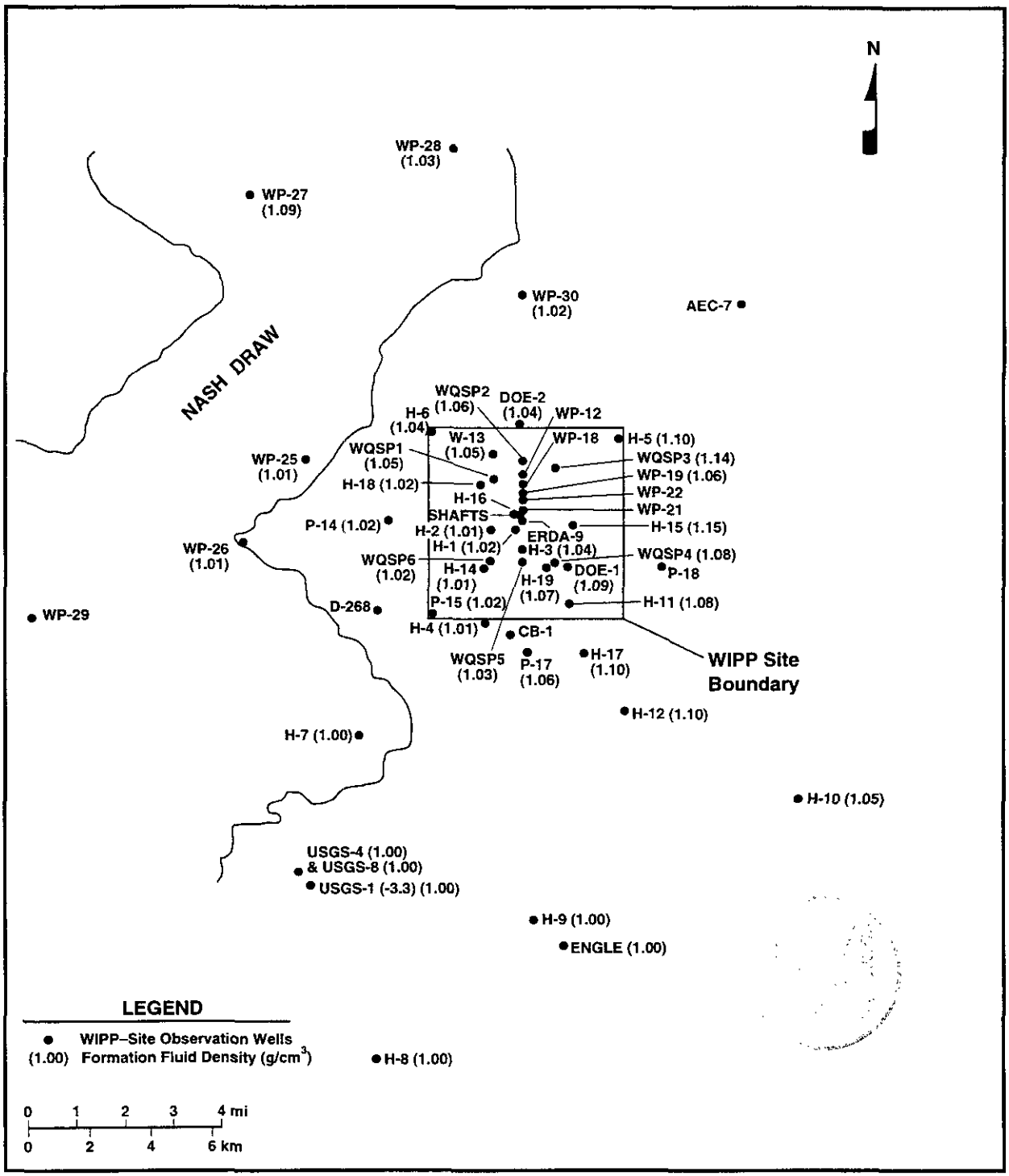

CCA-TFI004-0

Figure TFIELD-4. Culebra Fluid-Density Values at the WIPP Area Boreholes

1 THIS PAGE INTENTIONALLY LEFT BLANK

TFIELD.2.2.3 Culebra Transmissivity and Storativity Data

The transmissivity data base for the Culebra is derived from numerous hydraulic tests performed at the WIPP site. Values have been obtained from drill-stem tests (DSTs), slug tests, and local- and regional-scale pumping or interference tests (Beauheim 1986, 1987a, 1987b, 1987c, 1989, 1996; Beauheim et al. 1991; Cooper 1962; Cooper and Glanzman 1971). Transmissivity values interpreted from these tests extend over a range of seven orders of magnitude (Table TFIELD-2 and Figure TFIELD-5). The uncertainty of the transmissivity data has been estimated to be ± 0.3 ($\log_{10}$ meters per square second). This value is used in this model to assign limits on the permissible changes to the transmissivity field during model calibration.

The lack of numerous storativity data eliminated the possibility of spatially varying storativity in the model domain. The storativity data that were obtained from the tests within the Culebra were therefore used to determine a mean storativity (1×10^{5}) for the entire area.

TFIELD.2.2.4 Culebra Freshwater Head Data

Data from the observation-well network in the Culebra were evaluated in Cauffman et al. (1990) to characterize the hydraulic conditions in the Culebra. Appendix G of Cauffman et al. (1990) presents the hydrographs plotted as equivalent freshwater head versus time. The freshwater-head data were calculated from either depth-to-water or downhole-pressure-transducer measurements. The procedure used and the information necessary to calculate the freshwater heads are also presented in Appendix G of Cauffman et al. (1990). An example of the hydrograph for Well H-1 is shown in Figure TFIELD-6.

Cauffman et al. (1990) estimated the undisturbed hydraulic conditions and the transient responses to construction of the shafts and regional-scale pumping tests in the Culebra from these hydrographs. In addition, they presented the uncertainty associated with each selected undisturbed head, which was calculated by summing the measurement error of the parameters used to calculate freshwater head (for example, the accuracy of the water-level measuring device, the accuracy of the ground-surface elevation survey, and the uncertainty of the borehole fluid-column density). However, the uncertainties associated with the selected heads did not account for unexplained trends in the hydrographs. For example, in Figure TFIELD-6, a 3.4-m rising trend occurs between 1977 and the middle of 1981.

For this study, the undisturbed heads were reselected so that these trends could be included directly in the uncertainty associated with each head value. In essence, the heads were reselected so that the head value used in the 1996 performance assessment would be centered in the middle of any unexplained trend. The range (minimum and maximum) of the trend was then considered to represent the 99 percent confidence interval ($\pm 3\sigma$) and converted to an uncertainty value. The uncertainty due to the trend was added to the uncertainty presented in

Cauffman et al. (1990) to obtain a centered or symmetrical uncertainty value associated with each selected head value.

For example, in Figure TFIELD-6, the undisturbed head selected by Cauffman et al. (1990) was 923.3 meters on July 1981. However, in 1977, the head at H-1 was approximately 920 meters and rising (Figure TFIELD-6). Because the uncertainty associated with the preshaft (that is, pre-August 1981) hydraulic conditions at H-1 should include the 3.4-meters upward trend in the heads, a readjustment of the Cauffman et al. selected head value was needed. Therefore, the selected head at H-1 (923.3 meters) was readjusted so that it lay in the center of the 3.4-meters rising trend (921.6 meters) (Figure TFIELD-6). The range of this trend (3.4 meters) was used to calculate a standard deviation associated with the adjusted head value. The head and standard deviation were calculated as follows:

Head:

Cauffman et al. (1990) Head + Adjustment = 1996 Head

$$9.23.3\text{m} - \frac{3.4\text{m}}{2} = 921.6\,\text{m}$$

Standard Deviation:

Head Range = Trend Range + Measurement Error Range

$= 3.4\text{ m} + 2(2.0\text{ m})$

$= 7.4\text{ m} = 6\sigma$

where σ = head value standard deviation.

$$\sigma = \frac{7.4\text{m}}{6} = 1.23\,\text{m}$$

Overall Head Variance: $\sigma^2 = 1.5$

Head Weight: $\frac{1}{\sigma 2} = \frac{1}{1.5} = 0.7$

Note: The weights are assigned to the head values during steady-state model calibration to weight the more certain heads higher than the less certain heads.

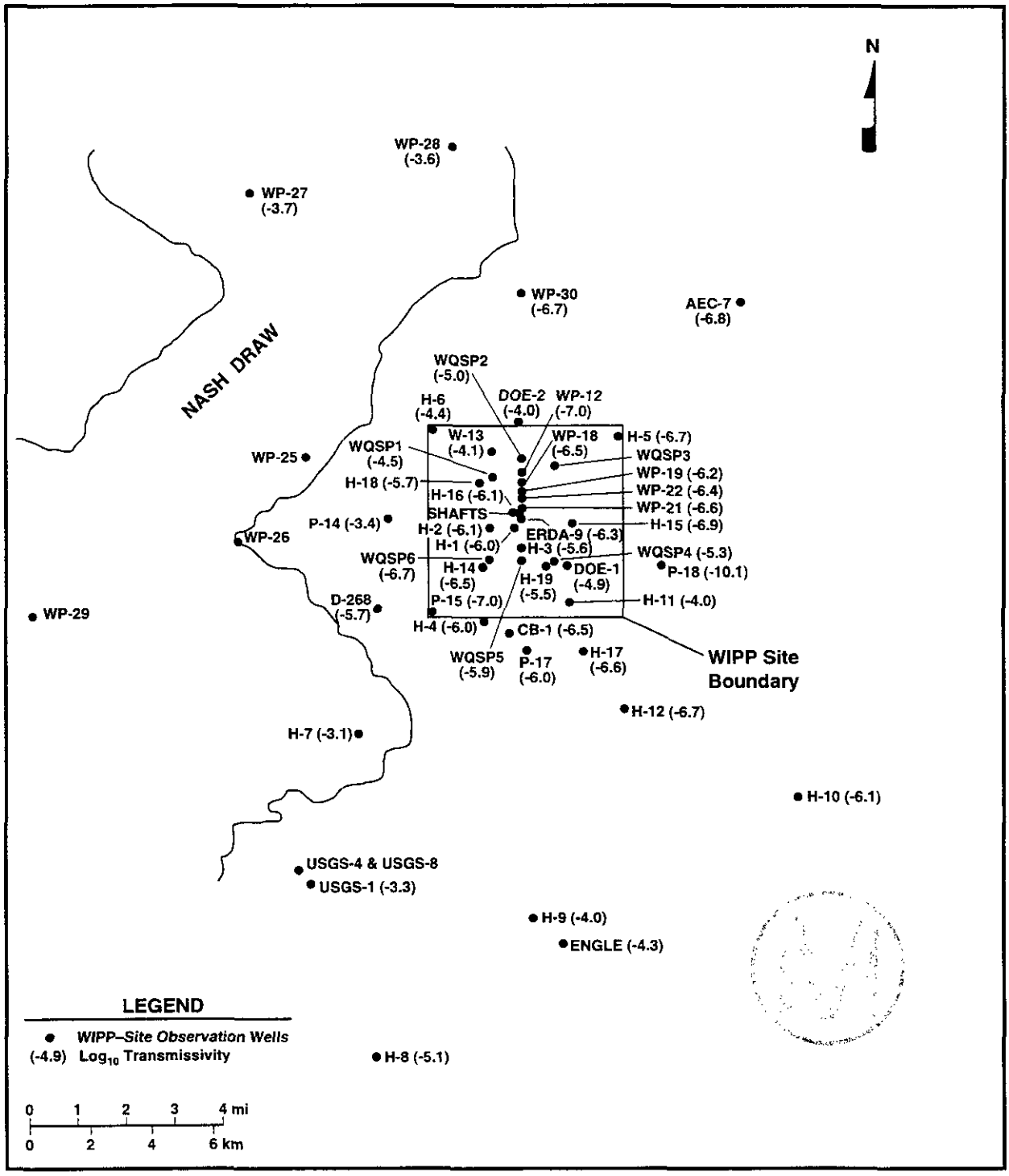

CCA-TFI005-0

Figure TFIELD-5. Culebra $\log_{10}$ Transmissivities at the WIPP Area Boreholes

1 **THIS PAGE INTENTIONALLY LEFT BLANK**

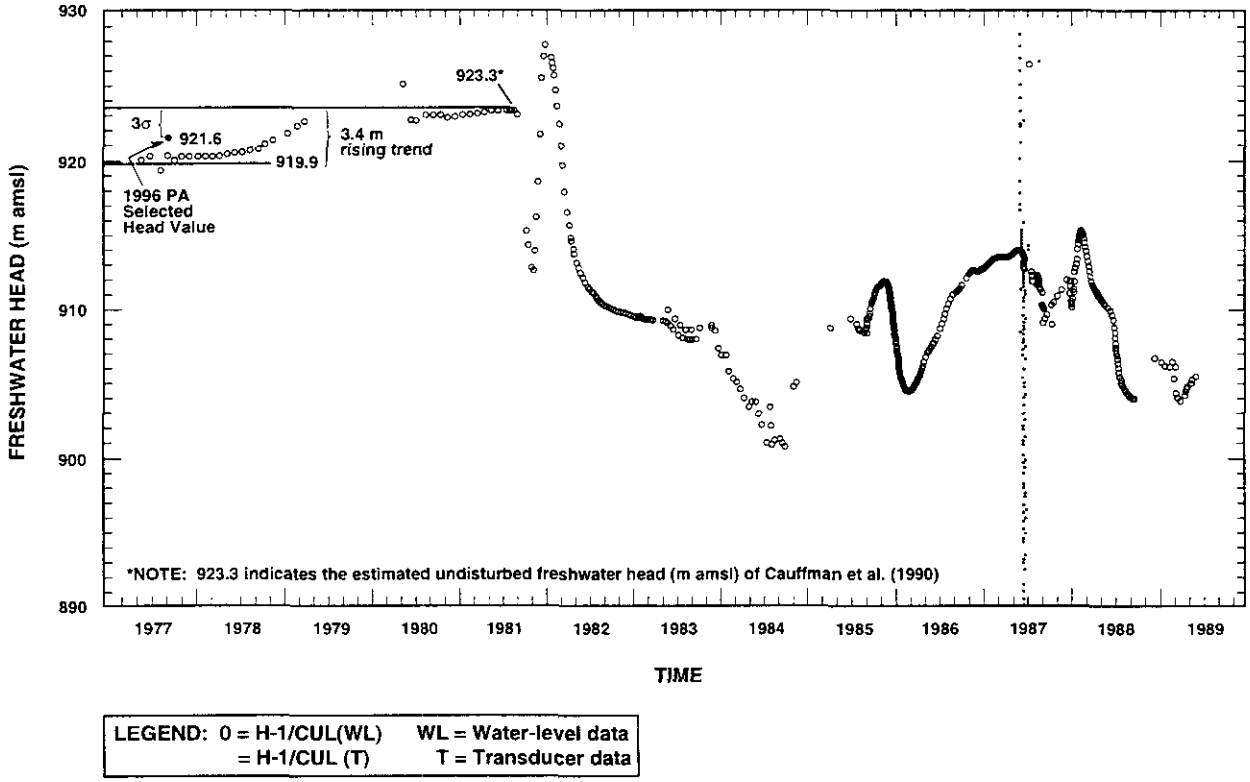

Figure TFIELD-6. Equivalent Freshwater Elevations for the Culebra at Well H-1

1 THIS PAGE INTENTIONALLY LEFT BLANK

Table TFIELD-3 summarizes the reselected head values and the uncertainties. For example, the entry for Well H-1 shows the new value for the undisturbed head (921.6 meters), the range of the trend (3.4 meters), the overall uncertainty due to measurement error (±2.0), the overall head variance (1.5), and the steady-state head weight (0.7). The data in the "Residual Effects" column is taken from Table 5.4 in LaVenue et al. (1989). The undisturbed head column also indicates whether the 1996 head value was decreased from the Cauffman et al. data (D), increased (I), or remained the same (S).

A map of the undisturbed freshwater heads within the Culebra is illustrated in Figure TFIELD-7. Generally, the freshwater heads reveal a predominantly southerly flow direction across the WIPP site. The heads southeast of the WIPP-site area reflect an approximate westerly flow direction.

TFIELD.3 GRASP-INV Code Description

GRASP-INV solves the inverse problem for Darcy's Law of groundwater flow. That is, given information concerning the physical characteristics of an aquifer and its groundwater heads spatially and/or temporally, GRASP-INV determines a spatially varying transmissivity field that will reproduce the observed heads (within the head uncertainty bounds). GRASP_INV was designed to meet the needs of the DOE by solving the inverse problem to determine the Culebra transmissivity field using the measured heads within the Culebra. However, because the performance assessment calculations employ Monte Carlo simulation, numerous calibrated Culebra transmissivity fields are required. Therefore, GRASP-INV calibrates numerous transmissivity fields, each of which has different spatial characteristics.

The general process used in the GRASP-INV code is illustrated by the flow chart in Figure TFIELD-8. The initial transmissivity field is generated through a geostatistical simulation routine called CONSIM II. This simulation is usually performed on a grid much finer than the flow model finite difference grid. Once a field is generated, the flow model grid is superimposed upon the geostatistical simulation grid and average transmissivity values are calculated for each flow model grid block by analyzing the simulation grid point values falling within each grid block. The grid-block transmissivity values are then sent to the flow model, SWIFT II. SWIFT II calculates groundwater pressures and velocities across the flow model domain and sends this information to GRASP II, a sensitivity analysis routine.

GRASP II first determines the objective function, which in the case of the Culebra flow model is the weighted least squares error between computed and measured steady-state and/or transient pressures. GRASP II then calculates adjoint sensitivities of the objective function to the addition of a pilot point. Having determined the most sensitive location for the addition of a pilot point into the model transmissivity field, the transmissivity value assigned to the pilot point is optimized by the PAREST routine to reduce the objective function. Constraints are assigned to the optimization process to ensure realistic transmissivity values at the pilot point locations. Once a pilot point's x,y,z location is selected and the transmissivity assigned, the

Table TFIELD-3. Culebra Undisturbed Head Values and Uncertainties

Well	Undisturbed Head* (meters)	Residual Effects in the Data (meters)	Range of Trends (meters)	Overall Head Uncertainty due to Measurement Error (meters)	Overall Head Variance	Steady-State Head Weight
H-1	921.6 (D)		3.4	±2.0	1.5	0.7
H-2	924.8 (I)		1.6	+1.8/-0.1	0.3	3.3
H-3	914.8 (D)		4.6	±1.9	2.0	0.5
H-4	911.4 (D)		2.8	±0.6	0.4	2.5
H-5	934.2 (I)		0.3	±1.4	0.3	3.3
H-6	932.0 (D)		1.2	±1.0	0.3	3.3
H-7	912.7 (S)		1.1	+0.5/-0.1	0.1	10.0
H-9	906.4 (D)		3.5	+1.2/-0.1	0.6	1.7
H-10	921.3 (S)		1.0	±2.2	0.8	NA
H-11	912.4 (D)	2.0	2.4	+3.0/-1.0	1.1	0.9
H-12	913.5 (S)		1.0	+1.2/-1.2	0.3	3.3
H-14	916.9 (D)	3.2	0.5	+3.9/-0.1	0.6	1.7
H-15	916.1 (D)	2.9	0.4	+4.2/-0.1	0.6	1.7
H-17	911.0		0.0	±0.9	0.3	3.3
H-18	932.4	1.4	0.0	+2.5/-1.1	0.4	2.5
DOE-1	914.3	2.2	0.0	+4.3/-2.2	0.8	1.3
DOE-2	934.7 (S)		2.7	±1.5	0.9	1.1
P-14	926.9 (S)		1.9	±0.9	0.6	1.7
P-15	917.8(I)		2.6	±0.8	0.5	2.0
P-17	909.3 (D)		4.6	±0.7	1.0	1.0
W-12	933.6 (S)	0.9	1.0	+2.2/-0.1	0.3	3.3
W-13	933.7 (D)	0.3	0.8	+1.5/-1.3	0.4	2.5
W-18	930.5 (D)	1.8	0.8	+3.0/-1.2	0.7	1.4
W-25	928.7 (S)		1.4	±1.0	0.3	3.3
W-26	918.5 (D)		2.0	+0.4/-0.1	0.2	5.0
W-27	938.1		0.0	±0.7	0.1	NA
W-28	937.5 (I)		0.8	+0.9/-1.2	0.2	5.0
W-30	934.1 (D)		2.0	+0.9/-1.3	0.5	2.0

Table TFIELD-3. Culebra Undisturbed Head Values and Uncertainties (Continued)

Well	Undisturbed Head* (meters)	Residual Effects in the Data (meters)	Range of Trends (meters)	Overall Head Uncertainty due to Measurement Error (meters)	Overall Head Variance	Steady-State Head Weight
CB-1	911.1 (S)		0.6	±0.7	0.1	10.0
USGS-1	909.8 (S)		1.6	+0.4/-0.1	0.1	10.0
D-268	915.2		0.0	+0.4/-0.1	0.3	3.3
AEC7	932.0		0.0	±0.8	0.3	3.3

* As the result of including the trend in the uncertainty, the 1996 head value, shown in column 2, was either increased (I) from the 1990 value to accommodate a downward trend, decreased (D) to accommodate a rising trend, or remained the same (S) to reflect that the trend did not significantly contribute to the uncertainty. For example, the rising trend of 3.4 m for Well H-1 meant that the 1996 head value was lower than the 1990 value.

transmissivity field is modified by determining the influence of the pilot point upon the surrounding grid block transmisssivity values (Figure TFIELD-9). The modified transmissivity field is then sent back to SWIFT II and the process repeats until the objective function is reduced to a specified minimum or until a selected maximum number of pilot points has been added.

Another approach to solving the inverse problem consists of dividing the model domain into a few zones; in each of these zones, the transmissivity is treated as constant. The transmissivities in the different zones constitute the parameters to be adjusted in the optimization process. The delineation of zones is a subjective process that affects the results of the calibration. Several alternative zonation patterns may have to be considered for calibration; also, uniform transmissivities are assigned to each zone. This approach was found to be inadequate for addressing the issues of spatial variability, as indicated by the study described in Niou and Pietz (1987). These authors attempted to match the hydraulic response to the H-3 Multipad pumping test using a zonation approach. Their study produced a set of transmissivity zones within which the transmissivities were constant.

To avoid the above difficulties of the zonation approach, an approach using pilot points (de Marsily et al. 1984; LaVenue and Pickens 1992) as parameters is adopted. Conceptually, a pilot point may be viewed as a simple mechanism to effect realistic modifications of transmissivity in the region of the model surrounding the pilot-point location. The definition of the transmissivity field using the pilot point method, as presented by de Marsily et al. (1984), Certes and de Marsily (1991), LaVenue and Pickens (1992), and Capilla et al. (1993), was compared with other methods by Keidser and Rosbjerg (1991). Keidser and Rosbjerg concluded their comparison of the pilot point approach with other techniques based on zoning

by stating that "...it [pilot point] is the best at reproducing large local heterogeneities due to the influence of the pilot points on the kriged T fields."

The question arises whether the generated fields are indeed equally plausible (that is, each field has the same probability of representing the real field). It is well known that unconditional simulations, such as those generated by the sequential Gaussian simulation (sGs) method, are in principle independent and equally likely if the random number generator used to produce them is adequate. Conditioning these simulations on measured T data maintains this equal-likeliness. Is it still the same after a second conditioning by the head measurements through an inverse? To ensure this, a constant number of pilot points for each simulation is prescribed first, so that the calibration has the same degree of freedom and plausibility. If the calibration criterion reached through optimization (an L_2 norm based on the difference between observed and calculated heads) was identical for all simulations, one would be justified in claiming that the equal-likeliness of the simulations would be preserved. This will not be exactly the case in practice: each conditionally simulated and calibrated field will reach a slightly different minimal norm. One might then think that those fields with a lesser norm could be slightly more likely than the ones with a larger norm. In practice, this difference is neglected, since the difference in norm will be very small.

The drawback of the proposed methodology is that it is computationally intensive, as each simulated field requires the solution of a new inverse problem. It also assumes that the distribution of the T field is lognormal, which, in the case of the Culebra, is reasonably verified by the data.

GRASP-INV is composed of four main routines as discussed above: CONSIM II, SWIFT II, GRASP II, and PAREST. The following sections will present the theory used in these routines to give the reader the ability to construct the appropriate data sets for GRASP-INV.

TFIELD.3.1 CONSIM II

CONSIM II is a computer program for the geostatistical simulation of heterogeneous geologic media and related spatial random variables. It creates one-, two- or three-dimensional simulated fields of spatially correlated random variables that may be conditioned to measured values. CONSIM II also produces estimated fields based on the measured values via kriging. The program is written in FORTRAN-77, and is developed from GSLIB, the well-known library of geostatistical programs published by Deutsch and Journel (1992). The text in this section has been excerpted from the text contained in Deutsch and Journel (1992). CONSIM II uses a two-step approach to simulating geologic media. The first step is to simulate lithology within a formation as discrete categories using Indicator Categorical Simulation (iCs). The second step 'fills in' the property of interest at each location for each category, for example, permeability for each rock type. The continuous variable is simulated parametrically by Sequential Gaussian Simulation (sGs). If observed values of the variable of interest are

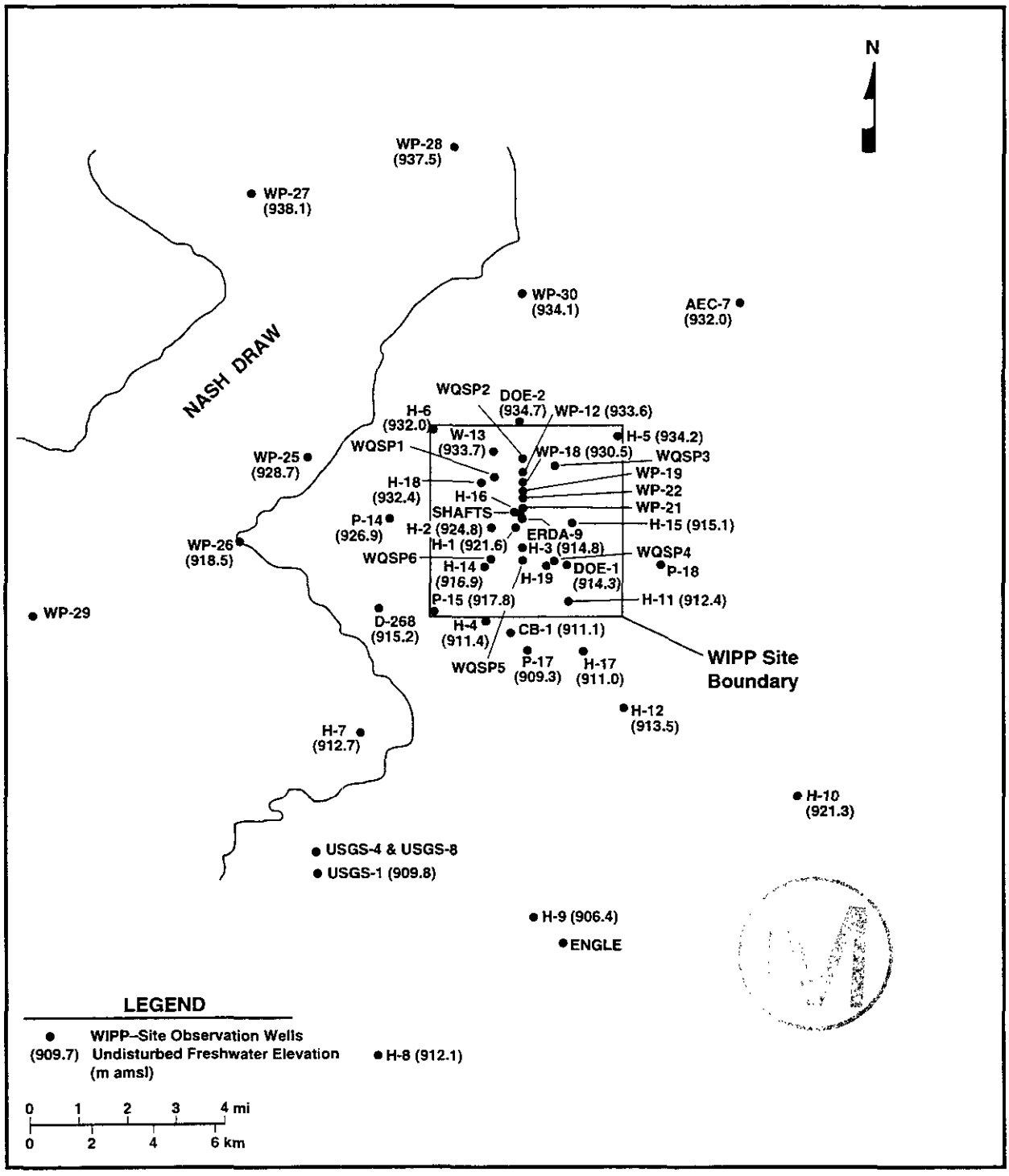

CCA-TFI007-0

Figure TFIELD-7. Culebra Freshwater Heads at the WIPP Area Boreholes

THIS PAGE INTENTIONALLY LEFT BLANK

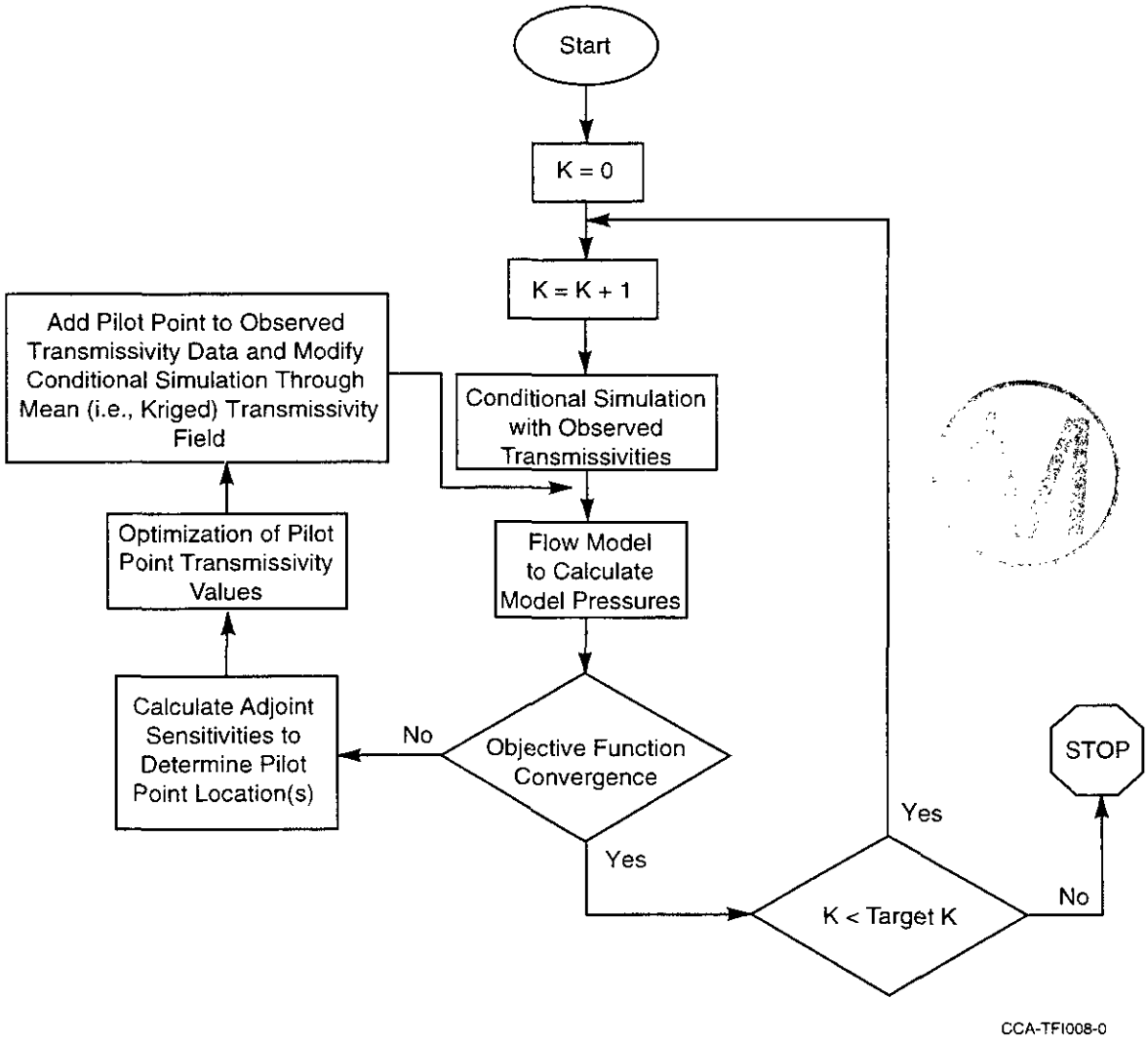

Figure TFIELD-8. Flow Chart of GRASP-INV

THIS PAGE INTENTIONALLY LEFT BLANK

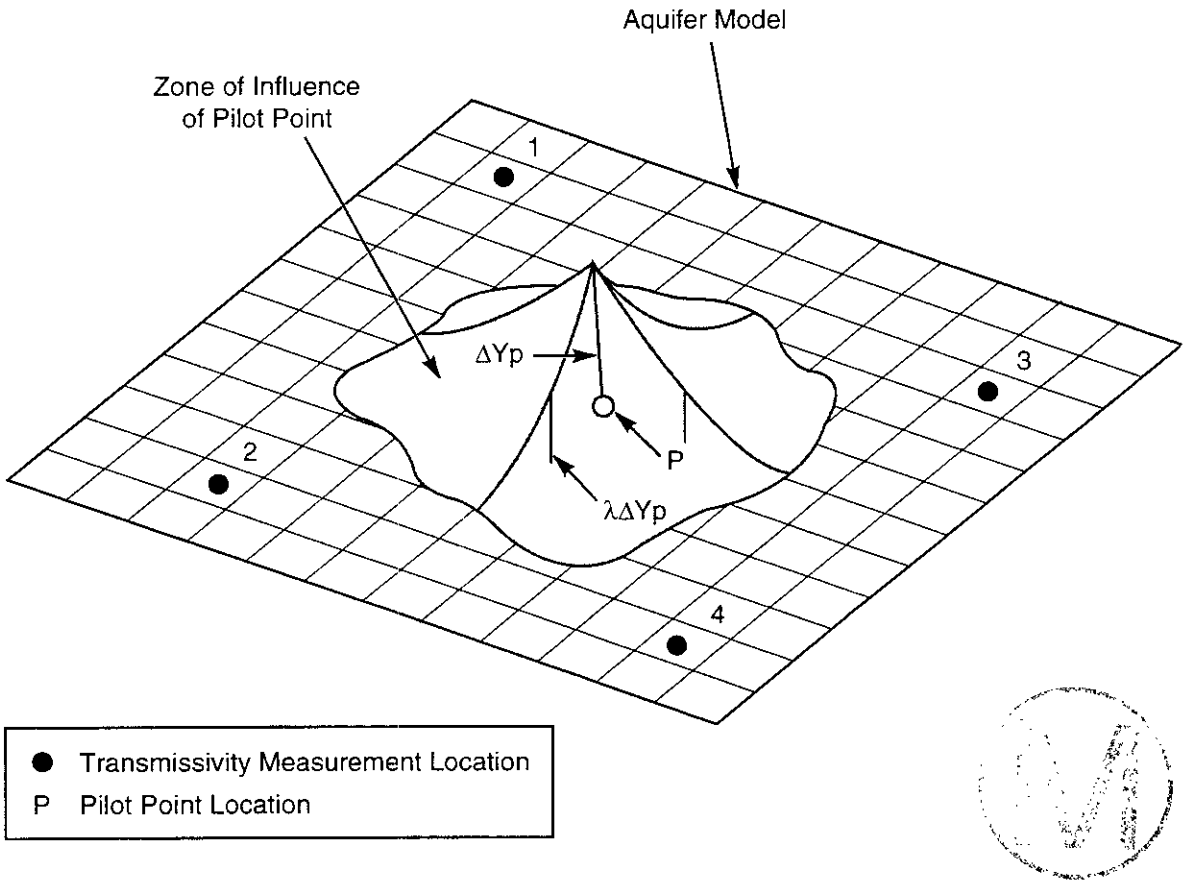

Pilot Point - Schematic

		X	Y	T	y ($\log_{10}$ T)	σ_y
Measured Transmissivity	1 2 ⋮ 4	150	1050	$10^{-3.1}$	-3.1	0.5
Pilot Points added in Calibration	P_1 P_2 ⋮ P_n	650	620	$10^{-4.81}$	-4.81	0.84

CCA-TFI009-0

Figure TFIELD-9. Spatial Influence of a Pilot Point upon Model Grid-Block Transmissivities

THIS PAGE INTENTIONALLY LEFT BLANK

available, the simulations will reproduce the observations at their locations while providing alternative, equally plausible realizations for the unmeasured regions of the field.

CONSIM II may be used to simulate a variety of geologic media; examples include

- the permeabilities of both sand and shale layers within a single formation,
- the transmissivities of both fractured and massive units within a limestone aquifer, and
- facies changes and the associated material properties for an alluvial or aeolian deposit.

TFIELD.3.1.1 CONSIM II: Normal Scores Transform

Gaussian-based simulation programs such as CONSIM II work with normal scores of the original data. The conditioning data used in the simulations are first transformed to their normal scores, calculations are then performed in the normal space, then the results (that is, kriging results or simulation results) are back transformed. This section provides details of the normal scores transformation step. CONSIM II will also accept data that have already been transformed.

Consider the original data T_i, $i = 1,..., n$, each with a specified probability,

$$p_i, i = 1, ..., n, (\text{with } \sum_{i=1}^{n} p_i = 1.0), \quad (1)$$

to account for clustering. If clustering is not considered important then all the p_is can be set equal to $1/n$. Tied T-data values are randomly ordered. When there is a large proportion of T-data in a tie, these tied values should be ranked (despiked) prior to using CONSIM II.

Because of the limited sample size available in most applications, one should consider a non-zero probability for values less than the data minimum or greater than the data maximum. Thus some assumptions must be made about the (unsampled) tails of the attribute distribution.

One common solution is to standardize all previous probabilities p_i to a sum slightly less than one, for example, to $n/n+1$ if there are n data. This solution is sensitive to the number of data (sample size), and it does not offer any flexibility in modeling the distribution tails.

To avoid the problem of sensitivity to sample size, the cumulative probability associated with each data value is reset to the average between its cumulative probability and that of the next lowest datum. This allows finite probabilities to be lower than the data minimum and greater than the data maximum.

For notation, let c_i be the cumulative probability associated with the ith largest data value, T_i,

$$T_i \ (c_i = \sum_{j=1}^{i} p_j). \tag{2}$$

The normal score transform y_i associated with T_i is then calculated as

$$y_i = G^{-1}\left(\frac{c_i + c_{i-1}}{2}\right), \tag{3}$$

with $G(y)$ being the standard normal cumulative distribution function (CDF), $y_c = G^{-1}(c)$ being the corresponding standard normal c-quantile, and $c_0 = 0.0$. GSLIB utilizes the numerical approximation to $G^{-1}(\ )$ proposed by Kennedy and Gentle (1980).

The normal scores transformation is automatically performed in the sGs algorithm and the transformed data are saved to a file for later use in the back transformation of the results into the real space. The back transformation T_i of the standard normal deviate y_i is given by

$$T_i = F^{-1}[G(y_i)], \tag{4}$$

where $F(T)$ is the (declustered) CDF of the original data.

Almost always, the value $G(y_i)$ will not correspond exactly to an original sample, CDF value F; therefore, some interpolation between the original sample T-values or extrapolation beyond the smallest and largest T-value will be required. Linear interpolation is always performed between two known values. A variety of options is available on how the tails of the distribution will be treated; these options are discussed in the next section.

The normal score back transform aims at exactly reproducing the sample CDF $F(T)$, except for the within class interpolation and the two extreme class extrapolations. Hence details of the sample CDF that are deemed not representative of the population should be smoothed out prior to using CONSIM II.

TFIELD.3.1.2 CONSIM II: CDF Interpolation Models

Both the normal scores transform algorithm and the indicator complementary cumulative distribution function (CCDF) transform result in discrete CDFs (for example, Figure TFIELD-10). Because estimated or simulated values may not correspond to the cutoff values, these methods will require interpolating between cutoffs and at the tail values.

The within-class CDF interpolation models considered in CONSIM II are:

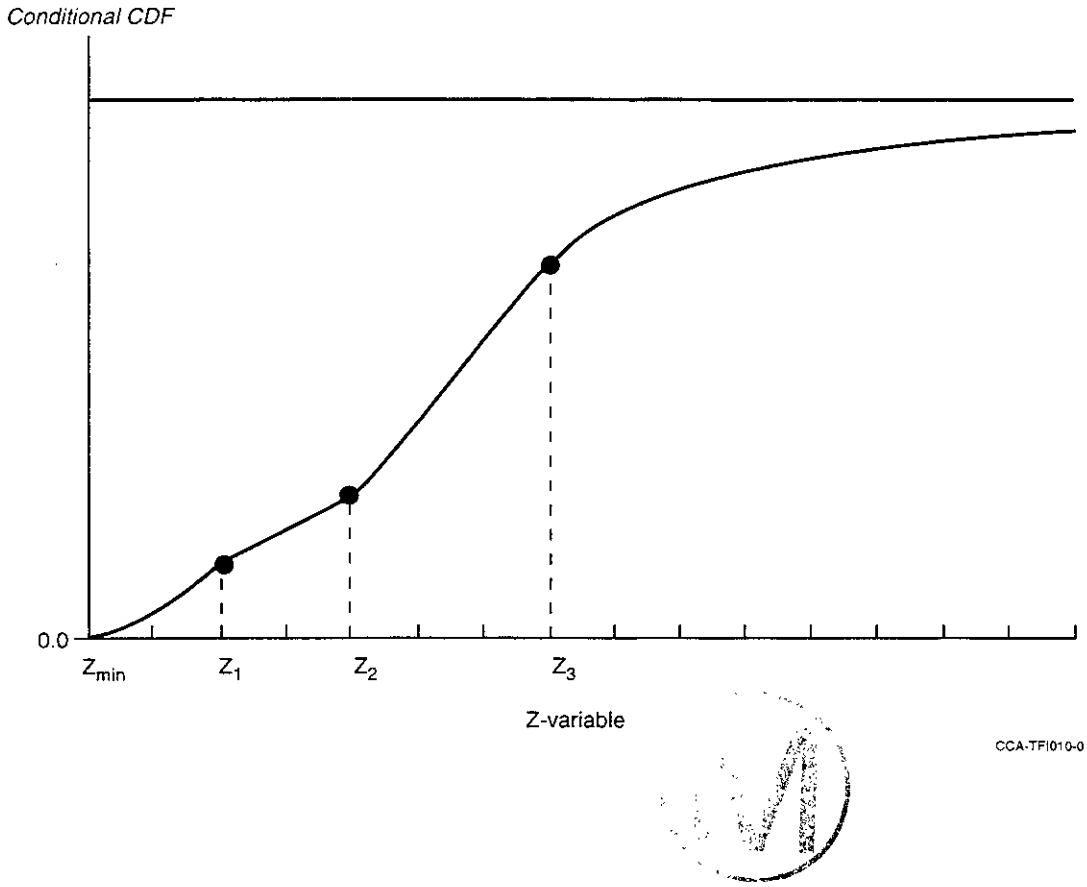

Figure TFIELD-10. Discrete Cumulative Distribution Function (CDF)

1 THIS PAGE INTENTIONALLY LEFT BLANK

Power Model: For a finite class interval $(T_{k-1}, T_k]$ and a parameter (the power) > 0, this CDF model is written:

$$F^{w}_{T_{k-1},T_k}(T) = \begin{cases} 0, & \forall T \le T_{k-1} \\ \left[\frac{T-T_{k-1}}{T_k-T_{k-1}}\right]^{w}, & \forall T \in (T_{k-1}, T_k) \\ 1, & \forall T \ge T_k \end{cases} \quad (5)$$

In practice, this CDF model is scaled between the calculated CDF values at T_{k-1} and T_k rather than between 0 and 1. Distributions with $w < 1$ are positively skewed, $w = 1$ corresponds to the linear CDF model (uniform distribution), and distributions with $w > 1$ are negatively skewed; see Figure TFIELD-11.

Linear Interpolation between Tabulated Bound Values: This option considers a fixed number of subclasses with given bound values within each class (T_{k-1}, T_k). For example, the three bound values a_{k1}, a_{k2}, a_{k3} can be tabulated defining four sub-classes (T_{k-1}, a_{k1}), (a_{k1}, a_{k2}), (a_{k2}, a_{k3}), (a_{k3}, T_k) that share the probability p_k calculated for class (T_{k-1}, T_k); p_k is shared equally unless specified otherwise. Then, linear CDF interpolation is performed separately within each sub-class.

This option allows the user to add detail to the distribution within the classes defined by the cutoff T_k. That detail, that is, the sub-class bound values, can be attributed to some or all of the original data values falling within each class (T_{k-1}, T_{k-1}) of the marginal (sample) distribution. Thus, some of the resolution lost through descretization by the T_k values can be recovered. More generally, the sub-class bound values a_k can be taken from any parametric model, for example, beta or gamma distribution.

Hyperbolic Model: This last option is to be used only for the upper tail of a positively skewed distribution. Decisions regarding the upper tail of CCDFs are often the most consequential; therefore, a great deal of flexibility is needed, including the possibility of a very long tail.

The hyperbolic CDF upper tail model (Figure TFIELD-12) for a strictly positive variable is a two parameter distribution:

$$F_{w,\lambda}(T) = 1 - \frac{\lambda}{T^{w}}, w \ge 1, T^{w} > \lambda > 0. \quad (6)$$

The scaling parameter λ allows identification of any precalculated quantile value, for example, the *p*-quantile T_p such that $F_{\omega,\lambda}(T_p) = p$, then:

$$\lambda = T_p^w (1-p). \quad (7)$$

The parameter w > 1 controls how fast the CDF reaches its upper limit value 1; the smaller w, the longer the tail of the distribution.

The mean *T*-value above the *p*-quantile value T_p is:

$$m_p = \frac{w}{w-1} T_p > T_p. \quad (8)$$

Hence the smaller w, the larger the mean above T_p. At its minimum value, w = 1 identifies the Pareto distribution which has an infinite mean m_p, $\forall p$, corresponding to a very long tail. w = 1.5 is suggested.

CONSIM II allows different sets of options depending on whether interpolation is needed within the middle classes or extrapolation for the lower and upper tails. The available options are:

Lower Tail: Below the first calculated CDF value:

1. Linear model or uniform distribution
2. Power model
3. Tabulated bound values

Middle: Between any two calculated CDF values:

1. Linear model (uniform distribution)
2. Power model
3. Tabulated bound values

Upper Tail: Above the last calculated CDF value:

1. Linear model (uniform distribution)
2. Power model
3. Tabulated bound values
4. Hyperbolic model

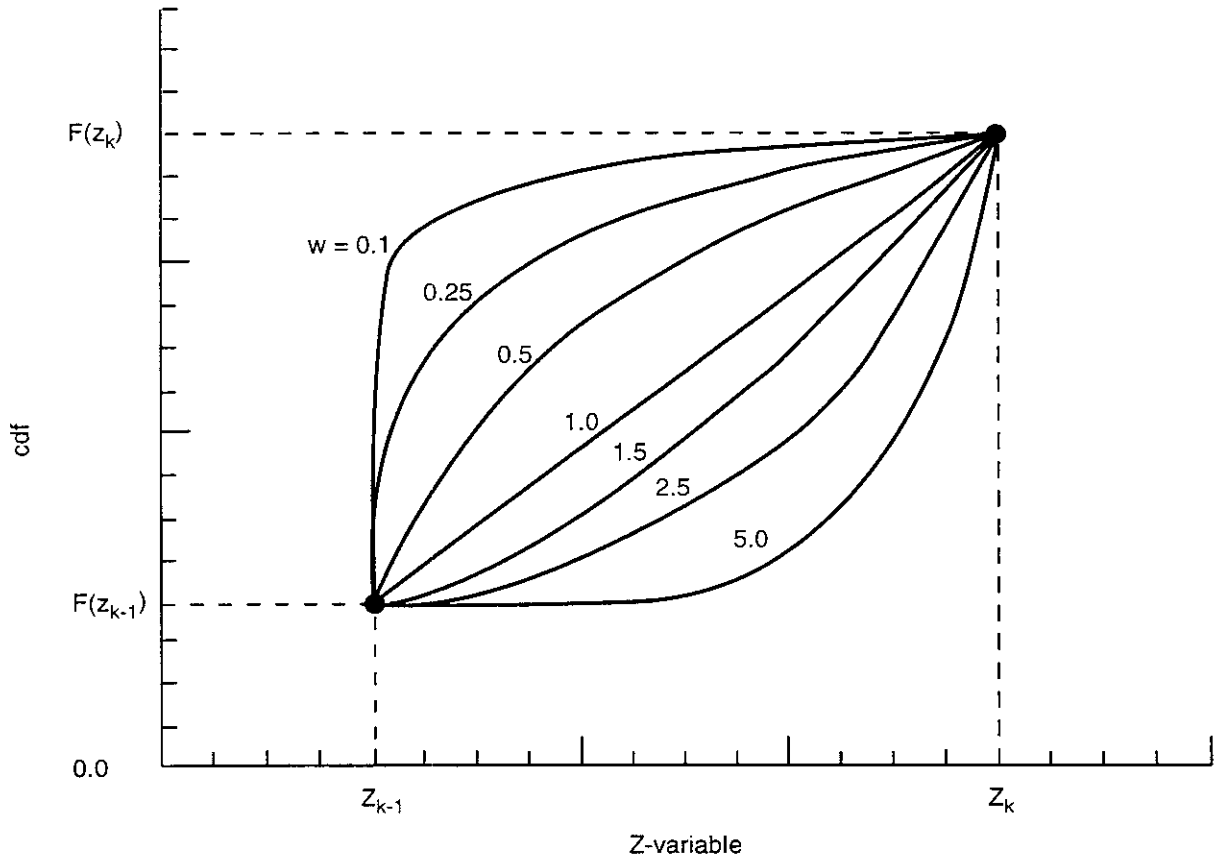

Figure TFIELD-11. Power Model Fit between CDF Points

1 THIS PAGE INTENTIONALLY LEFT BLANK

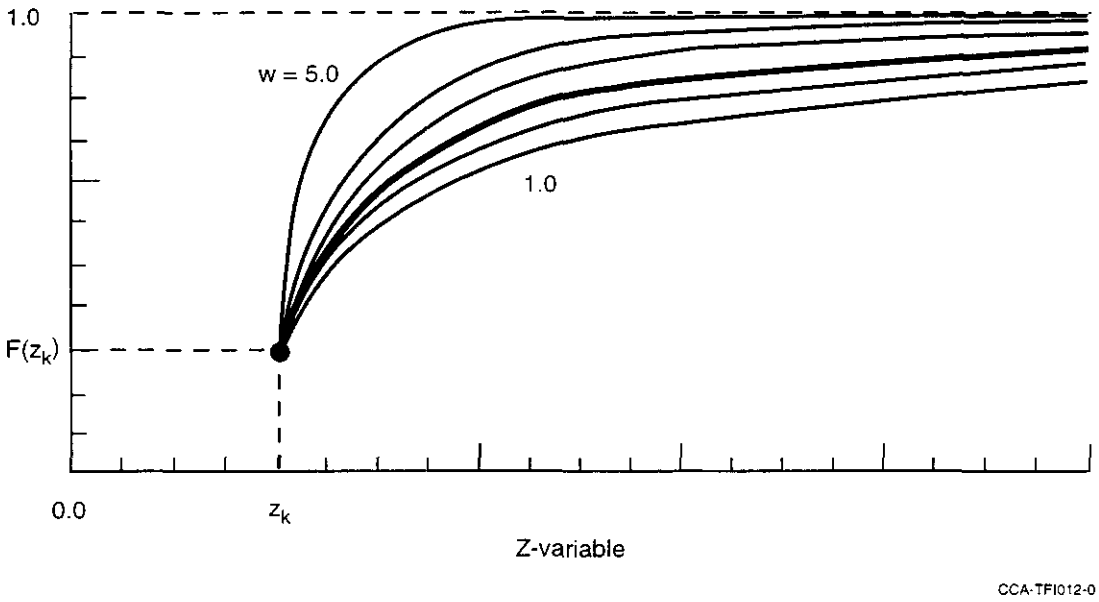

Figure TFIELD-12. Hyperbolic Model for Fitting Tails

THIS PAGE INTENTIONALLY LEFT BLANK

The user is asked for a specific model for each of these regions (the integer number identifying each model in the list above is used).

TFIELD.3.1.3 CONSIM II: Variogram Model Specification

This section describes the conventions for describing a variogram model and can be scanned quickly the first time through. Most of the kriging and simulation subroutines call for covariance or pseudo-covariance values; however, a semivariogram model rather than a covariance model must be specified for the normal scores data. This apparent inconsistency allows for the traditional practice of modeling variograms and also permits the straightforward incorporation of the power model, which has no covariance counterpart.

TFIELD.3.1.3.1 Model Types

An acceptable semivariogram model for CONSIM II consists of an isotropic nugget effect and any positive linear combination of up to four of the standard semivariogram models. The standard models are:

1. **Spherical** model defined by an actual range a and positive variance contribution or *sill* value c.

$$\gamma(h) = c \bullet Sph\left(\frac{h}{a}\right) = \begin{cases} c \bullet \left[1.5\frac{h}{a} - 0.5\left(\frac{h}{a}\right)^3\right], & \text{if } h \le a \\ c, & \text{if } h \ge a \end{cases} \tag{9}$$

2. **Exponential** model defined by a parameter a (effective range $3a$) and positive variance contribution value c.

$$\gamma(h) = c \bullet Exp\left(\frac{h}{a}\right) = c \bullet \left[1 - \exp\left(-\frac{h}{a}\right)\right]. \tag{10}$$

3. **Gaussian** model defined by a parameter a (effective range a 3) and positive variance contribution value c.

$$\gamma(h) = c \bullet \left[1 - \exp\left(-\frac{h^2}{a^2}\right)\right] \tag{11}$$

4. **Power** model defined by a power $0 < a < 2$ and positive slope c.

$$\gamma(h) = c \bullet h^a \tag{12}$$

The type of variogram structure is specified by an integer code, which is the order in the above list, that is, *it* = 1: spherical model, *it* = 2: exponential model, *it* = 3: Gaussian model, and *it* = 4: power model. The *a* and *c* parameter values, which correspond to the description in the above list, are also needed.

For the first three semivariograms parameter *a* has units length (L) and parameter *c* is dimensionless. For the power model, *a* is dimensionless and *c* has inverse length units (L^{-a}). Length units must be consistent with the length unit used for the geostatistical simulation grid (and thus the same as for the coordinates of the conditioning data).

TFIELD.3.1.3.2 Variogram Anisotropy

Each nested structure requires an additional two or five parameters that define its own geometric anisotropy in 2-D or 3-D. Figure TFIELD-13 illustrates the angle and anisotropy factor required in 2-D:

- The rotation angle *ang* corresponds to an azimuth angle measured in degrees clockwise from the positive Y or north direction. The range parameter *a* is applied directly to this principal direction. The distances along the minor direction, that is, at 90 degrees from the principal direction, are obtained by multiplying *a* by the second parameter *anis*.

- The anisotropy factor *anis* is the range in the minor direction divided by the range in the principal direction. Hence, it is normally less than one. There is no requirement, however, that the *anis* parameter be less than one; for example, it may be set very large to model a zonal anisotropy (discussed below). Note that a very large anisotropy factor will add the variogram structure in the principal direction and add nothing in any other direction, a feature known as "zonal anisotropy."

With CONSIM II the actual distance is corrected so that it accounts for the specified anisotropy. That is, the distance component in the rotated X axis (see Figure TFIELD-13) is divided by *anis*. In other words, the anisotropy parameters do not apply to the *a* parameter of the variogram. Consequently, the anisotropy of the power model is handled in an intuitively correct manner; an anisotropic distance is calculated and the power *a* is left unchanged.

Figure TFIELD-14 illustrates the angles and anisotropy factors required in 3-D. It is quite straightforward to visualize a phenomenon that is dipping with respect to the horizontal at a dip azimuth that is not aligned with a coordinate axis. The third angle is required to account for the geological concept of a plunge or rake. One example that requires a third angle is modeling the geometric anisotropy within the limbs of a plunging syncline.

The easiest way to describe the three angles and two anisotropy factors is to imagine the rotations and squeezing that would be required to transform a sphere into an ellipsoid. The outer shell of the ellipsoid consists of points at the same structural distance, for example, if the ellipsoid is one half as large in one direction then the attribute is one half as continuous. We

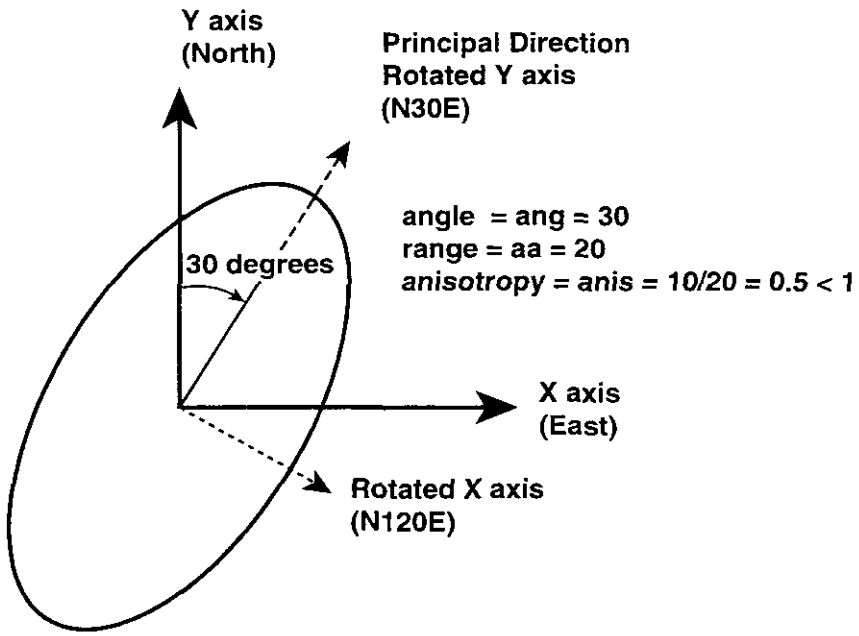

CCA-TFI013-0

Figure TFIELD-13. Angle and Axis Rotation used in 2-D Variogram Analysis

THIS PAGE INTENTIONALLY LEFT BLANK

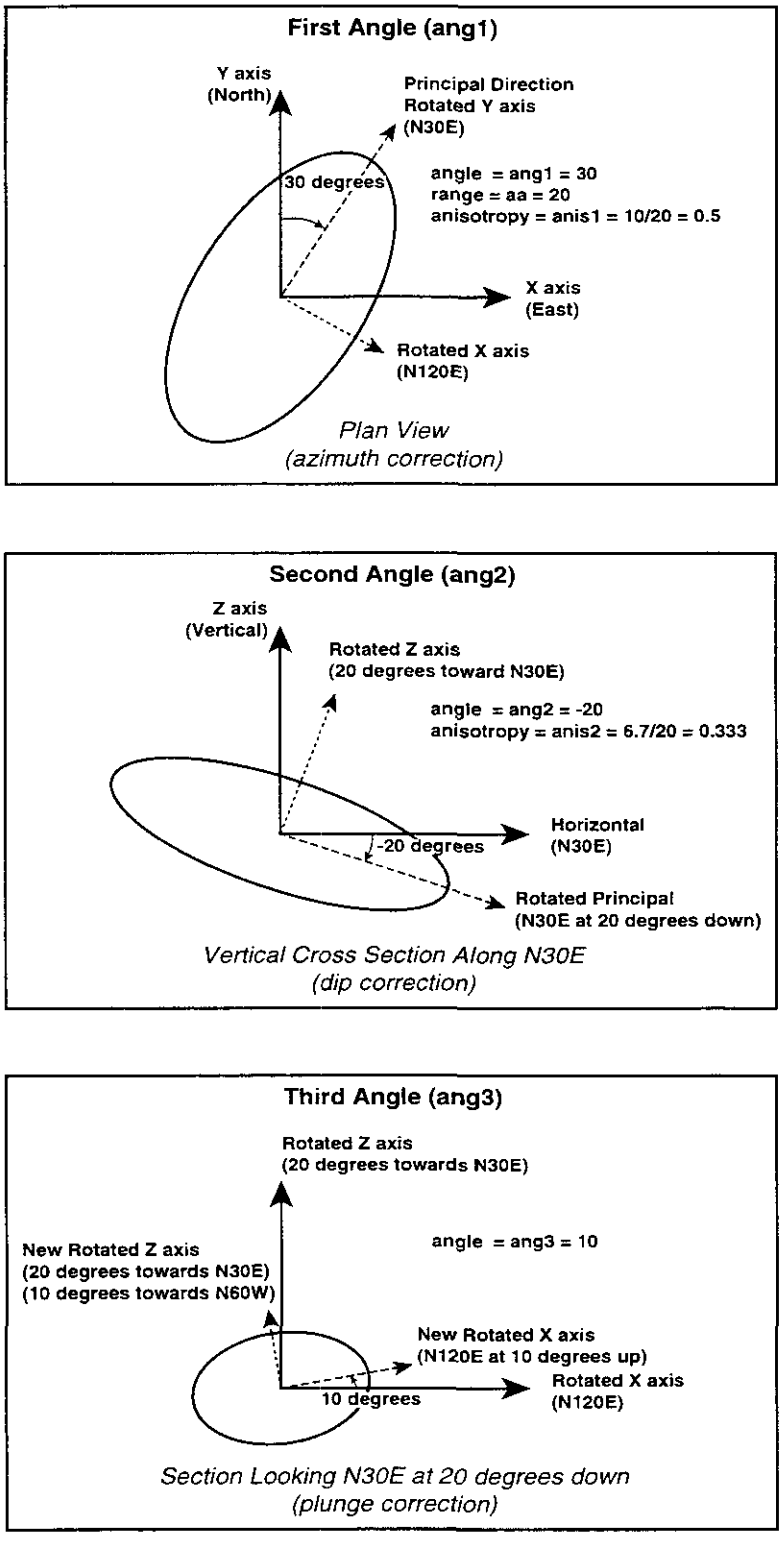

CCA-TFI014-0

Figure TFIELD-14. Angle and Axis Rotation used in 3-D Variogram Analysis

THIS PAGE INTENTIONALLY LEFT BLANK

will refer to the original *y* axis as the principal direction and consider the rotations such that it ends up being the actual principal structural direction (direction of maximum continuity):

- the first rotation angle, *ang*1, rotates the original *Y* axis (principal direction) in the horizontal plane: this angle is measured in degrees clockwise.

- The second rotation angle, *ang*2, rotates the principal direction from the horizontal: this angle is measured in negative degrees down from horizontal.

- The third rotation angle, *ang*3, leaves the principal direction, defined by *ang*1 and *ang*2, unchanged. The two directions orthogonal to the principal direction are rotated clockwise relative to the principal direction when looking toward the origin. The rotation of the Third Step in Figure TFIELD-14 appears as counterclockwise because the view is away from the origin.

Zonal anisotropy can be considered as a particular case of a geometric anisotropy (see Isaaks and Srivastava 1989, 385–386). This situation can be handled by entering the anisotropy parameter *anis* as a very large number, which causes the implicit range in the minor direction to infinity; the particular variogram structure is then added only to the major direction.

Note that, whether in 2-D or 3-D, the anisotropy directions need not be the same for each nested structure, allowing for a great flexibility in modeling experimental anisotropy. However, the more complicated the variogram model, the longer it takes to construct each kriging matrix; hence, the longer the kriging or simulation program will take. For an excellent discussion on variogram modeling, refer to Chapter 16 of Isaaks and Srivastava (1989).

TFIELD.3.1.3.3 A Straightforward 2-D Variogram Example

Consider the semivariogram shown on Figure TFIELD-15. The dots are the experimental semivariogram points in two orthogonal directions. The semivariogram that reaches the sill first (at about 10 to 15 distance units) is in the north-south direction (an azimuth of 0.0) and the variogram with the longer range is in the east-west direction (an azimuth of 90 degrees). The solid line in both directions is the fitted semivariogram model.

The north-south model was fitted with a nugget effect of 0.22, an exponential structure with contribution 0.53 and range parameter *a* of 1.6, and a spherical structure with contribution 0.25 and range 15.0. The east-west model was fitted with nugget effect of 0.22, an exponential structure with contribution 0.53 and range parameter *a* of 16.0, and a spherical structure with contribution 0.25 and range 50.0. The semivariogram parameters required by the kriging or simulation programs would be specified as follows:

c0 = nugget = 0.22.

nst = number of nested structures = 2.

it(1) = type of structure 1 = 2 (exponential).

azimuth(1) = 90 degrees (the east-west direction).

cc(1) = contribution of structure 1 = 0.53.

aa(1) = range of structure 1 in the direction **azimuth** = 16.0.

anis(1) = anisotropy of structure 1 = 1.6/16.0 = 0.10.

it(2) = type of structure 2 = 1 (spherical).

azimuth(2) = 90 degrees (the east=west direction).

cc(2) = contribution of structure 2 = 0.25.

aa(2) = range of structure 2 in the direction **azimuth** = 50.0.

anis(2) = anisotropy of structure 2 = 15.0/50.0 = 0.30.

TFIELD.3.1.4 CONSIM II: MultiGaussian Kriging

Although kriging was initially introduced to provide estimates for unsampled values, it is being used increasingly to build probabilistic models of uncertainty about these unknown values. In effect, the kriging algorithm provides a minimum error-variance estimate of any unsampled value. Contouring a grid of kriging estimates is the traditional mapping application of kriging. Kriging used as a mapping algorithm is a low-pass filter that tends to smooth out details and extreme values of the original data set.

Because kriging is a minimum error variance estimation algorithm, it approximates, and in some cases is identical to, the conditional expectation of the variable being estimated. Thus, kriging can be used to estimate a series of posterior conditional probability distributions from which unsmoothed images of the attribute spatial distribution can be drawn. In the multiGaussian (MG) case, the conditional distribution is identified by the mean and variance obtained from simple kriging. In the indicator kriging (IK) approach, a series of CCDF values are estimated directly.

The kriging principle, applied both as a mapping algorithm and as a tool to obtain conditional probability distributions, has been presented in numerous papers and textbooks (Isaaks and Srivastava 1989, Chapter 16; Journel and Huijbregts 1978).

TFIELD.3.1.4.1 Simple Kriging

All versions of kriging are elaborations on the basic linear regression algorithm and corresponding estimator:

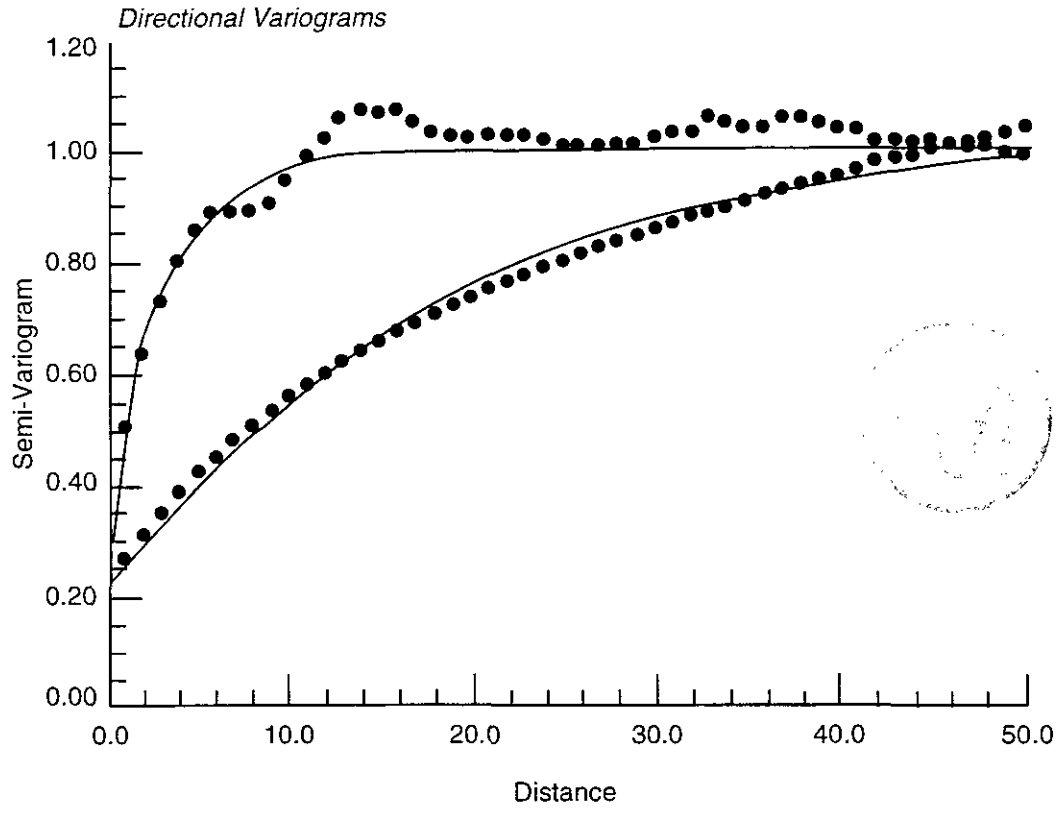

Figure TFIELD-15. 2-D Variogram Example

1 **THIS PAGE INTENTIONALLY LEFT BLANK**

$$[Z^*_{SK}(u) - m(u)] = \sum_{\alpha=1}^{n} \lambda_\alpha(u)[Z(u_\alpha) - m(u_\alpha)], \quad (13)$$

where $Z(\mathbf{u})$ is the random variable (RV) model at location $\mathbf{u}$, the $\mathbf{u}_\alpha$'s are the n data locations, $m(\mathbf{u}) = E\{Z(\mathbf{u})\}$ is the location-dependent expected value of RV, $Z(\mathbf{u})$, and $Z^*_{SK}(\mathbf{u})$ is the linear regression estimator, also called the "simple kriging" (SK) estimator.

The SK weights $\lambda_\alpha(\mathbf{u})$ are given by the system of normal equations written in their more general nonstationary form as follows:

$$\sum_{\beta=1}^{n} \lambda_\beta(u) C(u_\beta, u_\alpha) = C(u, u_\alpha), \alpha = 1, \ldots, n. \quad (14)$$

The SK algorithm requires prior knowledge of the $(n + 1)$ means $m(\mathbf{u})$, $m(\mathbf{u}_\alpha)$, $\alpha = 1, \ldots, n$, and the $(n + 1)$ by $(n + 1)$ covariance matrix $[C(\mathbf{u}_\alpha, \mathbf{u}_\alpha), \alpha, \beta = 0, 1, \ldots, n]$ with $\mathbf{u}_0 = \mathbf{u}$. In most practical situations, inference of these means and covariance values requires a prior hypothesis (rather a *decision*) of stationarity of the random function $Z(\mathbf{u})$. If the random function (RF) $Z(\mathbf{u})$ is stationary with constant mean m, and covariance function $C(\mathbf{h}) = C(\mathbf{u}, \mathbf{u} + \mathbf{h})$, $\forall \mathbf{u}$, the SK estimator reduces to its stationary version:

$$Z^*_{SK}(u) = \sum_{\alpha=1}^{n} \lambda_\alpha(u) Z(u_\alpha) + \left[1 - \sum_{\alpha=1}^{n} \lambda_\alpha(u)\right] m, \quad (15)$$

with the traditional stationary SK system:

$$\sum_{\beta=1}^{n} \lambda_\beta(u) C(u_\beta - u_\alpha) = C(u - u_\alpha), \alpha = 1, \ldots, n. \quad (16)$$

Stationary SK does not adapt to local trends in the data because it relies on the mean value m, assumed known and constant throughout the area. Consequently, SK is rarely used directly for mapping the z-values. Instead, it is the more robust ordinary kriging (OK) algorithm, discussed next, which is used.

According to strict stationary theory, it is SK that should be applied to algorithms such as sequential Gaussian simulation (sGs), which use the normal score transform. The OK algorithm, however, might be considered if enough data are available to reestimate locally the normal score mean.

TFIELD.3.1.4.2 Ordinary Kriging

Ordinary kriging filters the mean from the SK estimator by requiring that the kriging weights sum to one. This results in the following OK estimator:

$$Z^*_{OK}(u) = \sum_{\alpha=1}^{n} \nu_\alpha(u) Z(u_\alpha), \tag{17}$$

and the stationary OK system:

$$\begin{cases} \sum_{\beta=1}^{n} \nu_\beta(u) C(u_\beta - u_\alpha) + \mu(u) = C(u - u_\alpha), \alpha = 1, \ldots, n \\ \sum_{\beta=1}^{n} \nu_\beta(u) = 1 \end{cases} \tag{18}$$

where $\nu_\alpha(\mathbf{u})$'s are the OK weights, and $\mu(\mathbf{u})$ is the Lagrange parameter associated with the constraint in the second expression in (18).

Comparing expression (16) and (18), note that the SK weights are different from the OK weights. It can be shown that ordinary kriging amounts to reestimating, at *each* new location $\mathbf{u}$, the mean m as used in the SK expression. Because OK is most often applied within moving search neighborhoods, that is, using different data sets for different locations $\mathbf{u}$, the implicit reestimated mean denoted $m^*(\mathbf{u})$ depends on the location $\mathbf{u}$. Thus, the OK estimator (17) is, in fact, a simple kriging of type (13) where the constant mean value m is replaced by the location-dependent estimate $m^*(\mathbf{u})$:

$$\begin{aligned} Z^*_{OK}(u) &= \sum_{\alpha=1}^{n} \nu_\alpha(u) Z(u_\alpha) \\ &= \sum_{\alpha=1}^{n} \lambda_\alpha(u) Z(u_\alpha) + \left[1 - \sum_{\alpha=1}^{n} \lambda_\alpha(u)\right] m^*(u) \end{aligned} \tag{19}$$

Hence, OK as applied within moving data neighborhoods is already a nonstationary algorithm, in the sense that it corresponds to a nonstationary random function (RF) model with varying mean but stationary covariance. This ability to rescale locally the RF model $Z(\mathbf{u})$ to a different mean value $m^*(\mathbf{u})$ explains the extreme robustness of the OK algorithm. OK has been and will remain the anchor algorithm of geostatistics.

TFIELD.3.1.5 CONSIM II: Indicator Kriging

Indicator kriging (IK) of a continuous variable provides a least-squares estimate of the CCDF at cutoff z_k:

$$[i(u;z_k)]^* = E\{I(u;z_k|(n)\}^* = \text{Prob}^*\{Z(u)\le z_k|(n)\} \quad (20)$$

where (n) represents the conditioning information available in the neighborhood of location **u**.

The IK process is repeated for a series of K cutoff values z_k, $k = 1,..., K$, which discretize the interval of variability of the *continuous* attribute z. The CCDF, built from assembling the K indicator kriging estimates of type (20), represents a probabilistic model for the uncertainty about the unsampled value $z(\mathbf{u})$.

If $z(\mathbf{u})$ is itself a binary categorical variable, for example, set to 1 if a specific rock type prevails at **u**, to 0 if not, then there is no need for any prior indicator transform. The direct kriging of $z(\mathbf{u})$ provides an estimate for the probability that $z(\mathbf{u})$ be one, that is, for that rock type to prevail at location **u**.

If $z(\mathbf{u})$ is a continuous variable, then the correct selection of the cutoff values z_k at which indicator kriging takes place is essential: with too many cutoff values, the inference and computation become needlessly tedious and expensive; too few, and the details of the distribution are lost.

TFIELD.3.1.5.1 Simple IK

The stationary mean of the binary indicator RF $I(\mathbf{u}; z)$ is the CDF of the RF $Z(\mathbf{u})$ itself; indeed:

$$E\{I(u;z)\} = 1\cdot\text{Prob}\{Z(u)\le z\} + 0\cdot\text{Prob}\{Z(u)>z\} = \text{Prob}\{Z(u)\le z\} = F(z) \quad (21)$$

The SK estimate of the indicator transform $i(\mathbf{u}; z)$ is thus written, according to expression (15):

$$[i(u;z)]^*_{SK} = [\text{Prob}\{Z(u)\le z|(n)\}]^*_{SK} = \sum_{\alpha=1}^{n}\lambda_\alpha(u;z)i(u_\alpha;z) + \left[1-\sum_{\alpha=1}^{n}\lambda_\alpha(u;z)\right]F(z), \quad (22)$$

where the $\lambda_\alpha(\mathbf{u}; z)$'s are the SK weights corresponding to cutoff z. These weights are given by a SK system of type (16):

$$\sum_{\beta=1}^{n} \lambda_\beta(u; z) C_I(u_\beta - u_\alpha; z) = C_I(u - u_\alpha; z), \alpha = 1, \ldots, n, \quad (23)$$

where $C_I(\mathbf{h}; z) = Cov\{I(\mathbf{u}; z), I(\mathbf{u} + \mathbf{h}; z)\}$ is the indicator covariance at cutoff z. If K cutoff values z_k are retained, simple IK requires K indicator covariances $C_I(\mathbf{h}; z_k)$ in addition to the K CDF values $F(z_k)$. If the z-data are preferentially clustered, the sample CDF values should be declustered before being used (see program `declus` in Deutsch and Journel, 1992).

TFIELD.3.1.5.2 Ordinary IK

Just like any simple kriging, simple IK is dependent on the stationarity decision and on the CDF values $F(z)$ interpreted as mean indicator values. When data are abundant, ordinary indicator kriging within moving data neighborhoods may be considered; this amounts to reestimating locally the prior CDF values $F(z)$. Both simple and ordinary kriging are implemented in CONSIM II.

TFIELD.3.1.5.3 Exactitude of the E-type Estimate

Because the CCDF returned by IK honors both hard z-data and constraint intervals, the corresponding E-type estimate (see below) also honors that information. More precisely, at a datum location $\mathbf{u}_\alpha$, $[z(\mathbf{u}_\alpha)]^*_E = z(\mathbf{u}_\alpha)$, if the z-datum is hard, and $[z(\mathbf{u}_\alpha)]^*_E \in (a_\alpha, b_\alpha)$, if the information at u is the constraint interval $z(\mathbf{u}_\alpha) \in (a_\alpha, b_\alpha)$. In practice, the exactitude of the E-type estimate is limited by the finite discretization into K cutoff values z_k. For example, in the case of a hard z-datum, the estimate is: $[z(\mathbf{u}_\alpha)]^*_E \in (z_{k-1}, z_k)$, with z_k being the upper bound of the interval containing the datum value $z(\mathbf{u}_\alpha)$. Thus, the E-type estimate attached to IK provides a straightforward solution to the difficult problem of constrained interpolation, as opposed to the quadratic programming solution which would limit the estimate $z^*(\mathbf{u}_\alpha)$ to either bound a_α or b_α if the constraint interval is active.

TFIELD.3.1.5.4 Correcting for Order Relation Problems

Regardless of the estimation algorithm used, it is imperative to correct order relation deviations. CONSIM II performs these corrections and provides a detailed report of the number and magnitude of corrections at each cutoff. The program performs within-class interpolation, as described in Section TFIELD.3.1.2, to provide any required quantile value or probabilities of exceeding any given threshold value. CONSIM II also returns the mean of the CCDF, called the "E-type" estimate of $z(\mathbf{u})$, and defined as:

$$[z(u)]^*_E = \int_{-\infty}^{+\infty} z \, dF(u; z|(n)) = \sum_{k=1}^{K+1} z'_k \, [F(u; z_k|(n)) - F(u; z_{k-1}|(n))], \quad (24)$$

where z_k, $k = 1,..., K$ are the K cutoffs retained, and $z_0 = z_{min}$, $z_{K+1} = z_{max}$ are the minimum and maximum of the z-range, to be entered as input parameters. The conditional mean value z'_k within each class, (z_{k-1}, z_k), is obtained by the interpolation procedure specified as input to CONSIM II.

The IK algorithm itself does not ensure that the resulting probability estimates (CCDFs for continuous variables or discrete probabilities for categorical variables), verify the order relations for legitimate probabilities, that is, for CCDFs of continuous variables $z(\mathbf{u})$:

$$\text{Prob}\{Z(u) \le z|(n)\} = F(u; z|(n)) \in [0,1] \quad \text{and} : F(u; z_{k'}|(n)) \ge F(u; z_k|(n)), \ \forall \ z_{k'} > z_k . \quad (25)$$

For conditional probabilities of an exhaustive set of mutually exclusive categorical variables $I_k(\mathbf{u})$, $k = 1,..., K$:

$$\text{Prob}\{I_k(u) = 1|(n)\} = F(u; k|(n)) \in [0,1] \quad \text{and} : \sum_{k=1}^{K} F(u; k|(n)) = 1 \quad (26)$$

The indicator $i_k(\mathbf{u})$ is set to 1 if category k prevails at location $\mathbf{u}$, to zero if not.

The flexibility of the IK approach is obtained at the cost of order relation problems. IK-derived conditional probabilities may not verify the order relations conditions (Eq. 25 or 26). In any particular study, one would expect to meet at least one order relation deviation for up to one-half or two-thirds of the IK-derived CCDFs. Fortunately, the average magnitude of the probability corrections is usually on the order or 0.01, much smaller than shown on Figure TFIELD-16. CONSIM II provides statistics of the order relation problems encountered, if desired.

In the case of categorical probabilities, the first constraint (Eq. 25) is easily met by resetting the estimated value $F^*(\mathbf{u}; z|(n))$ to the nearest bound, 0 or 1, if originally valued outside the interval [0,1]. This resetting corresponds exactly to the solution provided by quadratic programming.

The second constraint (Eq. 26) is tougher because it involves K separate krigings. One solution consists of kriging only (K - 1) probabilities leaving aside one category k_0, chosen with a large enough prior probability p_{k0}, so that:

$$F^*(u;k_0|(n)) = 1 - \sum_{k \neq k_0} F^*(u;k|(n)) . \quad (27)$$

Another solution, applied after the first constraint (Eq. 25) has been met, is to restandardize each estimated probability $F^*(\mathbf{u}; k|(n)) \in [0,1]$ by the sum $\sum_k F^*(\mathbf{u}; k|(n)) < 1$.

Correcting for order relations of continuous variable CCDFs is more delicate, because of the ordering of the cumulative indicators. There are two sources of order relation problems:

1. Negative indicator kriging weights. One solution is to constrain the IK system to deliver only non-negative weights. One would have to forfeit, however, the sometimes beneficial properties of having a non-convex kriging estimate.

2. Lack of data in some classes; see hereafter.

Practice has shown that the majority of order relation problems are due to a lack of data, more precisely, to cases when IK is attempted at a cutoff z_k which is the upper bound of a class (z_{k-1}, z_k) that contains no z-data. In such cases, the indicator data set is the same for both cutoffs z_{k-1} and z_k and yet the corresponding indicator variogram models are likely different; therefore, the resulting CCDF values will likely be different with a good chance for order relation problems.

Figure TFIELD-16 shows an example with the following order relation problems:

$$\begin{aligned} &F(u;z_3|(n)) < F(u;z_2|(n)) \\ &F(u;z_8|(n)) < F(u;z_7|(n)) \\ &F(u;z_9|(n)) > 1 \end{aligned} \quad (28)$$

TFIELD.3.1.6 CONSIM II: The Sequential Simulation Approach

The most straightforward algorithm for generating realizations of a multivariate Gaussian field is provided by the sequential principle described in this section. Each variable is simulated sequentially according to its normal CCDF fully characterized through an SK system of Eq. 22 for sequential Indicator Categorical Simulation (iCs) or Eq. 15 for Sequential Gaussian Simulation (sGs). The conditioning data consist of all original data and all previously simulated values found within a neighborhood of the location being simulated. CONSIM II will first simulate the categorical variable using sequential indicator categorical simulation and will then conduct a sequential gaussian simulation within each category to "fill in" the spatial variability.

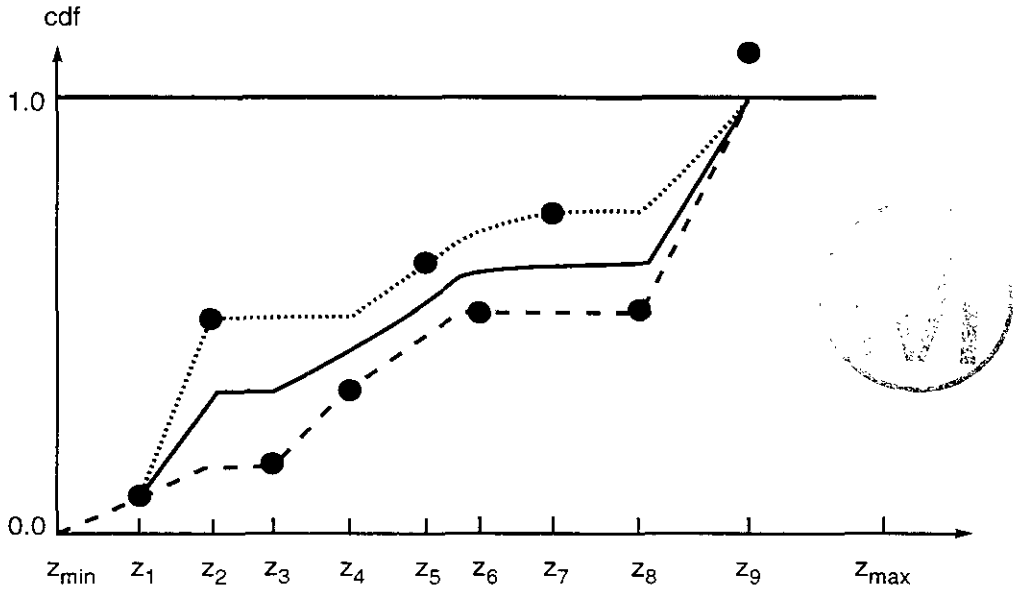

Note: The dots are the CCDF values returned by indicator kriging. The corrected CCDF is obtained by averaging the forward and downward corrections.

Figure TFIELD-16. Order Relation Problems and Their Correction

1 THIS PAGE INTENTIONALLY LEFT BLANK

The Sequential Simulation procedure may be summarized as follows. Consider the joint distribution of N random variables Z_i with N very large. The N RV's Z_i may represent the same attribute at the N nodes of a dense grid discretizing the field, or they can represent N different attributes measured at the same location, or they could represent a combination of K different attributes defined at the N' nodes of a grid with $N = KN'$.

Next, consider the conditioning of these N RV's by a set of n data of any type symbolized by the notation $l(n)$. The corresponding N-variate CCDF is denoted:

$$F_{(N)}(z_1,..., z_N|(n)) = \text{Prob}\{Z_i \le z_i, i = 1,..., N|(n)\}. \quad (29)$$

Equation 29 is completely general with no intrinsic limitations; some or all of the variables Z_i could be categorical.

Successive application of the conditional probability relation shows that drawing an N-variate sample from the CCDF (Eq. 29) can be done in N successive steps, each involving a univariate CCDF with increasing levels of conditioning:

- draw a value $z_1^{(l)}$ from the univariate CCDF of Z_1 given the original data (n). The value $z_1^{(l)}$ is now considered as a conditioning datum for all subsequent drawings; thus, the information set (n) is updated to $(n + 1) = (n) \cup \{Z_1 = z_1^{(l)}\}$.
- draw a value $z_2^{(l)}$ from the univariate CCDF of Z_2 given the updated data set $(n + 1)$, then update the information set to $(n + 2) = (n + 1) \cup \{Z_2 = z_2^{(l)}\}$.
- sequentially consider all N RV's Z_i.

The set $\{z_i^{(l)}, i = 1,..., N\}$ represents a simulated joint realization of the N dependent RV's Z_i. If another realization is needed, $\{z_i^{(l')}, i = 1,..., N\}$, the entire sequential drawing process is repeated.

This sequential simulation procedure requires the determination of N univariate CCDFs, more precisely:

$$\begin{aligned} &\text{Prob}\{Z_1 \le z_1|(n)\} \\ &\text{Prob}\{Z_2 \le z_2|(n + 1)\} \\ &\text{Prob}\{Z_3 \le z_3|(n + 2)\} \\ &\ldots \\ &\text{Prob}\{Z_N \le z_N|(n + N - 1)\}. \end{aligned} \quad (30)$$

The sequential simulation principle is independent of the algorithm or model used to establish the sequence (Eq. 30) of univariate CCDFs. In sGs, all CCDFs (Eq. 30) are assumed Gaussian and their means and variances are given by a series of N simple kriging systems. In iCs, the CCDFs are obtained directly by IK.

TFIELD.3.1.6.1 Indicator Categorical Simulation (iCs)

CONSIM II begins by assuming that the observed data $T(\mathbf{u})$ can be divided into mutually exclusive categories s_k, $k = 1,..., K = cat.$

$$i_k(u)=\begin{cases}1 \text{ if } T(u)\in s_k \\ 0 \text{ otherwise}\end{cases}. \tag{31}$$

Note that each $T(\mathbf{u})$ can only fit into one category s_k. Also note that at any location $\mathbf{u}$ we can define a probability of the $T(\mathbf{u})$ falling into a category s_k as

$$p_k(u) = p\{T(u) \in s_k\}. \tag{32}$$

The field $T(\mathbf{u})$ is simulated as follows:

1. Code all observed $T(\mathbf{u})$ into categories, that is,

x_1	y_1	z_1	T_1	s(1)
x_2	y_2	z_2	T_1	s(2)
x_α	y_α	z_α	T_α	s(α)

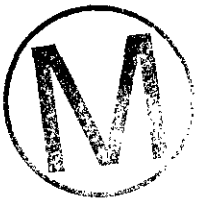

where $s(\alpha) = 1, 2,..., k$ as input; also provide: variograms for s_k and global p_k (for simple kriging).

2. Select a category s_k, indicator transform using

$$i_k(u_\alpha)=\begin{cases}1 \text{ if } s(\alpha)\in s_k \\ 0 \text{ otherwise}\end{cases} \tag{33}$$

3. Krige

$$[i_k(u|u_\alpha)]^* = \text{Prob}\{T(u) \in s_k | s(u_\alpha)\} = p_k^*(u|\alpha), \tag{34}$$

that is, krige the indicator of category s_k, which is the estimated probability of category s_k at the unknown location.

4. Repeat 2 and 3 for the $k = 1, 2, ..., K$ categories, correct for order relations so that

$$\sum_{k=1}^{K} p_k^*(u|s_k(u_\alpha)) = 1. \quad (35)$$

5. Use the $p^*_k(\mathbf{u})$ as an empirical CDF $F_{s_k}(s_k)$ of $P\{s(\mathbf{u}) \in s_k\}$; generate a random $\mathbf{u}[0,1]$ and invert $F_{s_k}(s_k)$ to get a simulated s_k as S^*_k.

6. Go to a new random location u, and repeat steps 2 through 5.

Within each simulated category we can now simulate $T^*(u) = T(u)|s(u)s_k$ using the sGs algorithm as described in Section TFIELD.3.1.6.2.

Figure TFIELD-17 illustrates an example of a categorical simulation over a model domain using two categories.

TFIELD.3.1.6.2 *Sequential Gaussian Simulation (sGs)*

The conditional simulation (CS) of a *continuous* variable $T(\mathbf{u})$ modeled by a Gaussian-related stationary RF $T(\mathbf{u})$ proceeds as follows:

1. Determine the univariate CDF $F_z(T)$ representative of the entire study area and not only of the t-sample data available. Declustering may be needed if the T-data are preferentially located.

2. Using the CDF $F_z(T)$ perform the normal score transform of T-data into y-data with a standard normal CDF.

3. Check for bivariate normality of the normal score y-data. If the multivariate Gaussian model can not be retained, then consider an indicator-based algorithm for the stochastic simulation.

4. If a multivariate Gaussian RF model can be adopted for the y-variable, proceed with program `sgsim` and sequential simulation, that is,

   - Define a random path that visits each node of the grid (not necessarily regular) once. At each node $\mathbf{u}$, retain a specified number of neighboring conditioning data including both original y-data and previously simulated grid node y-values.

   - Use SK with the normal score variogram model to determine the parameters (mean and variance) of the CCDF of the RF $y(\mathbf{u})$ at location $\mathbf{u}$.

   - Draw a simulated value $y^{(l)}(\mathbf{u})$ from that CCDF.

- Add the simulated value $y^{(1)}(\mathbf{u})$ to the data set.
- Proceed to the next node, and loop until all nodes are simulated.

5. Backtransform the simulated normal values $\{y^{(1)}(\mathbf{u}), \mathbf{u} \in A\}$ into simulated values for the original variable $\{T^{(1)}(\mathbf{u}) = \varphi^{-1}(y^{(1)}(\mathbf{u}), \mathbf{u} \in A\}$. Within-class interpolations and tail extrapolations are usually called for; see Section TFIELD.3.1.2.

Figures TFIELD-18 and TFIELD-19 illustrate the sGs for the categorical simulation shown in Figure TFIELD-17. Note that each sGs is independent of the other. Combining Figures TFIELD-18 and TFIELD-19 produces one CS field for a two-categorical problem. The grey scale in Figures TFIELD-18 and TFIELD-19 is presented in $\log_{10}$ meters squared per second units.

TFIELD.3.1.6.3 Implementation Considerations

Strict application of the sequential simulation principle calls for the determination of more and more complex CCDFs, in the sense that the size of the conditioning data set increases from (n) to $(n + N - 1)$. In practice, the argument is that the closer data screen the influence of more remote data; therefore, only the closest data are retained to condition any of the N CCDFs (Eq. 35). Because the number of previously simulated values may become overwhelming as i progresses from 1 to $N >> n$, one may want to give special attention to the original data (n) even if they are more remote.

The neighborhood limitation of the conditioning data entails that statistical properties of the $(N + n)$ set of RVs will be reproduced only up to the maximum distance found in the neighborhood. For example, the search must extend at least as far as the distance to which the variogram is to be reproduced; this requires extensive conditioning as the sequence progresses from 1 to N. Gomez-Hernandez and Wen (1993) has suggested that sequential algorithms such as sGs can fail to adequately reproduce the long-range spatial correlations of some fields; this problem may be particularly pronounced for covariance functions models with zonal anisotropy. This situation can occur when the random sequence of simulated locations fails to populate the field at long distances early enough in the sequence so that the simulated values do not reflect the effects of the long distance correlations.

To circumvent this situation, CONSIM II uses a multigrid approach, a type of stratified random sampling, to force the sequential simulation to visit widely separated locations early in the sequence (Gomez-Hernandez and Cassiraga 1994). The multigrid approach involves setting up an initial coarse grid, each point of which is visited randomly in the sequential simulation. Subsequent finer grids are superimposed and simulated until the grid spacing is reduced to the desired resolution. Because the multigrid approach requires the sequential simulation algorithms to visit widely-spaced locations first, it helps the simulations retain the long distance spatial correlation structure specified as input.

Note: Black dots indicate boreholes that are associated with Category 1; white dots are boreholes associated with Category 2.

Figure TFIELD-17. Example of Categorical Simulation over a Model Domain using Two Categories

1 THIS PAGE INTENTIONALLY LEFT BLANK

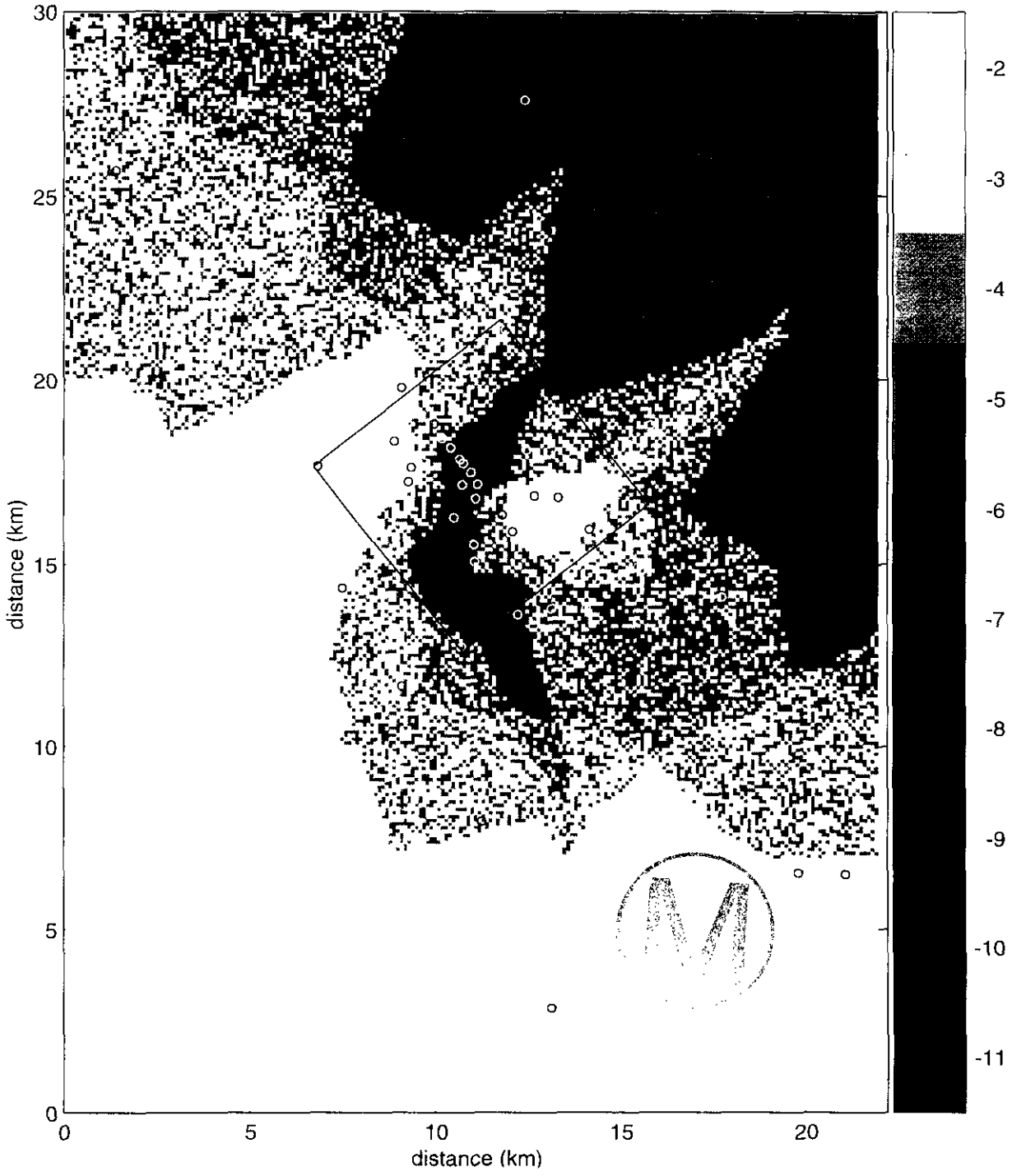

Figure TFIELD-18. Sequential Gaussian Simulation (sGs) for Category 1

THIS PAGE INTENTIONALLY LEFT BLANK

Figure TFIELD-19. Sequential Gaussian Simulation (sGs) for Category 2

1 **THIS PAGE INTENTIONALLY LEFT BLANK**

Theory does not specify the sequence in which the *N* nodes should be simulated. Practice has shown, however, that it is better to consider a random sequence. Indeed, if the *N* nodes are visited row-wise, any departure from rigorous theory may entail a corresponding spread of artifacts along rows.

TFIELD.3.1.7 CONSIM II: Connection to SWIFT II

Once the simulation (that is, generation) of the transmissivity field is complete by CONSIM II, information concerning the transmissivity field is passed to the SWIFT II flow model finite difference grid. The details for each SWIFT II block that are passed from CONSIM II to SWIFT II include

1. The simulated (estimated) log transmissivity
2. A lower bound for the log transmissivity
3. An upper bound for the log transmissivity
4. The category for the block
5. A flag that can prohibit the block from being selected as a pilot point

CONSIM II generates items 1 through 4 for every point on the simulation grid as discussed in the previous sections. It then generates the same four items for every block on the SWIFT II grid by averaging. After the averaging is done, the simulation grid is effectively discarded, that is, not used further by GRASP-INV.

To find transmissivities and a category for a SWIFT II grid block, the block must contain at least one simulated point. If not, a large negative (for example -99) value is assigned to the log transmissivity and its bounds, and the category for the block is set to 0. Subsequently, SWIFT II will *not* over-write the values read from its input file for the conductivities for the block.

If there is at least one refined point within a SWIFT II grid block, simulated transmissivity values from each contained point are averaged to find a value for the SWIFT II block. There are two different approaches taken depending on the type of refined grid. If the refined grid is irregular, the geometric mean of the simulated transmissivities is calculated. If the refined grid is regular, an analog to resistance computations for an electrical circuit is used.

For an irregular grid (this includes the Gauss points used by the previous version of GRASP-INV) the arithmetic mean of the logarithms of the transmissivities for the included points is found. This is equivalent to finding the geometric mean of the transmissivities themselves. The arithmetic mean is found by summing the log transmissivities contained in the block and dividing by their number.

For a regular grid, the first assumption is that each refined point has equal weight, that is, comprises an equal volume within the SWIFT II grid block. A principal direction is selected and the SWIFT II grid block is partitioned into a sequence of slices, where each slice is perpendicular to that direction. Fluid entering the block must traverse each slice. If there is more than one refined point within a slice, the fluid has more than one path through the slice. This is analogous to resistance in parallel in an electrical circuit. Resistors in parallel have a total resistance found by the inverse of the sum of the inverses of the individual resistors. Since transmissivity is inversely proportional to resistance, the transmissivity for a slice is found from the sum of the transmissivities for the refined points within the slice. Each slice must be traversed in sequence. This is analogous to resistance in series. Resistors in series have total resistance equal to the sum of the individual resistors. Again applying the inverse relation between resistance and transmissivity, the average transmissivity across all slices is the inverse of the sum of the inverses of the individual slice transmissivities.

In two dimensions a slice is a row or column of refined points. In three dimensions, a slice is comprised of points in a plane. CONSIM II finds the directional transmissivity for each SWIFT II grid block in the x and y directions (T_x and T_y) using the electrical analogue. The equivalent horizontal conductivity is then the geometric mean, $T_h = (T_x\, T_y)^{1/2}$. The calculations conducted are illustrated below for a two-dimensional problem.

TFIELD.3.1.7.1 Upscaling Example - Electrical Analog

Consider a geostatistical simulation grid of 25×25 (x,y), with 1 meter grid spacing in each direction. Assume the SWIFT II grid is 7×7 (x,y), with grid spacing equal to 3.6 meters in the x and y directions. This example will illustrate the method used to upscale the results of the geostatistical simulation to the SWIFT grid. This example is designed such that each SWIFT II grid block will contain 3 or 4 simulation points in the x-direction and 3 or 4 in the y-direction. The simulation points that reside within a SWIFT II grid block will be averaged together to determine a transmissivity value assigned to the SWIFT II grid block. In this example, the simulation grid is created internally by CONSIM II. This is done by specifying the location option as zero (in catg and sgsim input files) and providing the number of blocks and their (equal) size in each direction.

When the simulation grid is generated internally, that is, the grid is equally spaced, CONSIM II finds an average horizontal transmissivity using the analogue of electrical resistance. The electrical analogue approach to finding the average horizontal transmissivity considers flow through slices in each direction. To traverse a single slice, fluid has a choice of paths, which is analogous to resistance in parallel. To traverse all slices, fluid must cross each slice, which is analogous to resistance in series.

As an example, assume the simulated log transmissivities falling within a SWIFT II grid block have the transmissivity and category values listed in Table TFIELD-4 below.

Table TFIELD-4. Simulated Log_{10} Transmissivities and Categories Falling Within a SWIFT II Grid Block for Upscaling Example

x	y	Value	Category*
1.5	1.5	1.0	1
2.5	1.5	1.0	1
3.5	1.5	1.0	1
1.5	2.5	0.0	2
2.5	2.5	0.0	2
3.5	2.5	0.0	2
1.5	3.5	-1.0	2
2.5	3.5	-1.0	2
3.5	3.5	-1.0	2

*1-high transmissivity
2=low transmissivity

CONSIM II makes the assumption that each simulated point comprises an equal portion of the volume of the SWIFT II grid block that contains it. So for a SWIFT II grid block which has nine simulated points falling within it, the weights assigned to these points would be the same. Table TFIELD-5 depicts the locations of the transmissivity values listed above within the SWIFT II grid block.

Table TFIELD-5. Simulated Transmissivities Lying Within a SWIFT II Grid Block For Upscaling Example

0.1	0.1	0.1
1.	1.	1.
10.	10.	10.

As mentioned above, the electrical analogue approach to finding the average horizontal transmissivity considers flow through slices in each direction. Traversing a single slice is analogous to resistance in parallel. Traversing all slices is analogous to resistance in series. In this example, the x-direction is analyzed first, where flow is assumed from left to right in Table TFIELD-5. Each slice is a column in Table TFIELD-5. The transmissivity for a slice is found by adding its transmissivities. Calling the three columns slice 1, slice 2, and slice 3, their transmissivities are

Slice 1 transmissivity = 11.1
Slice 2 transmissivity = 11.1

Slice 3 transmissivity = 11.1

To traverse all three slices (analogous to encountering resistance in series), each slice transmissivity is inverted, the sum is found, and the result is inverted. Thus, the transmissivity in the x-direction, T_x, is given by

$$T_x = [(1/11.1) + (1/11.1) + (1/11.1)]^{-1} = 3.7$$

For the y-direction the same approach is taken only this time each slice is a row of Table TFIELD-5. The slice transmissivities for the rows are:

Slice 1 transmissivity = 0.3
Slice 2 transmissivity = 3.0
Slice 3 transmissivity = 30.

Thus, the transmissivity in the y-direction, T_y, is given by

$$T_y = [(1/0.3) + (1/3.0) + (1/30.)]^{-1} = 0.27027$$

Horizontal transmissivity, T_h, is then estimated by the geometric mean of T_x and T_y. Thus,

$$T_h = (T_x\, T_y)^{1/2} = 1.0$$

The $\log_{10}$ of T_h is 0.0.

The other variable that is upscaled to the SWIFT II grid block is the category variable. The category that is assigned to the SWIFT II grid block is the most frequent amongst the simulation points within the block. In case of ties, the lowest category number involved in the tie is selected and assigned to the block. In the example above, Category 2 would be assigned to the SWIFT II grid block because of the larger number of Category 2 values falling within the block.

CONSIM II does not calculate the vertical direction transmissivity because it is assumed that conditioning data is based on horizontal transmissivities. SWIFT II will calculate vertical conductivity by converting the horizontal transmissivity computed here to horizontal conductivity and multiplying by the nominal value of anisotropy.

TFIELD.3.1.7.2 Upscaling Example - Geometric Mean

Consider the same grid used in the previous example of Section TFIELD.3.1.7.1. The geostatistical simulation grid is 25×25 (x, y), with 1-meter grid spacing in each direction. The SWIFT II grid is 7×7 (x, y), with grid spacing equal to 3.6 meters in the x and y directions. The example is designed such that each SWIFT II grid block will contain 3 or 4 simulation points in the x-direction and 3 or 4 in the y-direction. The simulation points that reside within a SWIFT II grid block will be averaged together to determine a transmissivity

value assigned to the SWIFT II grid block. In this example, the simulation grid is read from a text file. This is done by specifying the location option as 1 (in catg and sgsim input files) and providing the name of the text file and the columns to use on the file. When the simulation grid is provided on a text file, the geometric average of transmissivities found within a SWIFT II block is used as demonstrated below.

Assume the simulated log transmissivities falling within a SWIFT II grid block have the transmissivity and category values as listed in the previous example (Table TFIELD-4). The geometric mean transmissivity taken over all the simulation values within the block is equivalent to calculating the arithmetic mean of the log transmissivities. Summing all values listed in Table TFIELD-4 and dividing by 9 gives a mean $\log_{10} T_h$ value of 0.0. (Note: The sample used gave equivalent values between the electric analog and geometric mean upscaling calculations, which is not usually the case.)

TFIELD.3.1.7.3 Summary

The steps used to upscale the geostatistical simulation results to the SWIFT grid are summarized as follows:

1. Use the electrical current analog to groundwater flow to find average transmissivity in the x-direction, T_x,
2. Use the electrical current analog to groundwater flow to find average transmissivity in the y-direction, T_y,
3. Find the equivalent horizontal isotropic transmissivity, $T_h = (T_x T_y)^{1/2}$,
4. Convert T_h to conductivity K_h by dividing by block thickness,
5. Estimate vertical conductivity K_v by multiplying K_h by the nominal anisotropy factor, and
6. Use K_h for both K_x and K_y in SWIFT II and use K_v for K_z.

Note the following with regard to block thickness in Step 4. Initially all blocks in a horizontal layer have the same thickness. Nonuniform thicknesses can be provided to SWIFT II either through the R1-21 cards or the R1-26 cards. The grid block thickness used above is the thickness established after the R1-21 cards are read, but before the R1-26 cards are read. So in GRASP-INV, it is recommended that thicknesses *not* be modified using the SWIFT II R1-26 cards.

CONSIM II uses the same approach, depending on the type of simulation grid, to find minimum and maximum values for transmissivity in each block. Instead of simulated values, it substitutes the minimum and maximum bounds for each simulated point during the averaging process. This substitution produces a minimum and maximum log transmissivity

for the SWIFT II grid block. Note that the bounds were originally symmetric when simulation was being performed on the normal scores. Symmetry is generally lost during back transformation to original data, and can be further diminished during the averaging processes described above.

In the GRASP-INV scheme, the simulated SWIFT II grid is used as an initial estimate for the calibration process. At each step of the calibration, a pilot point(s) is found and its transmissivity is modified, along with that of grid blocks "nearby." Pilot point locations are selected from the set of SWIFT II grid block centers. If the location of a conditional data point coincides with a SWIFT II grid block center, the center should *not* be an eligible pilot point. That is, the transmissivity at such a point must be honored and therefore must not be modified.

Each conditioning data point is located on the SWIFT II grid. Its distance to the center of the block is computed, *wd*. The diagonal distance from the block center to a block corner is also computed, *cd*. If the ratio *wd* / *cd* is less than a specified fraction, the data point is considered to fall on the grid block center. Currently, the specified fraction is 0.2. Note that this test and restriction apply only if the data point and the grid block are of the same category.

TFIELD.3.2 SWIFT II

The groundwater flow model of the Culebra was developed using the computer code SWIFT II. SWIFT II (Sandia Waste Isolation, Flow, and Transport code) is a fully transient, three-dimensional, finite difference code that solves the coupled equations for single-phase flow and transport in porous and fractured geologic media, where the mass per unit volume, ρ, is a function of the concentration of the transported constituents. The SWIFT II code is supported by comprehensive documentation and extensive testing. The theory and implementation of SWIFT II are given by Reeves et al. (1986) and the data input guide is given by Reeves et al. (1987). Finley and Reeves (1981) and Ward et al. (1984) present the verification-validation tests for the code.

The transient flow equation solved by SWIFT II is given by

$$\nabla \bullet \left[\frac{(\rho k)}{\mu} (\nabla p - \rho g \nabla z) \right] + q = \frac{\partial (\phi \rho)}{\partial t}, \qquad (36)$$

where $k = k(\boldsymbol{x})$ is permeability tensor, $p = p(\mathbf{x}, t)$ is pressure, z is the vertical coordinate and is considered positive downward, $\rho = \rho(\mathbf{x})$ is fluid density, q is flux sources or sinks, g is the gravitational constant, μ is fluid viscosity, ϕ is rock porosity, $\mathbf{x}$ is the position vector, and t is time. Discretized, (Eq. 36) becomes a matrix equation of the form

$$[A]\{p\}^n = [B]\{p\}^{n-1} + \{f\}^n, \qquad (37)$$

where, for the fully implicit scheme of time integration in SWIFT II, [A] = [C] + [S]/Δt_n, [B] = [S]/Δt_n, [C] is the conductance matrix, [S] is the storativity matrix, [*f*] is the load vector, $\Delta t_n = t^n - t^{n-1}$, *t* is time, *n* is the time level (for example, 1,2,..., *L*) is the maximum time level of the simulation.

TFIELD.3.3 GRASP II

Adjoint Sensitivity Analysis and Kriging

The GRASP II (groundwater adjoint sensitivity program) code computes measures of the behavior of a groundwater system typically based on pressures or heads at a location or several locations. It then calculates the sensitivities of these measures to system parameters (for example, permeabilities and prescribed pressure values at the boundaries). The computed measures are referred to as "performance measures" and may include weighted spatial sums of groundwater pressures at selected locations or weighted squared deviations of computed and observed pressures at selected locations (or boreholes).

The sensitivities are computed by the adjoint method (Chavent 1971) and are derivatives of the performance measures with respect to the parameters for the modeled system, taken about the assumed parameter values. The system parameters available for use with GRASP II are (1) $\log_{10}$ transmissivity assigned to a pilot point (see below), (2) grid block permeabilities or transmissivities, (3) prescribed pressure values at the boundaries, (4) recharge, and (5) source/sink rates. In the application to be used by WIPP performance assessment, weighted sums of the squared differences between calculated and observed groundwater pressures at selected boreholes will be the chosen performance measures, and transmissivities assigned to pilot points will be the chosen system parameter used during model calibration.

GRASP II presumes either steady state or transient state saturated groundwater flow conditions and postprocesses the results from a SWIFT II flow simulation. The theory and verification for the steady state flow sensitivity equations used in GRASP II are presented by Wilson et al. (1986), while those for the transient flow sensitivity equations are presented by RamaRao and Reeves (1990). For completeness, a brief presentation of the pertinent equations solved by GRASP II during this study is given below.

A conventional approach to the evaluation of sensitivity coefficients is defined by the expression

$$J = f(\alpha, p), \tag{38}$$

where *J* is a performance measure and α is a vector of sensitivity parameters. Let α_l be the parameter for which a sensitivity coefficient is sought. Then

$$dJ/d\alpha_l = \partial J/\partial \alpha_l + \partial J/\partial p \bullet \partial p/\partial \alpha_l. \tag{39}$$

The first term on the right-hand side of (39) represents the sensitivity resulting from the explicit dependence of J on α_l and is called the direct effect. The second term represents an indirect effect due to the implicit dependence of J on α_l through the system pressures, $p(\alpha)$. While the computation of the direct effect is a trivial step, that of the indirect effect involves the evaluation of the state sensitivities; $\partial p(\mathbf{x}, t)/\partial\alpha_l$. State sensitivities may be calculated by the "parameter-perturbation approach" (Yeh 1986) or by solution of the partial differential equation for state sensitivity (Sykes et al. 1985; Yeh 1986). However, these approaches require the state sensitivities to be recomputed whenever a new parameter is considered. In a numerical model with a large number of grid blocks/elements and different system parameters, this represents an enormous computational effort of the same order as in the multiple simulation approach to parameter sensitivity.

The adjoint sensitivity approach circumvents the need to compute state sensitivities. This is done by expressing the performance measure as the sum of two distinct terms, one containing, exclusively, the partial variations with respect to the pressure function and the second containing partial variations with respect to α_l (RamaRao and Reeves 1990). Both terms include a function referred to as the adjoint state. The adjoint state is computed such that it greatly facilitates the evaluation of the second term on the right-hand side of (Eq. 39). The adjoint state vector λ is obtained by solving the following equation:

$$[A]\{\lambda\}^{n-1}=[B]\{\lambda\}^{n} + [\partial J/\partial\{p^{n}\}^{T}]^{T}, \tag{40}$$

where T denotes the transpose of the matrix, A and B are the same matrices used in the primary problem (that is, pressure solution) solved by SWIFT II, and J is the performance measure (for example, the cumulative sum of squared pressure deviations between calculated and observed pressures). The solution of (Eq. 40) permits the evaluation of parameter sensitivities by the following expression:

$$\frac{dJ}{d\alpha_i}=\frac{\partial J}{d\alpha_i}+\sum_{n=1}^{L}\left\{\lambda^{n}\right\}^{T}\cdot\left[\frac{\partial[A]}{\partial\alpha_i}\{p\}^{n}-\frac{\partial[B]}{\partial\alpha_i}\{p\}^{n-1}-\frac{\partial\{f^{n}\}}{\partial\alpha_i}\right] \tag{41}$$

The fact that there are not state sensitivity terms in the above expression leads to one important feature of the adjoint method, namely, the separation of the relatively time-intensive calculation of the adjoint state vector λ in (Eq. 40) from the relatively non-time-intensive calculation of the sensitivity derivative (Eq. 41). In general, this separation permits the calculation of sensitivity derivatives for all of the system parameters using the same adjoint state vector $[\lambda\}$, a major advantage over the perturbation approach.

TFIELD.3.3.1 GRASP II: Objective Function

The objective function that is minimized during calibration is a weighted least square error criterion function which is a model fit criterion. The model fit criterion is a weighted sum of

the squared deviations between the computed and measured pressures taken over all points in spatial and temporal domains where pressure measurements have been made.

For a purely steady state simulation, the objective function (also called performance measure) is given by:

$$J_s(\underline{u}) = \sum_{i=1}^{n} w_i \left(p_i - p_{ob,i}\right)^2, \quad (42)$$

where,

$J_s(\underline{u})$ = objective function for steady state,
n = number of boreholes,
i = suffix for the borehole,
P = calculated pressure,
$P_{ob,i}$ = observed pressure, and
w_i = weight assigned to the borehole.

For transient simulation, similarly

$$J_t(\underline{u}) = \sum_{t_1}^{t_2} \sum_{i=1}^{n} w_{i,t} \left(p_{i,t} - p_{ob\,i,t}\right)^2, \quad (43)$$

where,

$J_t(\underline{u})$ = objective function for transient state,
t_1 = the beginning of the time window,
t_2 = the end of the time window, and
w = weight assigned to selected borehole for a given time t.

The transient performance measure may consist of short transient events during which a response is only observed at a single location or long-term events during which responses are observed at several locations.

In practice, the steady state calibration is undertaken first. Subsequently, the transient calibration is taken up. It is necessary to ensure that the fit between calculated and observed pressures be improved during transient calibration without degrading the fit to the steady state calibration. From experience, it has been found that this requires that the contributions from the steady state and the transient state to the combined performance measure should be

approximately equal. Since transient performance measures can be generally much larger than the steady state performance measures (because values are summed up in the time window), an additional factor f is used to ensure that the steady state performance measure and the transient performance measure are approximately equal in the combined performance measure $J(\underline{u})$.

$$J(\underline{u}) = f\, J_s(\underline{u}) + J_t(\underline{u}), \tag{44}$$

where,

$J(\underline{u})$ = combined steady and transient objective function, and
f = weight factor for steady state objective function.

Also,

$$f\, J_s(\underline{u}) \approx J_t(\underline{u}) \tag{45}$$

$$f \approx \frac{J_t(\underline{u})}{J_s(\underline{u})},$$

TFIELD.3.3.2 GRASP II: Adjoint Sensitivity Analysis

Adjoint sensitivity analysis provides an extremely efficient algorithm for computing sensitivity coefficients between a given objective function J and a large number of parameters (permeabilities in thousands of grid blocks, as is the case here).

Let the groundwater flow model be represented by the following matrix equation:

$$\underline{\underline{A}}\,\underline{p}^{n} = \underline{\underline{B}}\,\underline{p}^{n-1} + \underline{f}^{n}, \tag{46}$$

where for a fully implicit scheme of time integration adopted here:

$\underline{p}$ = vector of gridblock pressures,
$\underline{\underline{A}} = \underline{\underline{C}} + \underline{\underline{B}}$,
$\underline{\underline{B}} = \underline{\underline{S}}/\Delta t$,
$\underline{\underline{C}}$ = conductance matrix,
$\underline{\underline{S}}$ = storativity matrix,
$\underline{f}^{n}$ = vector of source terms,
$\Delta t = t^{n} - t^{n-1}$,
t = time,
n = time level (1,2,3...L), and

L = maximum time level of the simulation.

First, an adjoint state vector $\{\lambda\}$ is obtained by the solution of the following equation:

$$\underline{\underline{A}}\lambda^{n-1} = \underline{\underline{B}}\lambda^{n} + \left[\frac{\partial J}{\partial \underline{p}^{n}}\right]^{T}, \tag{47}$$

where T denotes the transpose of the matrix.

Equation 47 is solved backwards in time, from n = L to n = 1 with

$$\underline{\lambda}^{L} = 0. \tag{48}$$

If a_i is a generic sensitivity parameter in the gridblock i, the sensitivity coefficient dJ/da_i is evaluated by the expression:

$$\frac{dJ}{d\alpha_i} = \frac{\partial J}{\partial \alpha_i} + \sum_{n=1}^{L} \underline{\lambda}^{nT} \bullet \left[\frac{\partial \underline{\underline{A}}}{\partial \alpha_i}\underline{p}^{n} - \frac{\partial \underline{\underline{B}}}{\partial \alpha_i}\underline{p}^{n-1} - \frac{\partial \underline{f}^{n}}{\partial \alpha_i}\right]. \tag{49}$$

Here, Equation 49 is evaluated with $\alpha_i = K_i$, the permeability in the grid block.

TFIELD.3.3.3 GRASP II: Locating Pilot Points

De Marsily et al. (1984) pioneered the concept of pilot points as parameters of calibration. He assigned their locations based on some considerations. In GRASP-INV, LaVenue and Pickens' (1992) approach to location of pilot points is followed. Pilot points are placed at grid-block center locations where their potential for reducing the objective function is the highest. This potential is quantified by the sensitivity coefficients (dJ/dY_p) of the objective function J, with respect to Y_p, the logarithm (to base 10) of pilot-point transmissivity. A large number of candidate pilot points are considered (as specified by the user), usually the centroids of all the grid blocks in the flow model grid. Each potential pilot point is initially described by an x,y,z location (grid block center) and a category type. The variograms for each category represented by the candidate pilot points and the number of neighboring grid blocks with the same category type is considered in the sensitivity equations.

Coupled adjoint sensitivity analysis and kriging is used to compute the required derivatives and the procedure is documented in RamaRao and Reeves (1990). It is described briefly here.

The user specifies the maximum number of pilot point locations to consider (for example, 50, 100). The code will then determine the grid blocks with the highest derivative $\frac{dJ}{dY_m}$ (see below) and then calculates $\frac{dJ}{dY_p}$ (see below) for these grid blocks only. It then reranks these grid blocks' $\frac{dJ}{dY_p}$ sensitivities and places a pilot point in the grid block with the highest sensitivity value. GRASP-INV then sends this new pilot point location to PAREST to optimize the pilot point's transmissivity value.

Let P be a pilot point added to a set of N observed transmissivity values within a particular category. Let T_p be the transmissivity assigned to pilot point P. Kriging is done using Y_p, where

$$Y_p = \log_{10} T_p . \tag{50}$$

The kriged estimate (Y*) at the centroid of a grid block m for this category is given by

$$Y_m^* = \sum_{k=1}^{N} \gamma_{m,k} Y_k + \gamma_{m,p} Y_p , \tag{51}$$

where k is the subscript for an observation point, p is the subscript for pilot point, $\gamma_{m,k}$ is the kriging weight between the interpolation point m and data point k, and $\gamma_{m,p}$ is the kriging weight between interpolation point m and pilot point p.

When a pilot-point transmissivity is perturbed, the kriged transmissivities and hence the conditionally simulated (CS) values in the neighboring grid blocks having the same category of the pilot point are altered, causing the objective function J to change. If a neighboring grid block belongs to another category, its CS value will not be affected by the addition of a nearby pilot point belonging to another category. Let Y_m^* represent the CS value assigned to grid block m. Using the chain rule,

$$\frac{dJ}{dY_p} = \sum_{m=1}^{M} \frac{\partial J}{\partial Y_m} \frac{\partial Y_m}{\partial Y_p} , \tag{52}$$

where M is the total number of grid blocks in the flow model.

$$\frac{\partial Y_m}{\partial Y_p} = \gamma_{m,p}, \tag{53}$$

where $\gamma_{m,p}$ is the linear weight between a pilot point and the finite-difference grid block centroid. This result is valid for a CS field also, because the kriging error is independent of the kriged values.

$$\frac{dJ}{dY_p} = \sum_{m=1}^{M} \frac{dJ}{dY_m^*} \bullet \gamma_{m,p} \tag{54}$$

$$Y_m^* = \log_{10}(T_m^*) \tag{55}$$

$$T_m^* = k_m \frac{\rho_m}{\mu_m} g b_m \tag{56}$$

$$\frac{dJ}{dY_m} = \ln(10) k_m \frac{dJ}{dk_m}, \tag{57}$$

where T* is the CS transmissivity, k is the CS permeability, ρ is fluid density, μ is fluid viscosity, g is acceleration due to gravity, b is grid block thickness, and m is the subscript denoting grid block.

Combining Eqs. 52, 53, and 54 yields

$$\frac{dJ}{dY_p} = \ln(10) \sum_{m=1}^{M} \gamma_{m,p} k_m \frac{dJ}{dk_m} \bullet \tag{58}$$

The sensitivity coefficient, dJ/dk_m of the objective function with respect to the permeability in a grid block m, is obtained by adjoint sensitivity analysis.

TFIELD.3.4 PAREST

PAREST comprises the optimization code used to assign transmissivities to selected pilot point locations. The optimization is essentially conducted in a two-step process. Given the parameter to be optimized, determine which direction to adjust its initial value (that is, increase or decrease). Once the direction is chosen, determine the optimal change or 'step length' in this direction. Details concerning these two parts of the optimization process are discussed below.

TFIELD.3.4.1 PAREST: Parameters of Calibration

The pilot-point transmissivities are the parameters that are adjusted for calibration. However, in the mathematical implementation, the logarithms (to base 10) of the transmissivities (and not the transmissivity) are treated as parameters. The calibration parameters are given by

$$Y_p = \log_{10} T_p, \tag{59}$$

where T_p is the transmissivity at a pilot point (suffix p denotes pilot point).

TFIELD.3.4.2 PAREST: Optimizing Pilot Point Transmissivity

The transmissivities at pilot points are assigned by an unconstrained optimization algorithm and a subsequent imposition of constraints. The optimization algorithm chosen here belongs to a class of iterative search algorithms. It involves a repeated application of the following equation until convergence is achieved:

$$\underline{Y}_{i+1} = \underline{Y}_i + \beta_i \bullet \underline{d}_i, \tag{60}$$

where i is the iteration index, $\underline{d}_i$ is the direction vector, β_i is the step length (a scalar), and $\underline{Y}_i$ is the vector of parameters to be optimized (that is, logarithms of pilot-point transmissivities to base 10).

The steps in the implementation of this algorithm are as follows:

1. For the selected number of pilot points, use the initial estimates of the pilot-point $\log_{10}$ transmissivity ($Y_p = \log_{10} T_p$), that is, the kriged values in the gridblocks where pilot points are located.

2. Compute the direction vector, $\underline{d}_i$, as per one of the three algorithms discussed below (Fletcher-Reeves, Broyden's, or Davidon-Fletcher-Powell). The direction vector constitutes a direction in the hyperspace of the parameters. By advancing along the direction vector, the new values of the parameters are obtained. The step length β determines the actual advance along this direction.

3. Determine the optimal step length β, which minimizes the objective function.

$$\beta_i \; J\left(\underline{Y}_{i+1}\right) = \min J\left(\underline{Y}_i + \beta_i \underline{d}_i\right),$$

4. Update the parameters:

$$\underline{Y}_{i+1} = \underline{Y}_i + \beta_i \underline{d}_i .$$

Impose the constraints.

5. Check for convergence.

6. If convergence is achieved, the optimization algorithm is completed and the pilot points are added to the data and passed to the CONSIMX code to modify the grid block transmissivity values which are then sent to SWIFT II

7. If convergence is not achieved, iterate within the optimization routine: using the augmented data set, modify the grid block tranmissivities with the CONSIMX code, derive the corresponding pressure field, and recompute the gradient vector using the already selected pilot point locations. (The pilot point selection process will be skipped. Go to Step 2 above.)

TFIELD.3.4.2.1 *Direction Vector: $\underline{d}_i$*

Three options for the computation of the direction vector $\underline{d}_i$ are considered. They are the algorithms due to (1) Fletcher-Reeves, (2) Broyden, and (3) Davidon-Fletcher-Powell (Carrera and Neuman 1986). These methods are well known in classical literature and are not described here. The details with respect to pilot point methodology are given by LaVenue and RamaRao (1992).

TFIELD.3.4.2.2 *Step Length: β_i*

The step length β_i, (a scalar) is determined by:

$$\beta_i \, J\left(\underline{Y}_{i+1}\right) = \min J\left(\underline{Y}_i + \beta_i \underline{d}_i\right). \qquad (61)$$

Thus, β_i is obtained by solving

$$\frac{\partial J\left(\underline{Y}_{i+1}\right)}{\partial \beta_i} = 0 . \qquad (62)$$

The solution of Eq. 62 follows from Carrera and Neuman (1986) and Neuman (1980). The details in respect to pilot points are presented in LaVenue and RamaRao (1992) and are not repeated here.

TFIELD.3.4.2.3 Constraints

It is possible that the optimization algorithms may dictate large changes in the transmissivities assigned to pilot points and bring about a reduction in the objective function. Such recommended large changes may be viewed as undesirable for several reasons. At any point in the field, one can obtain a kriged estimate of transmissivity and its variance (kriging variance). One may construct a confidence interval (assuming a normal distribution of kriging errors) for the transmissivity. It is reasonable to expect the calibrated value to be within the confidence band. A constraint may be imposed to achieve this.

There also may be situations where the confidence band is large. A large change in a pilot-point transmissivity value, even if contained within the confidence band, can cause a large change in the spatial correlation structure of the transmissivity field. One objective in calibration can then be to limit the maximum change to a specified value so that the geostatistical structure of the transmissivity field is not altered significantly.

Consider the kth parameter, whose value is Y_k (kth element in the vector of parameters, $\underline{Y}$). Then,

$$\Delta Y_{k,i} = \left(Y_{k,i+1} - Y_{k,i}\right), = \beta_i \bullet d_{k,i} \quad (63)$$

where i is an iteration index.

Constraint 1: The parameter value should lie within the confidence band.

$$Y_k - m\sigma_y \leq Y_{k,i+1} \leq Y_k + m\sigma_y . \quad (64)$$

Thus Y_k gives the kriged value at the location of k (the pilot point), σ gives the kriging variance at the same location, and m is the multiplier of the standard deviation, which gives the semi-width of the confidence band. GRASP-INV uses a 95 percent confidence band which is obtained from CONSIM II during the simulation of the transmissivity field (see Section TFIELD.3.1.7). The 95 percent confidence interval values are sent to PAREST as grid block minimum and maximum values and are therefore used as constraints during pilot point transmissivity optimization.

Constraint 2: The change in any parameters must be limited to ΔY_{max}.

$$\Delta Y_{k,i} \leq \Delta Y_{max} . \quad (65)$$

After the optimization, these constraints are implemented for each parameter. If a constraint becomes active (imposed), the optimal step length computed is reduced; however, the direction is preserved.

TFIELD.3.4.2.4 Convergence Criteria

Distinction Between Inner and Outer Iterations

There are two levels of iteration, designated as inner and outer iterations. During an outer iteration, optimal location of a set of pilot points is calculated using coupled kriging and adjoint sensitivity analysis. Subsequently, the transmissivities are optimized by a sequence of inner iterations. An inner iteration relates to the iterations needed to optimize the transmissivities of the pilot points once they have been located. Thus, if an inner iteration is repeated, the pilot point locations remain fixed and the optimization conducts a second iteration on the pilot-point transmissivity values. When the convergence of an inner iteration is achieved, the selected pilot points are added to the transmissivity data set. This then sets the stage for another outer iteration.

Convergence Criteria: Inner Iterations

The following criteria may be used to define convergence when optimizing the transmissivities assigned to a set of pilot points. These criteria are very similar to those employed by Carrera and Neuman (1986).

1. The performance measure (J) drops below a prescribed minimum value (JMIN):

$$J \leq JMIN.$$

2. The number of iterations (NITER) equals a prescribed maximum number of iterations, for the inner iterations (ITERMX1):

$$NITER \geq ITERMX1 .$$

3. The ratio of the norm of the gradient to the initial gradient norm reduces below a prescribed value (GRNR):

$$\frac{\|\underline{g}\|}{\|\underline{g}_0\|} \leq \underset{\text{(gradient norm ratio)}}{GRNR}$$

4. The gradient norm $\|\underline{g}\|$ is less than a prescribed minimum (GRMIN):

$$\|\underline{g}\| \leq GRMIN$$

5. The relative change in objective function is defined, as ΔJ/J, where ΔJ is the change in the objective function during one iteration. Iterations are terminated if this relative change falls below a prescribed value (RELCJ):

$$\frac{\Delta J}{J} \leq \text{RELCJ}$$

Convergence Criteria: Outer Iterations

Outer iterations are terminated essentially on criteria (1) and (2) of inner iterations.

TFIELD.3.5 Code Organization

Figure TFIELD-20 illustrates the overall code organization. Table TFIELD-6 lists the important subroutines and their functions.

TFIELD.4 Application

TFIELD.4.1 Description of the 1996 Culebra Model

TFIELD.4.1.1 Model Grid

The model boundaries and orientation used in this study are essentially the same as used by LaVenue and RamaRao (1992) for the 1992 performance assessment Culebra calculations (Figure TFIELD-21). The locations of the boundaries of the model were chosen to maximize the ability to use Nash Draw as a groundwater divide and to minimize the effect that the boundaries may have on the transient modeling results for the long-term pumping tests at the H-3, WIPP-13, H-11 and H-19 locations. The finite-difference grid used for this model domain was selected to facilitate the successful reproduction of both steady-state and transient heads. The grid consists of 108 × 100 × 1 (x,y,z) grid blocks and has a finer grid in the central portion of the model in the vicinity of H-3, H-11, WIPP-13, and the shafts (Figure TFIELD-22). Grid-block dimensions range from 100 meters near the center of the site to approximately 800 meters at the model boundary (Table TFIELD-7). Note that the grid used by GRASP-INV is referred to as the "regional grid," as discussed in Section 6.4 of the main report; it is not the "local grid" used in the transport calculations. The vertical dimension of the grid is taken from the thickness of the Culebra in the WIPP area. The mean thickness of 7.75 meters was calculated from the available data and was assumed suitable for the vertical model dimension in this study. The variable thickness of the Culebra is indirectly accounted for because the transmissivities were interpreted from the transient tests conducted at the WIPP.

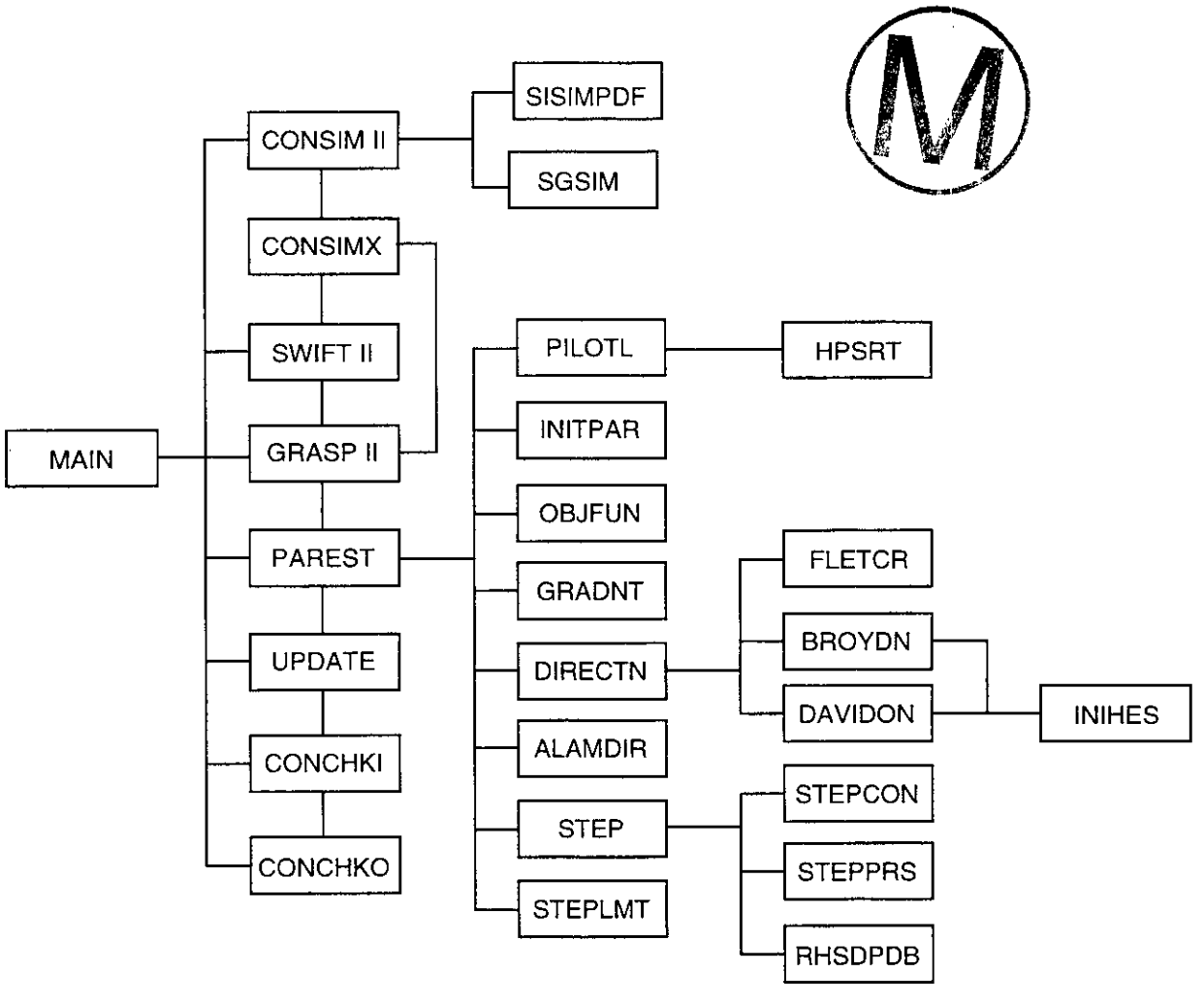

Figure TFIELD-20. GRASP-INV Code Organization

THIS PAGE INTENTIONALLY LEFT BLANK

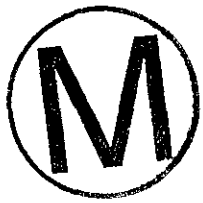

Table TFIELD-6. GRASP-INV Subroutines and Their Functions

Name of Subroutine	Purpose
MAIN	Driver Program for this code package.
SWIFT II	Simulation of pressures.
GRASP II	Sensitivity derivatives of performance measure with reference to model parameters.
SISIMPDF	Conditional simulation of categorical variables such as lithogic types.
CONSIM2	Conditional simulation of transmissivities (calls SISIMPDF and SGSIM) and averaging of simulated transmissivity values to the SWIFT II grid blocks.
CONSIMX	Modifies grid block conductivity values after a pilot point is added to the observed data set and sends this information to SWIFT II.
SGSIM	Conditional simulation of continuous variables such as transmissivities.
PAREST	Assigns pilot-point transmissivities by optimization.
PILOTL	Selects the pilot-point locations based on sensitivity analysis.
INITPAR	Initializes pilot-point transmissivities and their covariance matrix for the first iteration in calibrations.
READ3	Reads input related to pilot-point transmissivity optimization.
OBJFUN	Compute weighted least squares objective function.
GRADNT	Computes gradients of objective function to pilot-point transmissivities.
DIRECTN	Computes directions in search algorithm.
STEP	Computes step length in search algorithm.
UPDATE	Updates the pilot-point transmissivities at the end of an iteration.
HPSRT	Sorts absolute gradients in descending order.
BROYDN	Computes direction per Broyden algorithm.
FLETCR	Computes direction per Fletcher-Reeves (conjugate gradients) algorithm.
INIHES	Computes initial approximate inverse Hessian matrix.
STEPCON	Computes transmissivities-dependent constant in step-length formula.
STEPPRS	Computes pressure-dependent expressions in step-length formula.
ALAMDIR	Computes expressions involving Kriging weights and directions (to be used in solving sensitivity of pressure to step length).
RHSDPDB	Computes right-hand column vector for solving the equation for sensitivity of pressure to step length.
STEPLMT	Implements constraints on step length after optimization.
CONVCKI	Checks convergence of inner iterations.
CONVCKO	Checks convergence of outer iterations.

TFIELD.4.1.2 Model Grid-Block Elevations and Formation-Fluid Densities

The elevation data and fluid-density data presented in Section 2 were used to estimate the Culebra elevation above mean sea level and the formation fluid density for each grid block in the model. These parameters were assigned to each grid block in order to include their effect into the groundwater velocities across the model domain. Kriging was used to obtain estimates for the elevation and fluid-densities at each grid block. Prior to variogram analysis, a trend was removed from the elevation data to obtain "intrinsic" residuals. This action implies that the raw variogram contained a sill. While the fluid-density data does reveal a slight trend, it was possible to model this trend directly using a directional variogram. Figures TFIELD-23a and TFIELD-23b illustrate the variograms employed for the elevation-data residuals and fluid-density data, respectively. The trend surface removed from the elevation data was $Elev(x,y) = 974.4 + 5.686(x) - 5.250(y)$. An isotropic Gaussian variogram with a sill of 688 m, a range of 10 kilometers, and a nugget of 20 m was determined to adequately represent the elevation raw variogram. The variogram for the fluid-density data was oriented at 128°. An exponential variogram with a sill of 9.6, a range of 6 kilometers, and a nugget of 6.4 was chosen for the density data. The theoretical variogram used for the elevation data fit the elevation data raw variogram well. The fit of the theoretical model used for the density data to the density raw variogram could be improved. More adjustments to the raw variogram could have been made to smooth out its fluctuations. However, the general fit to the data was considered acceptable.

Using the variograms in Figures TFIELD-23a and TFIELD-23b (as well as the elevation trend surface), the kriged estimates of elevation and formation fluid density at each grid block were obtained. These kriged surfaces are illustrated in Figures TFIELD-24 and TFIELD-25 for the Culebra elevation and formation-fluid density, respectively. The elevation dips to the southeast similar to the elevation surface illustrated in Figure TFIELD-3. The formation fluid density kriged surface increases from west to east. These two parameters were specified for each grid block in the simulation domain and held constant over the simulation period of the model.

TFIELD.4.1.3 Model Boundary Conditions

To estimate the boundary conditions for the boundary grid blocks, a kriging analysis was conducted. A variogram for the observed steady-state heads was obtained by removing a trend that was present in the head and analyzing the head residuals. A trend had to be removed from the head data because the head field is not stationary, which negates the possibility of variogram analysis. Linear regression of the heads was used to obtain the coefficients of the trend surface $H(x,y) = 912.409 - 0.6938x + 1.1326y + 0.0104xy$. Once the trend was removed from the observed head data, a variogram analysis on the head residuals produced the variogram illustrated in Figure TFIELD-26. This variogram was used to estimate the boundary head residuals, which were then added to the trend surface to obtain the boundary heads. As Figure TFIELD-26 illustrates, the raw variogram for the residuals continues to increase at distances longer than 2 kilometers, an indication that the trend did not completely

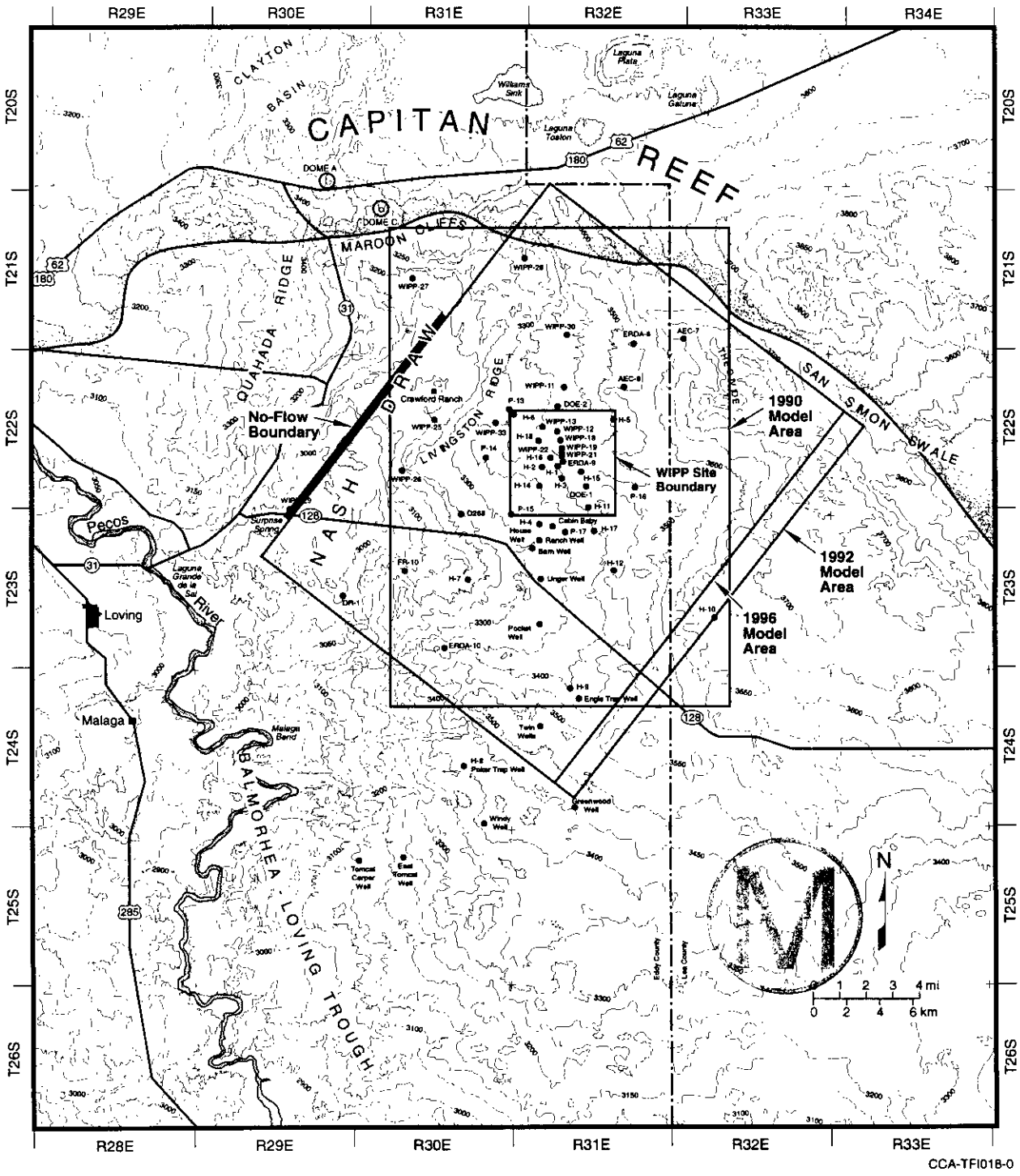

Figure TFIELD-21. 1996 Culebra Model Boundaries over the WIPP Site Area

1 **THIS PAGE INTENTIONALLY LEFT BLANK**

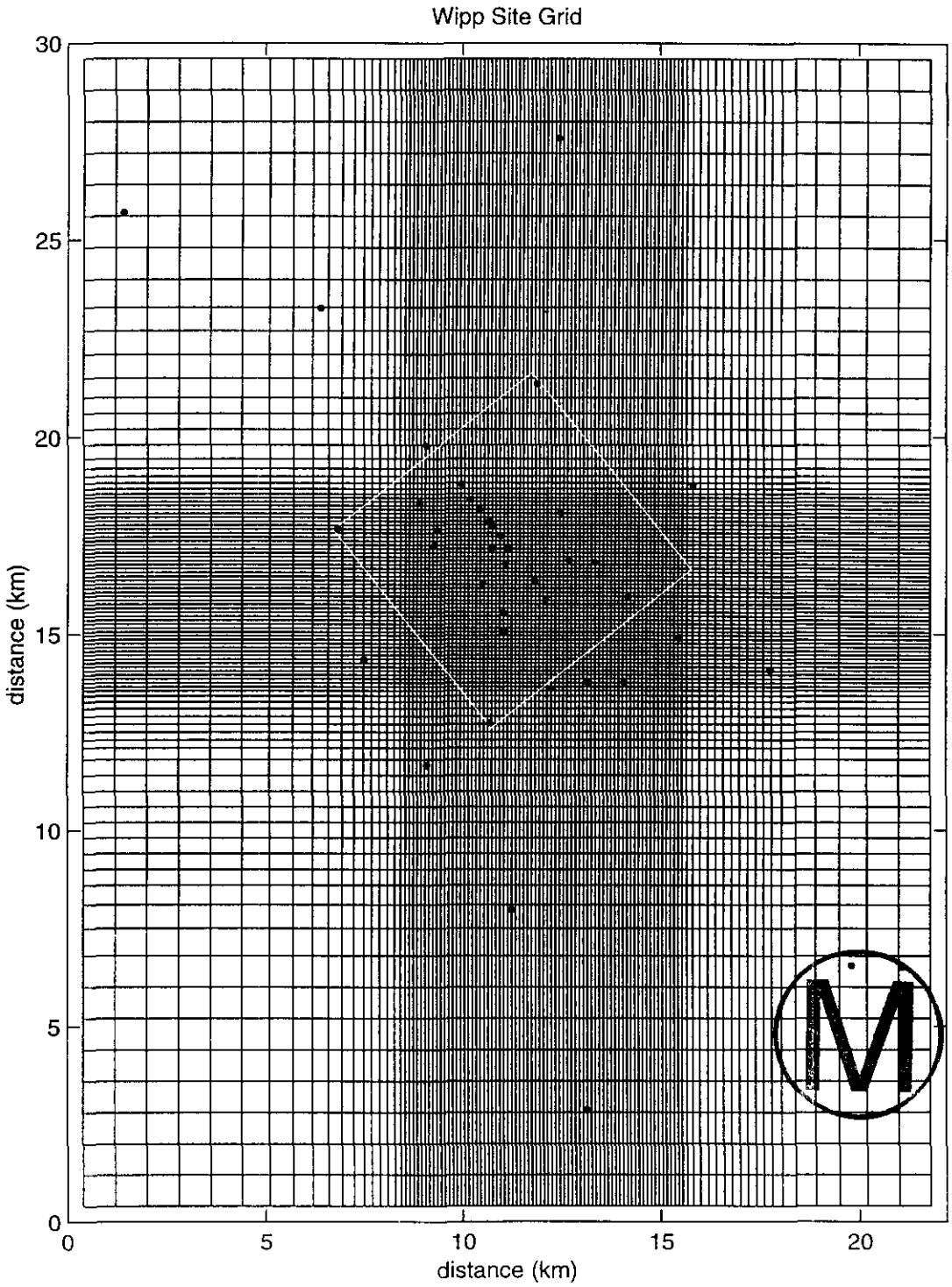

Figure TFIELD-22. 1996 Culebra Model Finite-Difference Grid

THIS PAGE INTENTIONALLY LEFT BLANK

Table TFIELD-7. Model Grid Block Dimensions

NX; 108 NY; 100

DX (SW to NE):

800. 800. 800. 800. 800. 800. 600. 600. 400. 400.
300. 300. 200. 200. 200. 200. 150. 150. 100. 100.
100. 100. 100. 100. 100. 100. 100. 100. 100. 100.
100. 100. 100. 100. 100. 100. 100. 100. 100. 100.
100. 100. 100. 100. 100. 100. 100. 100. 100. 100.
100. 100. 100. 100. 100. 100. 100. 100. 100. 100.
100. 100. 100. 100. 100. 100. 100. 100. 100. 100.
100. 100. 100. 100. 100. 100. 100. 100. 100. 100.
100. 100. 100. 100. 100. 100. 100. 100. 100. 150.
150. 200. 200. 200. 200. 200. 200. 200. 200. 200.
200. 300. 400. 600. 600. 800. 800. 800.

DY (SE to NW):

800. 800. 800. 800. 800. 800. 800. 800. 800. 600.
600. 400. 400. 400. 400. 400. 400. 400. 400. 400.
200. 200. 200. 200. 200. 200. 150. 150. 100. 100.
100. 100. 100. 100. 100. 100. 100. 100. 100. 100.
100. 100. 100. 100. 100. 100. 100. 100. 100. 100.
100. 100. 100. 100. 100. 100. 100. 100. 100. 100.
100. 100. 100. 100. 100. 100. 100. 100. 100. 100.
100. 100. 100. 100. 100. 100. 100. 100. 100. 150.
150. 200. 200. 300. 400. 400. 400. 400. 600. 600.
600. 600. 800. 800. 800. 800. 800. 800. 800. 800.

render the residuals intrinsic. However, an isotropic Gaussian variogram with a range of 2 kilometers, a sill of 50 square meters, and a nugget of 2.66 square meters fit the data occurring within 2 kilometers adequately. Kriging the head residuals at each of the boundary grid blocks and subsequently adding the trend surface back to the residuals produced the heads that were assigned to the boundaries. Table TFIELD-8 lists the prescribed-pressure boundaries (expressed as heads in meters) that were estimated at each grid block along the southeastern, southwestern, northeastern, and northwestern boundaries (Figure TFIELD-22). One section of the northwestern boundary was considered a no-flow boundary due to the groundwater divide along Nash Draw.

The Culebra is considered confined above and below by low-permeability beds of anhydrite, halite, and siltstone. Vertical flux is not considered in the model because (1) the existence of these low-permeability anhydrites indicates that flow would be confined and (2) any leakage into the Culebra would have a negligible impact upon the estimation of the transmissivity fields (that is, the large drawdowns associated with the transient tests "swamp" any effect the leakage would have upon the heads). Therefore, the conceptual model used in this study assumes a two-dimensional flow system.

TFIELD.4.1.4 Model Initial Kriged-Transmissivity Field and Its Uncertainty

A histogram of the transmissivity data listed in Table TFIELD-2 is presented in Figure TFIELD-27. The transmissivities range over five orders of magnitude excluding the outlier transmissivity value at P-18 (-10.1 $\log_{10}$ meters squared per second). The histogram illustrates an interesting aspect of the Culebra transmissivity values, namely the transmissivity distribution appears approximately bi-modal. This aspect is due to the difference between the boreholes located in areas where the transmissivities have been increased and those located in areas where the Culebra has been left intact. As mentioned in Chapter 2.0 of the main report, the transmissivities generally increase from east to west where the halite removal is greatest.

A variogram analysis was conducted for the transmissivity data to determine the input parameters needed for the CONSIM II code (that is, the sill, range, and nugget). Given the approximate bi-modal nature of the transmissivity data, separate variograms were constructed for the transmissivities above and below the median transmissivity value of -5.9 $\log_{10}$ m^2/s. The median value was chosen as the cutoff between the high and low values because (1) the histogram appears to support this value as the cutoff and (2) boreholes that have exhibited dual-porosity behavior fell into the high (that is, increased) transmissivity category using this cutoff. Prior to conducting a variogram analysis, the transmissivity data had to be transformed into a standard normal distribution with a mean of 0.0 and a variance of 1.0. The high transmissivity and low transmissivity categories were transformed separately (see Equation 3 of Section TFIELD.3.1.1).

Figures TFIELD-28a and TFIELD-28b illustrate the normal-score variograms for the high transmissivities and the low transmissivities, respectively. The most noticeable difference between the two variograms is their respective correlation lengths. The spherical variogram fitted to the high transmissivity normal scores has a range of 5.9 kilometers, a nugget of 0.05, and a sill of 0.95. The spherical variogram fitted to the low transmissivity normal scores has a range of 2.1 kilometers, a nugget of 0.11, and a sill of 0.89. Thus, the correlation length associated with the high transmissivity normal scores is almost three times longer that the correlation length associated with the low transmissivity normal scores.

Given this difference in the variograms shown in Figures TFIELD-28a and TFIELD-28b, an indicator variogram analysis was conducted on the categorical variables that were assigned to the WIPP boreholes as follows. If a borehole's transmissivity value fell into the high transmissivity category (that is, above the median value), it was assigned a categorical value of 1. If a borehole's transmissivity value fell into the low transmissivity category, it was assigned a categorical value of 2. An indicator variogram on the categorical values assigned to each borehole revealed the variogram illustrated in Figure TFIELD-29. A spherical variogram with a range of 2 kilometers and a sill of 0.25 fitted the categorical raw variogram well. It should be remembered that the $\gamma(h)$ value on the y-axis of Figure TFIELD-29 is equal to $(p - p^2)$, where p represents the probability of changing from one category to the next.

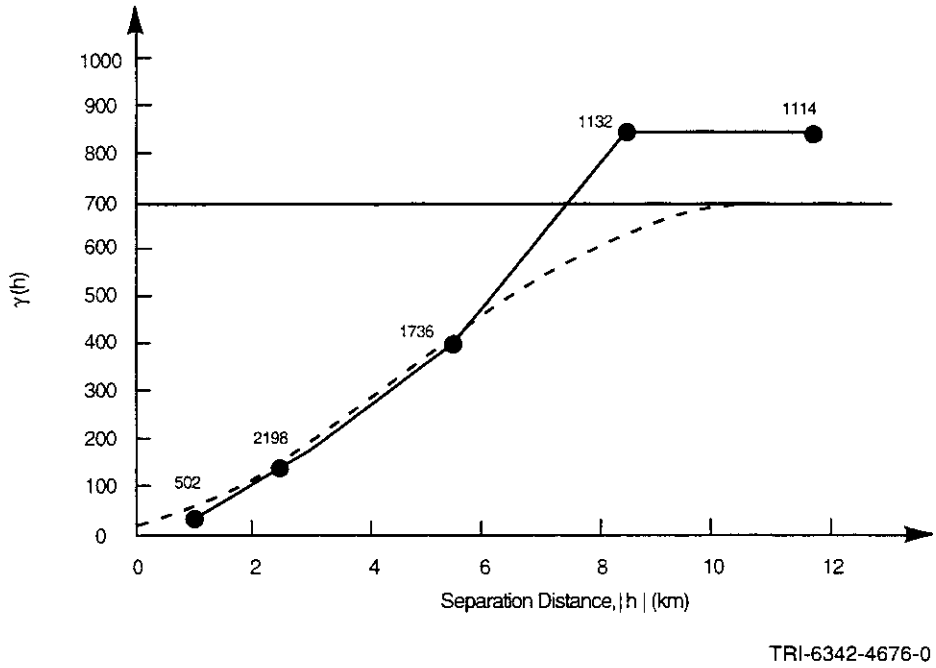

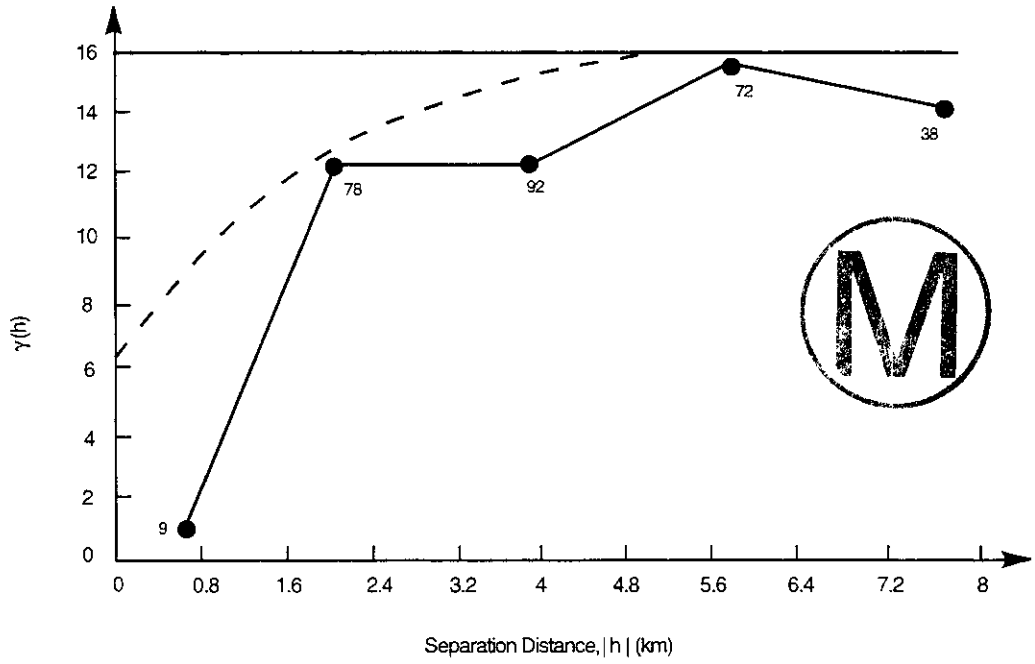

Figure TFIELD-23. Variograms for the (a) Culebra Elevation Data and (b) Formation-Fluid Density Data

1 **THIS PAGE INTENTIONALLY LEFT BLANK**

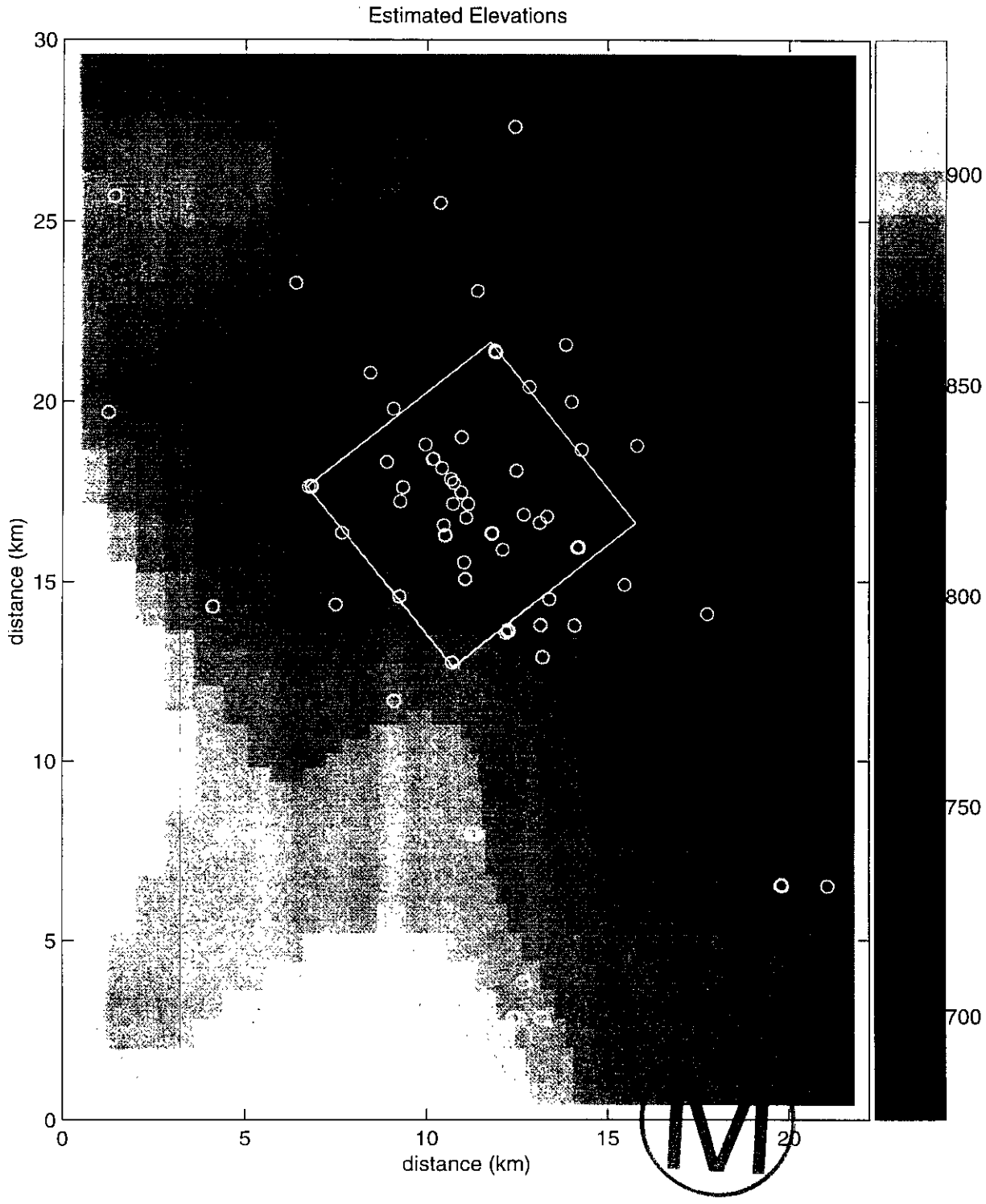

Figure TFIELD-24. Kriged Estimates of the Elevation of the Model Grid Blocks

THIS PAGE INTENTIONALLY LEFT BLANK

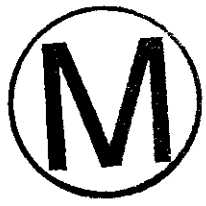

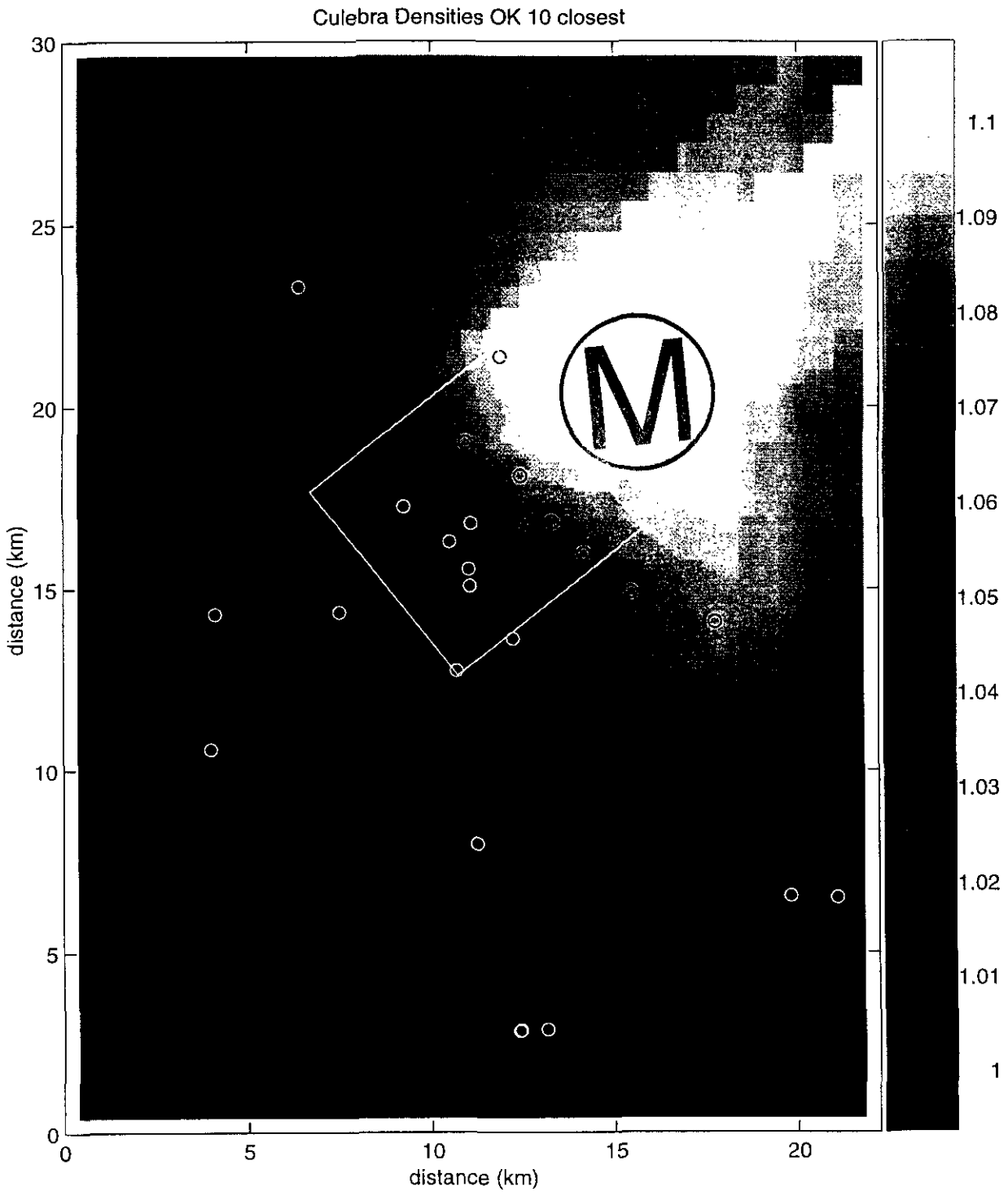

Figure TFIELD-25. Kriged Estimates of the Formation-Fluid Densities of the Model Grid Blocks

1 THIS PAGE INTENTIONALLY LEFT BLANK

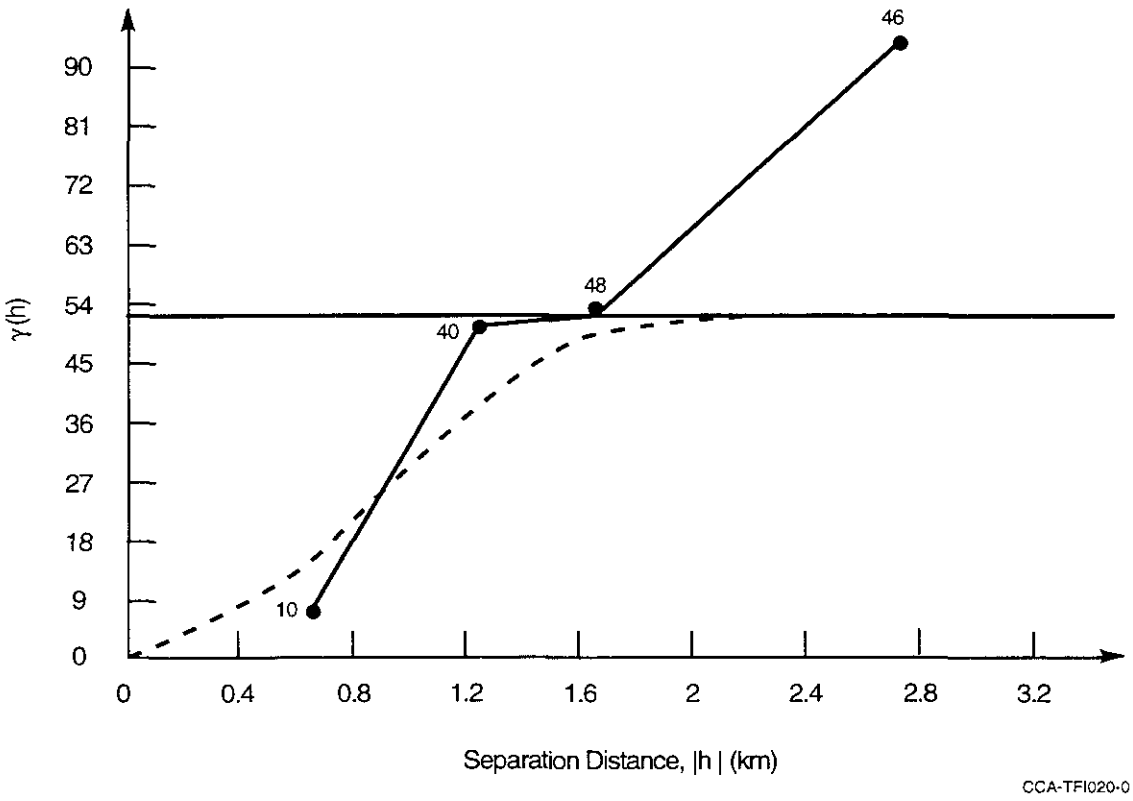

Figure TFIELD-26. Variogram of the Culebra Freshwater Head Residuals

1 THIS PAGE INTENTIONALLY LEFT BLANK

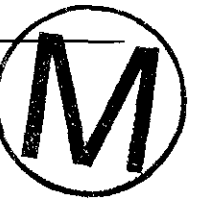

Table TFIELD-8. Prescribed Boundary Conditions

Southwestern Model Boundary

Grid Block Center X (kilometer)	Grid Block Center Y (kilometer)	Boundary Head (meter)	Grid Block Center X (kilometer)	Grid Block Center Y (kilometer)	Boundary Head (meter)
0.000	0.400	912.86	0.000	15.750	930.26
0.000	1.200	913.76	0.000	15.850	930.37
0.000	2.000	914.67	0.000	15.950	930.49
0.000	2.800	915.58	0.000	16.050	930.60
0.000	3.600	916.48	0.000	16.150	930.71
0.000	4.400	917.39	0.000	16.250	930.82
0.000	5.200	918.29	0.000	16.350	930.94
0.000	6.000	919.20	0.000	16.450	931.05
0.000	6.800	920.10	0.000	16.550	931.16
0.000	7.500	920.89	0.000	16.650	931.28
0.000	8.100	921.56	0.000	16.750	931.39
0.000	8.600	922.12	0.000	16.850	931.50
0.000	9.000	922.56	0.000	16.950	931.62
0.000	9.400	923.01	0.000	17.050	931.73
0.000	9.800	923.45	0.000	17.150	931.84
0.000	10.200	923.90	0.000	17.250	931.96
0.000	10.600	924.35	0.000	17.350	932.07
0.000	11.000	924.81	0.000	17.450	932.19
0.000	11.400	925.27	0.000	17.550	932.31
0.000	11.800	925.73	0.000	17.650	932.42
0.000	12.100	926.08	0.000	17.750	932.54
0.000	12.300	926.32	0.000	17.850	932.66
0.000	12.500	926.55	0.000	17.950	932.77
0.000	12.700	926.79	0.000	18.050	932.89
0.000	12.900	927.02	0.000	18.150	933.01
0.000	13.100	927.25	0.000	18.250	933.13
0.000	13.275	927.45	0.000	18.350	933.24
0.000	13.425	927.63	0.000	18.450	933.36
0.000	13.550	927.77	0.000	18.550	933.48
0.000	13.650	927.89	0.000	18.675	933.63
0.000	13.750	928.00	0.000	18.825	933.81
0.000	13.850	928.12	0.000	19.000	934.02
0.000	13.950	928.23	0.000	19.200	934.25
0.000	14.050	928.35	0.000	19.450	934.55
0.000	14.150	928.46	0.000	19.800	934.96
0.000	14.250	928.57	0.000	20.200	935.42
0.000	14.350	928.69	0.000	20.600	935.86
0.000	14.450	928.80	0.000	21.000	936.29
0.000	14.550	928.91	0.000	21.500	936.82
0.000	14.650	929.03	0.000	22.100	937.41
0.000	14.750	929.14	0.000	22.700	937.93
0.000	14.850	929.25	0.000	23.300	938.33
0.000	14.950	929.36	0.000	24.000	938.62
0.000	15.050	929.48	0.000	24.800	938.87
0.000	15.150	929.59	0.000	25.600	939.43
0.000	15.250	929.70	0.000	26.400	940.57
0.000	15.350	929.81	0.000	27.200	942.10
0.000	15.450	929.93	0.000	28.000	943.60
0.000	15.550	930.04	0.000	28.800	944.85
0.000	15.650	930.15	0.000	29.600	945.89

Table TFIELD-8. Prescribed Boundary Conditions (Continued)

Southeastern Model Boundary

Grid Block Center X (kilometer)	Grid Block Center Y (kilometer)	Boundary Head (meter)	Grid Block Center X (kilometer)	Grid Block Center Y (kilometer)	Boundary Head (meter)
22.200	0.400	897.55	22.200	15.750	919.81
22.200	1.200	898.64	22.200	15.850	919.92
22.200	2.000	899.73	22.200	15.950	920.02
22.200	2.800	900.81	22.200	16.050	920.12
22.200	3.600	901.88	22.200	16.150	920.22
22.200	4.400	902.93	22.200	16.250	920.31
22.200	5.200	903.94	22.200	16.350	920.39
22.200	6.000	904.96	22.200	16.450	920.47
22.200	6.800	906.04	22.200	16.550	920.55
22.200	7.500	907.04	22.200	16.650	920.63
22.200	8.100	907.92	22.200	16.750	920.71
22.200	8.600	908.64	22.200	16.850	920.79
22.200	9.000	909.22	22.200	16.950	920.86
22.200	9.400	909.78	22.200	17.050	920.94
22.200	9.800	910.34	22.200	17.150	921.02
22.200	10.200	910.90	22.200	17.250	921.10
22.200	10.600	911.45	22.200	17.350	921.18
22.200	11.000	912.00	22.200	17.450	921.27
22.200	11.400	912.56	22.200	17.550	921.36
22.200	11.800	913.13	22.200	17.650	921.45
22.200	12.100	913.58	22.200	17.750	921.54
22.200	12.300	913.88	22.200	17.850	921.64
22.200	12.500	914.20	22.200	17.950	921.74
22.200	12.700	914.52	22.200	18.050	921.84
22.200	12.900	914.86	22.200	18.150	921.95
22.200	13.100	915.21	22.200	18.250	922.06
22.200	13.275	915.53	22.200	18.350	922.17
22.200	13.425	915.80	22.200	18.450	922.28
22.200	13.550	916.04	22.200	18.550	922.40
22.200	13.650	916.23	22.200	18.675	922.55
22.200	13.750	916.43	22.200	18.825	922.73
22.200	13.850	916.62	22.200	19.000	922.95
22.200	13.950	916.82	22.200	19.200	923.21
22.200	14.050	917.01	22.200	19.450	923.53
22.200	14.150	917.21	22.200	19.800	924.00
22.200	14.250	917.40	22.200	20.200	924.54
22.200	14.350	917.60	22.200	20.600	925.08
22.200	14.450	917.79	22.200	21.000	925.62
22.200	14.550	917.98	22.200	21.500	926.31
22.200	14.650	918.16	22.200	22.100	927.12
22.200	14.750	918.34	22.200	22.700	927.94
22.200	14.850	918.52	22.200	23.300	928.76
22.200	14.950	918.69	22.200	24.000	929.71
22.200	15.050	918.85	22.200	24.800	930.80
22.200	15.150	919.01	22.200	25.600	931.89
22.200	15.250	919.16	22.200	26.400	932.98
22.200	15.350	919.30	22.200	27.200	934.07
22.200	15.450	919.44	22.200	28.000	935.16
22.200	15.550	919.57	22.200	28.800	936.25
22.200	15.650	919.69	22.200	29.600	937.35

Table TFIELD-8. Prescribed Boundary Conditions (Continued)

Northwestern Model Boundary

Grid Block Center X (kilometer)	Grid Block Center Y (kilometer)	Boundary Head (meter)	Grid Block Center X (kilometer)	Grid Block Center Y (kilometer)	Boundary Head (meter)
0.400	0.000	912.13	12.150	0.000	904.26
1.200	0.000	911.57	12.250	0.000	904.20
2.000	0.000	911.02	12.350	0.000	904.14
2.800	0.000	910.46	12.450	0.000	904.09
3.600	0.000	909.91	12.550	0.000	904.03
4.400	0.000	909.35	12.650	0.000	903.97
5.100	0.000	908.87	12.750	0.000	903.90
5.700	0.000	908.45	12.850	0.000	903.84
6.200	0.000	908.10	12.950	0.000	903.78
6.600	0.000	907.83	13.050	0.000	903.71
6.950	0.000	907.58	13.150	0.000	903.64
7.250	0.000	907.37	13.250	0.000	903.57
7.500	0.000	907.20	13.350	0.000	903.50
7.700	0.000	907.06	13.450	0.000	903.42
7.900	0.000	906.92	13.550	0.000	903.35
8.100	0.000	906.79	13.650	0.000	903.27
8.275	0.000	906.66	13.750	0.000	903.19
8.425	0.000	906.56	13.850	0.000	903.11
8.550	0.000	906.47	13.950	0.000	903.03
8.650	0.000	906.41	14.050	0.000	902.95
8.750	0.000	906.34	14.150	0.000	902.87
8.850	0.000	906.27	14.250	0.000	902.78
8.950	0.000	906.20	14.350	0.000	902.70
9.050	0.000	906.13	14.450	0.000	902.61
9.150	0.000	906.06	14.550	0.000	902.53
9.250	0.000	905.99	14.650	0.000	902.44
9.350	0.000	905.93	14.750	0.000	902.36
9.450	0.000	905.86	14.850	0.000	902.27
9.550	0.000	905.79	14.950	0.000	902.19
9.650	0.000	905.73	15.050	0.000	902.11
9.750	0.000	905.66	15.150	0.000	902.02
9.850	0.000	905.59	15.250	0.000	901.94
9.950	0.000	905.53	15.350	0.000	901.86
10.050	0.000	905.46	15.450	0.000	901.78
10.150	0.000	905.40	15.550	0.000	901.70
10.250	0.000	905.34	15.675	0.000	901.60
10.350	0.000	905.27	15.825	0.000	901.48
10.450	0.000	905.21	16.000	0.000	901.35
10.550	0.000	905.15	16.200	0.000	901.20
10.650	0.000	905.09	16.400	0.000	901.05
10.750	0.000	905.03	16.600	0.000	900.91
10.850	0.000	904.97	16.800	0.000	900.76
10.950	0.000	904.92	17.000	0.000	900.62
11.050	0.000	904.86	17.200	0.000	900.48
11.150	0.000	904.80	17.400	0.000	900.34
11.250	0.000	904.75	17.600	0.000	900.20
11.350	0.000	904.69	17.800	0.000	900.06
11.450	0.000	904.64	18.050	0.000	899.88
11.550	0.000	904.58	18.400	0.000	899.64
11.650	0.000	904.53	18.900	0.000	899.29
11.750	0.000	904.47	19.500	0.000	898.88
11.850	0.000	904.42	20.200	0.000	898.39
11.950	0.000	904.37	21.000	0.000	897.83
12.050	0.000	904.31	21.800	0.000	897.28

Table TFIELD-8. Prescribed Boundary Conditions (Continued)

Northeastern Model Boundary

Grid Block Center X (kilometer)	Grid Block Center Y (kilometer)	Boundary Head (meter)	Grid Block Center X (kilometer)	Grid Block Center Y (kilometer)	Boundary Head (meter)
0.400	30.000	946.20	12.150	30.000	940.32
1.200	30.000	945.89	12.250	30.000	940.27
2.000	30.000	945.59	12.350	30.000	940.22
2.800	30.000	945.29	12.450	30.000	940.18
3.600	30.000	944.99	12.550	30.000	940.14
4.400	30.000	944.69	12.650	30.000	940.12
5.100	30.000	944.43	12.750	30.000	940.10
5.700	30.000	944.20	12.850	30.000	940.09
6.200	30.000	944.01	12.950	30.000	940.08
6.600	30.000	943.86	13.050	30.000	940.08
6.950	30.000	943.72	13.150	30.000	940.08
7.250	30.000	943.61	13.250	30.000	940.09
7.500	30.000	943.51	13.350	30.000	940.11
7.700	30.000	943.43	13.450	30.000	940.12
7.900	30.000	943.35	13.550	30.000	940.14
8.100	30.000	943.27	13.650	30.000	940.16
8.275	30.000	943.20	13.750	30.000	940.19
8.425	30.000	943.13	13.850	30.000	940.21
8.550	30.000	943.08	13.950	30.000	940.23
8.650	30.000	943.03	14.050	30.000	940.26
8.750	30.000	942.99	14.150	30.000	940.28
8.850	30.000	942.94	14.250	30.000	940.30
8.950	30.000	942.89	14.350	30.000	940.32
9.050	30.000	942.84	14.450	30.000	940.33
9.150	30.000	942.78	14.550	30.000	940.35
9.250	30.000	942.73	14.650	30.000	940.36
9.350	30.000	942.67	14.750	30.000	940.36
9.450	30.000	942.61	14.850	30.000	940.37
9.550	30.000	942.55	14.950	30.000	940.37
9.650	30.000	942.48	15.050	30.000	940.36
9.750	30.000	942.41	15.150	30.000	940.36
9.850	30.000	942.34	15.250	30.000	940.35
9.950	30.000	942.27	15.350	30.000	940.34
10.050	30.000	942.19	15.450	30.000	940.32
10.150	30.000	942.11	15.550	30.000	940.31
10.250	30.000	942.02	15.675	30.000	940.28
10.350	30.000	941.93	15.825	30.000	940.25
10.450	30.000	941.84	16.000	30.000	940.20
10.550	30.000	941.75	16.200	30.000	940.14
10.650	30.000	941.66	16.400	30.000	940.08
10.750	30.000	941.56	16.600	30.000	940.01
10.850	30.000	941.46	16.800	30.000	939.94
10.950	30.000	941.36	17.000	30.000	939.87
11.050	30.000	941.26	17.200	30.000	939.80
11.150	30.000	941.16	17.400	30.000	939.72
11.250	30.000	941.06	17.600	30.000	939.65
11.350	30.000	940.96	17.800	30.000	939.57
11.450	30.000	940.87	18.050	30.000	939.48
11.550	30.000	940.78	18.400	30.000	939.34
11.650	30.000	940.69	18.900	30.000	939.15
11.750	30.000	940.60	19.500	30.000	938.92
11.850	30.000	940.52	20.200	30.000	938.66
11.950	30.000	940.45	21.000	30.000	938.35
12.050	30.000	940.38	21.800	30.000	938.04

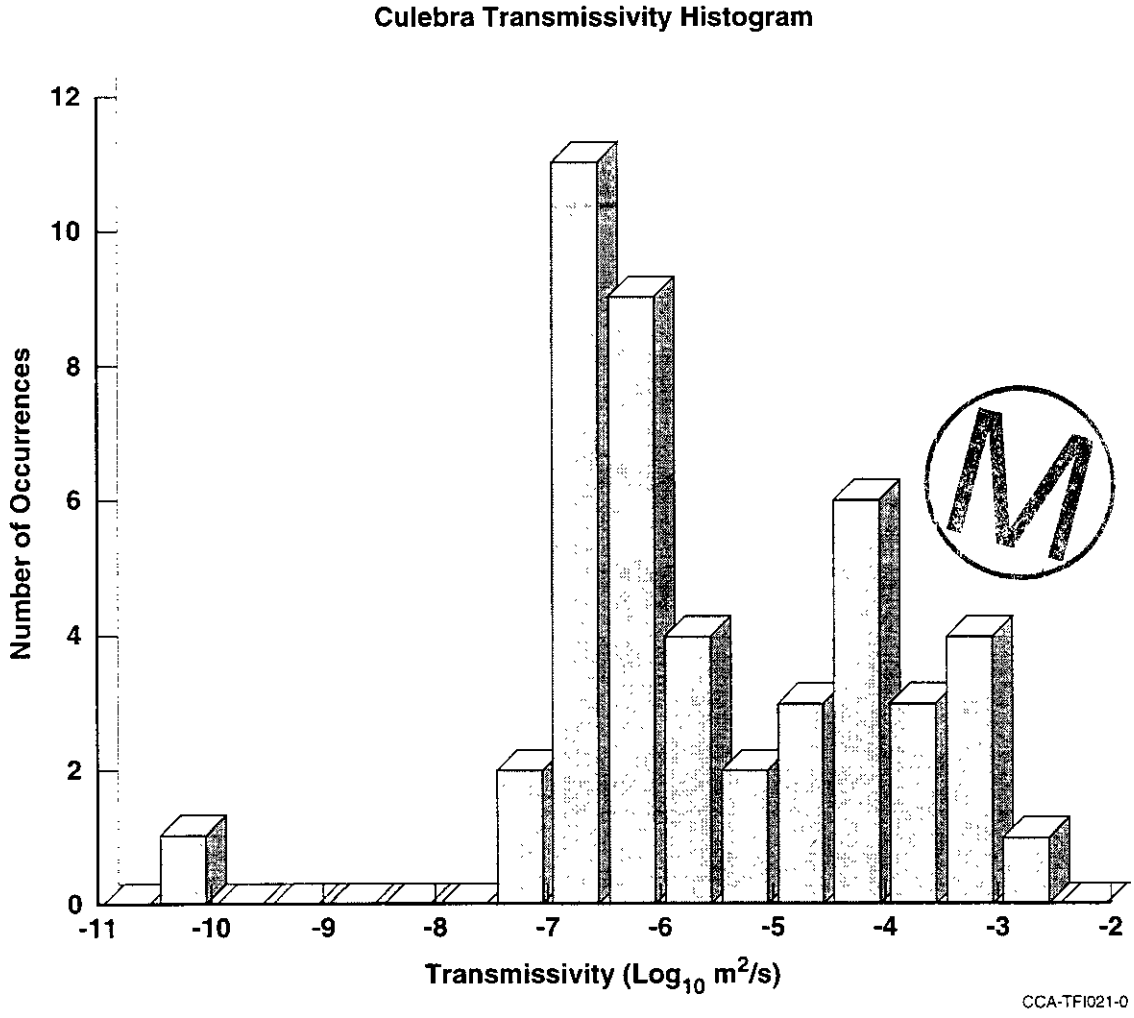

Figure TFIELD-27. Histogram of the Culebra Transmissivity Data

THIS PAGE INTENTIONALLY LEFT BLANK

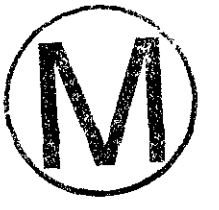

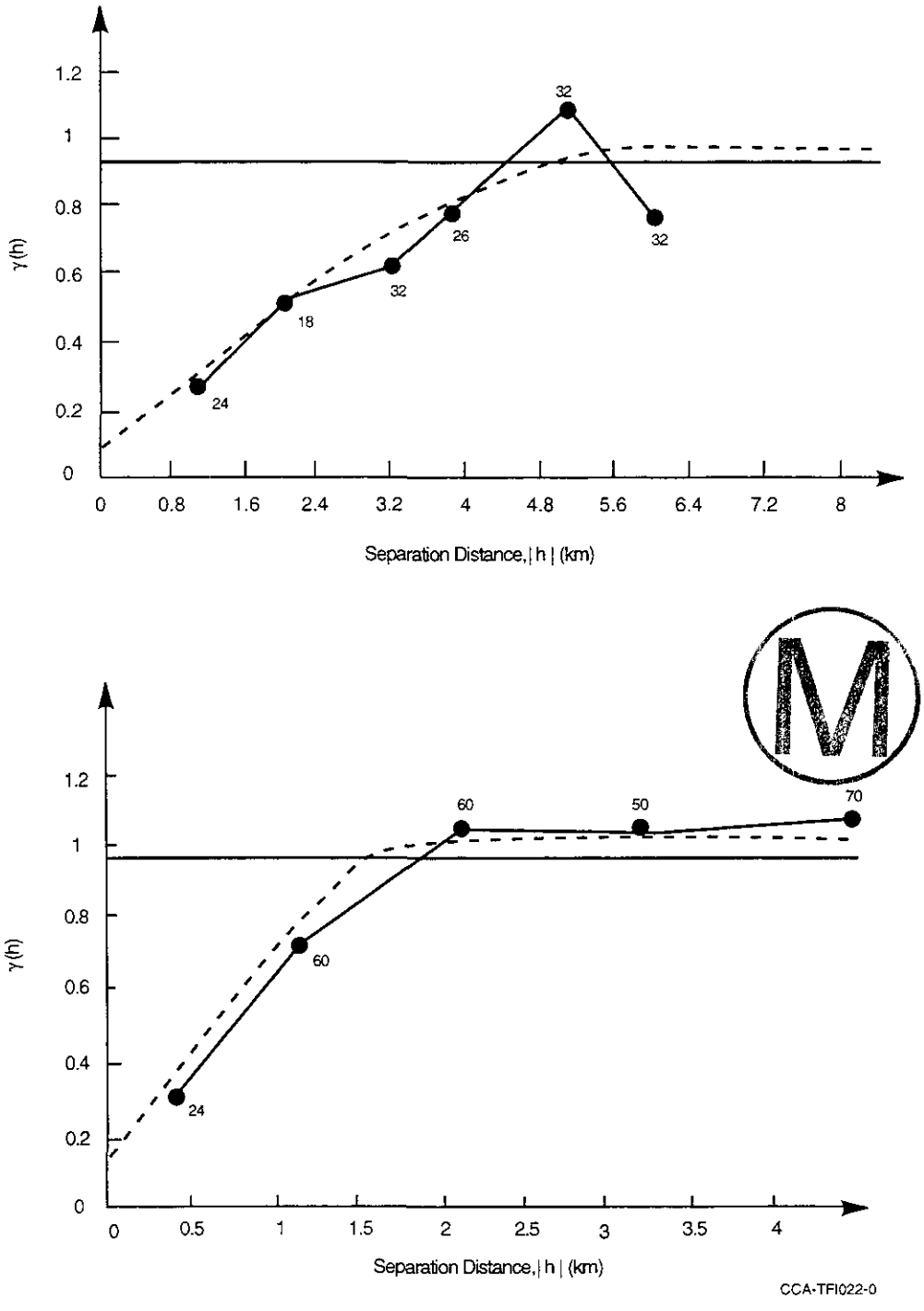

Figure TFIELD-28. Variograms for the Normal Scores of the Culebra Transmissivities that are (a) Higher Than and (b) Lower Than the Median Transmissivity

1 THIS PAGE INTENTIONALLY LEFT BLANK

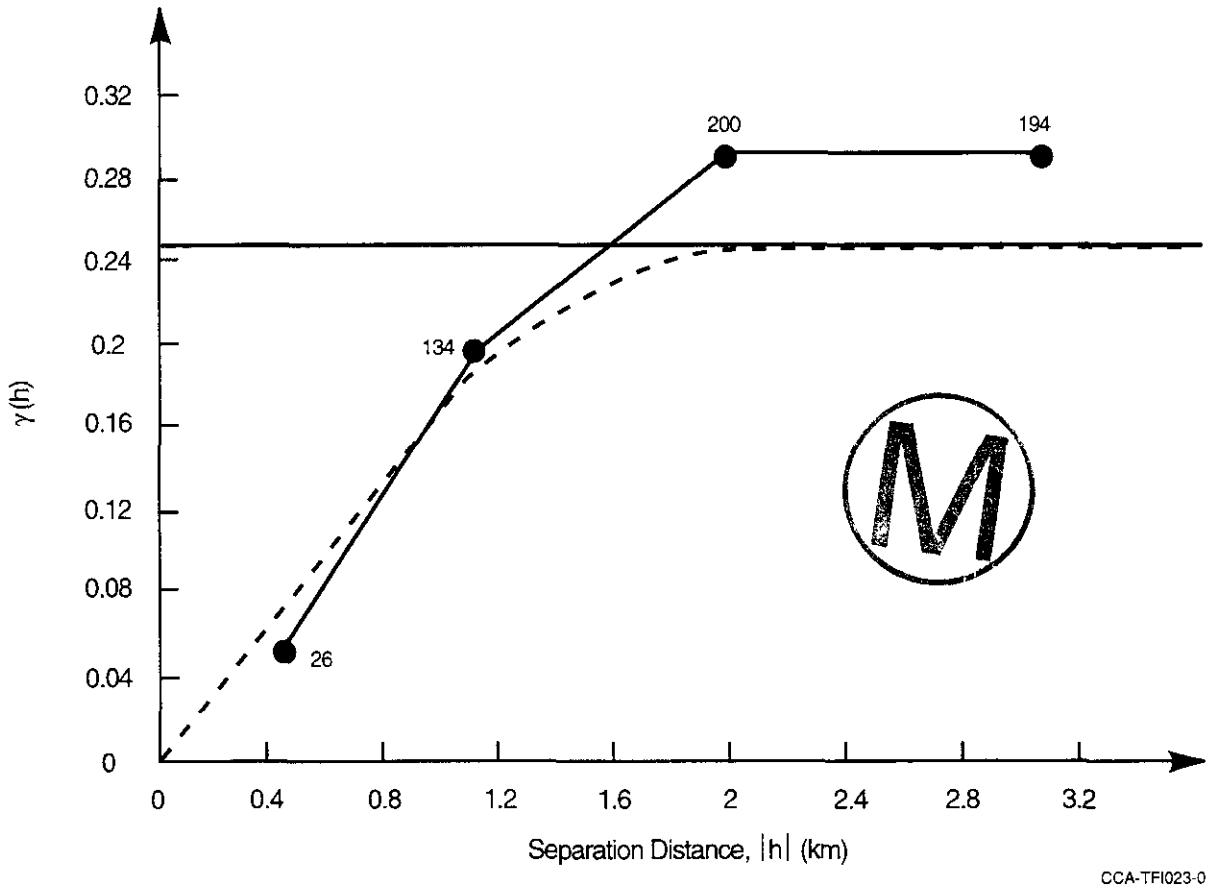

Figure TFIELD-29. Indicator Variogram for the Culebra High Transmissivity and Low Transmissivity Categories

THIS PAGE INTENTIONALLY LEFT BLANK

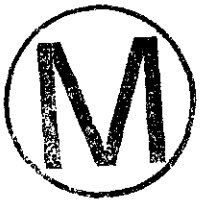

Because one of the conclusions presented in LaVenue and RamaRao (1992) stated that the location of the boundary between the high and low transmissivities in the area between the H-1 and H-11 boreholes had an important effect upon the groundwater travel time to the WIPP site boundary, it was decided to geostatistically simulate the high transmissivities separately from the low transmissivities. This step was accomplished by using the indicator variogram illustrated in Figure TFIELD-29 to determine the category of the model grid blocks and subsequently assigning a transmissivity value to the grid block by employing the appropriate variogram, that is, either Figure TFIELD-28a for category 1 grid blocks or Figure TFIELD-28b for category 2 grid blocks.

To develop the initial transmissivity values for the model grid blocks in each realization, a finer grid was superimposed upon the grid illustrated in Figure TFIELD-22. This finer grid, referred to as the geostatistical simulation grid, was evenly spaced in the x and y directions with a spacing of 100 meters. Thus, there were 299 nodes in the y direction and 219 in the x direction. All the conditional simulations were conducted on this grid and scaled up to the groundwater model's finite-difference grid (Figure TFIELD-22) using the electric analog upscaling procedure described in Section TFIELD.3.1.7.1. The upscaled transmissivities were then used in the flow model to determine the calculated heads over the model domain and, subsequently, the measured heads were calibrated.

TFIELD.4.1.5 Transient Events Simulated in Model

As in the 1992 Culebra model, the steady-state heads were calibrated first. Once steady-state calibration was obtained, transient calibration to the drawdowns resulting from the construction of the shafts and the regional scale pumping tests began. The transient events used in the model to calibrate the transmissivity fields are listed in Table TFIELD-9. These events are essentially the same as those used in the 1992 Culebra model; however, the pumping events that occurred in 1995 and 1996, for example, pumping at H-19, H-11, and WQSP-2, were added to the simulated events. It should be noted that the drawdowns associated with the H-19 tracer test were not included during transient calibration but were calculated by the model. This calculation provided a test against which the model's calibrated transmissivity field could be verified. The time steps used in the model are listed in Table TFIELD-10. The results of the steady-state and transient calibration for 100 conditionally simulated transmissivity fields are described in the following section.

TFIELD.4.2 Discussion of the Calibrated Conditionally Simulated Transmissivity Fields

TFIELD.4.2.1 Ensemble Mean Transmissivities

As described in Section TFIELD.4.1.4, the conditionally simulated (CS) transmissivity fields were generated using sequential categorical (indicator) simulation followed by sequential Gaussian simulation. The observed transmissivity data were divided into two categories (high transmissivity and low transmissivity) and used to obtain the categorical and continuous variable (that is, transmissivity) values for the model grid blocks. As previously mentioned,

Table TFIELD-9. Transient Events Simulated in the 1996 Culebra Model

Date	Pressure or Pumping/Leakage Rate	Location and Description
1 1 1981		START TRANSIENT SIMULATION INITIATION DATE
7 8 1981	7.0E+5 Pa	700 KPA AT CONSTRUCTION AND SALT HANDLING SHAFT (CSH) LOCATION DRILLING THROUGH THE TOP OF THE CULEBRA RADIUS OF SHAFT 1.83m
8 8 1981	3.50E+5 Pa	350 KPA AT CSH LOCATION
9 8 1981	3.15E+5 Pa	315 KPA AT CSH LOCATION
10 8 1981	2.80E+5 Pa	280 KPA AT CSH LOCATION
11 8 1981	2.45E+5 Pa	245 KPA AT CSH LOCATION
12 8 1981	2.10E+5 Pa	210 KPA AT CSH LOCATION
13 8 1981	1.75E+5 Pa	175 KPA AT CSH LOCATION
14 8 1981	1.40E+5 Pa	140 KPA AT CSH LOCATION
15 8 1981	1.013E+5 Pa	ATMOSPHERIC PRESSURE AT CSH WATER LEVEL FALLS BELOW CULEBRA AT CSH
25 10 1981	1.886E+6 Pa	BOREHOLE FILLED WITH BRINE (1.3 G/CM3) AT CSH
28 10 1981	1.950E+6 Pa	PRESSURE AT CSH LOCATION
31 10 1981	2.014E+6 Pa	PRESSURE AT CSH LOCATION
2 11 1981	2.078E+6 Pa	PRESSURE AT CSH LOCATION
5 11 1981	2.142E+6 Pa	PRESSURE AT CSH LOCATION
8 11 1981	2.206E+6 Pa	PRESSURE AT CSH LOCATION
11 11 1981	2.270E+6 Pa	PRESSURE AT CSH LOCATION
14 11 1981	2.334E+6 Pa	PRESSURE AT CSH LOCATION
17 11 1981	2.873E+6 Pa	CASING INSTALLATION. PRESSURE IN BOREHOLE FILLED AT CSH
6 12 1981	1.013E+5 Pa 0.032E-03 m^3/s	LINER ON CULEBRA AT CSH, ATM PRESSURE SET LEAKAGE TO 0.032 L/S BRINE PUMPED FROM CSH BOREHOLE

Table TFIELD-9. Transient Events Simulated in the 1996 Culebra Model (Continued)

Date	Pressure or Pumping/Leakage Rate	Location and Description
30 01 1982	1.013E+5 Pa	VENTILATION SHAFT (WHS) PENETRATES CULEBRA WITH 0.91m RADIUS
1 10 1983	0.005E-03 m^3/s	SET LEAKAGE TO 0.005 L/S AT CSH
5 10 1983	1013E+5 Pa	EXHAUST SHAFT (EXS) PENETRATES CULEBRA WITH AVERAGE RADIUS BETWEEN 0.1m AND 0.14m
10 01 1984	1.013E+5 Pa	CULEBRA REAMED AT EXS TO 0.91m RADIUS
1 02 1984	1.013E+5 Pa	CULEBRA REAMED AT WHS TO 3.27m RADIUS
5 04 1984	1.013E+5 Pa	CULEBRA LINED AT WHS, WELL BORE SKIN TIGHTENED
20 08 1984	1.013E+5 Pa	CULEBRA GROUTED AT WHS, SKIN TIGHTENED
15 10 1984	1.013E+5 Pa	EXHAUST SHAFT REAMS CULEBRA TO 2.13m RADIUS
4 12 1984	1.013E+5 Pa	EXHAUST SHAFT LINED, SKIN TIGHTENED
20 06 1985	0.129E-3 m^3/s	PUMPING AT H-3 (0.129 L/S) START H-3 STEP DRAW DOWN TEST
24 06 1985	0.250E-3 m^3/s	RESET PUMP RATE AT H-3
28 06 1985	0.300E-3 m^3/s	RESET PUMP RATE AT H-3
5 07 1985	0.321E-3 m^3/s	RESET PUMP RATE AT H-3
10 07 1985	0.0 m^3/s	PUMP OFF AT H-3 (END OF TEST)
15 07 1985	0.0120E-3 m^3/s	EXS LINED, SET LEAKAGE RATE TO 0.012 L/S
15 10 1985	0.31E-3 m^3/s	SET PUMP RATE AT H-3B2 TO 0.31 L/S
16 12 1985	0.0 m^3/s	PUMP OFF AT H-3B2, TIGHTEN SKIN AT WHS
15 07 1986	0.015E-03 m^3/s	LEAKAGE RATE AT WHS
12 01 1987	1.89E-3 m^3/s	SET PUMP RATE AT WIPP-13 (L/S)
27 01 1987	1.94E-3 m^3/s	RESET PUMP RATE AT WIPP-13 (L/S)
04 02 1987	1.99E-3 m^3/s	RESET PUMP RATE AT WIPP-13
11 02 1987	1.97E-3 m^3/s	RESET PUMP RATE AT WIPP-13

Table TFIELD-9. Transient Events Simulated in the 1996 Culebra Model (Continued)

Date	Pressure or Pumping/Leakage Rate	Location and Description
17 02 1987	0.0 m^3/s	PUMPING OFF AT WIPP-13
1 06 1987	0.00 m^3/s	CSH GROUTED, LEAKAGE TO 0.0 L/S AT CSH
1 07 1987	0.0125E-3 m^3/s	EXS LINED, LEAKAGE 0.0125 L/S
1 11 1987	0.00 m^3/s	WHS GROUTED- REDUCED LEAKAGE
1 01 1988	1.310E+6 Pa	AIR-INTAKE SHAFT (AIS) PENETRATES CULEBRA WITH 0.12m RADIUS
8 01 1988	1.690E+6 Pa	PRESSURE AT AIS SHAFT IN CULEBRA
2 02 1988	1.510E+6 Pa	0.18-m RADIUS AT AIS, 1510 KPA
7 02 1988	1.013E+6 Pa	AIS BOREHOLE DRAINS AT ATMOSPHERIC PRESSURE
05 05 1988	0.382E-03 m^3/s	PUMP RATE AT H-11 0.3820 L/S H-11 MULTIPAD TEST
17 06 1988	1.013E+5 Pa	AIR-INTAKE SHAFT PENETRATES CULEBRA WITH 3.1m RADIUS
07 07 1988	0.00 m^3/s	PUMPING AT H-11 SET TO 0.0
1 11 1988	1.013E+5 Pa	AIR-INTAKE SHAFT LINER IN PLACE, REDUCE SKIN
16 06 1995	2.46E-04 m^3/s	PUMPING AT H-19 TO 0.0246 L/S
28 07 1995	0.0 m^3/s	END PUMPING AT H-19
30 08 1995	2.27E-04 m^3/s	RESET PUMPING AT H-19
03 09 1995	0.0 m^3/s	RESET PUMPING AT H-19
08 09 1995	1.58E-04 m^3/s	RESET PUMPING AT H-19
13 09 1995	0.0 m^3/s	RESET PUMPING AT H-19
29 10 1995	5.68E-05 m^3/s	RESET PUMPING AT H-19
02 11 1995	1.526E-4 m^3/s	RESET PUMPING AT H-19
04 11 1995	0.0 m^3/s	RESET PUMPING AT H-19
10 11 1995	1.77E-4 m^3/s	RESET PUMPING AT H-19
13 11 1995	3.79E-5 m^3/s	RESET PUMPING AT H-19

Table TFIELD-9. Transient Events Simulated in the 1996 Culebra Model (Continued)

Date	Pressure or Pumping/Leakage Rate	Location and Description
15 11 1995	0.0 m^3/s	RESET PUMPING AT H-19
16 11 1995	2.56E-4 m^3/s	RESET PUMPING AT H-19
17 11 1995	0.0 m^3/s	RESET PUMPING AT H-19
15 12 1995	2.78E-4 m^3/s	RESET PUMPING AT H-19 FOR TRACER TEST
24 12 1995	2.71E-4 m^3/s	RESET PUMPING AT H-19 FOR TRACER TEST
08 01 1996	2.69E-4 m^3/s	RESET PUMPING AT H-19 FOR TRACER TEST
18 01 1996	2.46E-4 m^3/s	RESET PUMPING AT H-19 FOR TRACER TEST
07 02 1996	1.58E-4 m^3/s	RESET PUMPING AT H-11
20 02 1996	4.54E-4 m^3/s	RESET PUMPING AT WQSP-2
21 02 1996	1.58E-04 m^3/s	RESET PUMPING AT H-19 FOR TRACER TEST
24 02 1996	0.0 m^3/s	RESET PUMPING AT WQSP-2
11 03 1996	3.79E-04 m^3/s	RESET PUMPING AT H-11
27 03 1996	0.0 m^3/s	RESET PUMPING AT H-11
01 04 1996		END OF SIMULATION

Table TFIELD-10. Transient Time Steps Used in 1996 Culebra Model (relative to January 1, 1981)

Time (seconds)	Time Step	Time (seconds)	Time Step
0.00	1 time step	35337600.00	48 time step
18835200.00	2 time step	36720000.00	49 time step
18921600.00	3 time step	39484800.00	50 time step
19008000.00	4 time step	45014400.00	51 time step
19094400.00	5 time step	56073600.00	52 time step
19180800.00	6 time step	78192000.00	53 time step
19267200.00	7 time step	86659200.00	54 time step
19353600.00	8 time step	86745600.00	55 time step
19440000.00	9 time step	86918400.00	56 time step
19526400.00	10 time step	87004800.00	57 time step
19612800.00	11 time step	87091200.00	58 time step
19785600.00	12 time step	87264000.00	59 time step
20131200.00	13 time step	87609600.00	60 time step
20822400.00	14 time step	88300800.00	61 time step
22204800.00	15 time step	89683200.00	62 time step
24969600.00	16 time step	92448000.00	63 time step
25660800.00	17 time step	95385600.00	64 time step
25747200.00	18 time step	95472000.00	65 time step
25920000.00	19 time step	95644800.00	66 time step
26006400.00	20 time step	95990400.00	67 time step
26179200.00	21 time step	96681600.00	68 time step
26265600.00	22 time step	97286400.00	69 time step
26352000.00	23 time step	97372800.00	70 time step
26438400.00	24 time step	97545600.00	71 time step
26611200.00	25 time step	97891200.00	72 time step
26697600.00	26 time step	98582400.00	73 time step
26870400.00	27 time step	99964800.00	74 time step
26956800.00	28 time step	102729600.0	75 time step
27129600.00	29 time step	102816000.0	76 time step
27216000.00	30 time step	102902400.0	77 time step
27388800.00	31 time step	103075200.0	78 time step
27475200.00	32 time step	103420800.0	79 time step
27648000.00	33 time step	104112000.0	80 time step
27734400.00	34 time step	105494400.0	81 time step
27907200.00	35 time step	108259200.0	82 time step
28252800.00	36 time step	113788800.0	83 time step
28944000.00	37 time step	114652800.0	84 time step
29289600.00	38 time step	114739200.0	85 time step
29376000.00	39 time step	114912000.0	86 time step
29548800.00	40 time step	115257600.0	87 time step
29894400.00	41 time step	115948800.0	88 time step
30585600.00	42 time step	117331200.0	89 time step
31968000.00	43 time step	119491200.0	90 time step
34041600.00	44 time step	119577600.0	91 time step
34128000.00	45 time step	119750400.0	92 time step
34300800.00	46 time step	120096000.0	93 time step
34646400.00	47 time step	120787200.0	94 time step

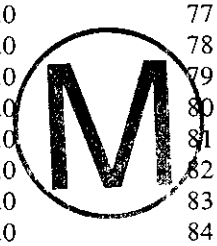

Table TFIELD-10. Transient Time Steps Used in 1996 Culebra Model (relative to January 1, 1981) (Continued)

Time (seconds)	Time Step	Time (seconds)	Time Step
122169600.0	95 time step	191548800.0	142 time step
123811200.0	96 time step	191635200.0	143 time step
123897600.0	97 time step	191808000.0	144 time step
124070400.0	98 time step	192153600.0	145 time step
124416000.0	99 time step	192240000.0	146 time step
125107200.0	100 time step	192326400.0	147 time step
126489600.0	101 time step	192499200.0	148 time step
129254400.0	102 time step	192844800.0	149 time step
134784000.0	103 time step	192931200.0	150 time step
140918400.0	104 time step	193104000.0	151 time step
141004800.0	105 time step	193363200.0	152 time step
141177600.0	106 time step	194054400.0	153 time step
141264000.0	107 time step	195436800.0	154 time step
141350400.0	108 time step	198201600.0	155 time step
141523200.0	109 time step	202348800.0	156 time step
141609600.0	110 time step	203040000.0	157 time step
141696000.0	111 time step	204422400.0	158 time step
141868800.0	112 time step	204940800.0	159 time step
142214400.0	113 time step	205632000.0	160 time step
142300800.0	114 time step	207014400.0	161 time step
142473600.0	115 time step	209779200.0	162 time step
142646400.0	116 time step	215308800.0	163 time step
142992000.0	117 time step	215568000.0	164 time step
143078400.0	118 time step	216259200.0	165 time step
143424000.0	119 time step	217641600.0	166 time step
144115200.0	120 time step	220406400.0	167 time step
145497600.0	121 time step	220838400.0	168 time step
148262400.0	122 time step	221529600.0	169 time step
151027200.0	123 time step	222134400.0	170 time step
151372800.0	124 time step	223516800.0	171 time step
152064000.0	125 time step	223603200.0	172 time step
153446400.0	126 time step	224294400.0	173 time step
156211200.0	127 time step	224726400.0	174 time step
156384000.0	128 time step	226108800.0	175 time step
157075200.0	129 time step	228873600.0	176 time step
158457600.0	130 time step	231638400.0	177 time step
161222400.0	131 time step	232329600.0	178 time step
166752000.0	132 time step	233712000.0	179 time step
174614400.0	133 time step	235353600.0	180 time step
175305600.0	134 time step	236044800.0	181 time step
176688000.0	135 time step	237081600.0	182 time step
179452800.0	136 time step	237772800.0	183 time step
184982400.0	137 time step	239155200.0	184 time step
190252800.0	138 time step	241920000.0	185 time step
190339200.0	139 time step	247190400.0	186 time step
190512000.0	140 time step	247881600.0	187 time step
190857600.0	141 time step	249264000.0	188 time step

Table TFIELD-10. Transient Time Steps Used in 1996 Culebra Model (relative to January 1, 1981) (Continued)

Time (seconds)	Time Step	Time (seconds)	Time Step
252028800.0	189 time step	469065600.0	237 time step
257558400.0	190 time step	469152000.0	238 time step
268617600.0	191 time step	469238400.0	239 time step
290736000.0	192 time step	469324800.0	240 time step
312854400.0	193 time step	469411200.0	241 time step
334972800.0	194 time step	469497600.0	242 time step
357091200.0	195 time step	469670400.0	243 time step
379209600.0	196 time step	470016000.0	244 time step
401328000.0	197 time step	470707200.0	245 time step
423446400.0	198 time step	471830400.0	246 time step
445564800.0	199 time step	471916800.0	247 time step
456105600.0	200 time step	472089600.0	248 time step
456192000.0	201 time step	472435200.0	249 time step
456364800.0	202 time step	472608000.0	250 time step
456710400.0	203 time step	472694400.0	251 time step
457401600.0	204 time step	472867200.0	252 time step
458784000.0	205 time step	473212800.0	253 time step
459734400.0	206 time step	473904000.0	254 time step
459820800.0	207 time step	473990400.0	255 time step
459993600.0	208 time step	474076800.0	256 time step
460339200.0	209 time step	474249600.0	257 time step
461030400.0	210 time step	474595200.0	258 time step
462412800.0	211 time step	474854400.0	259 time step
462585600.0	212 time step	474940800.0	260 time step
462672000.0	213 time step	475113600.0	261 time step
462844800.0	214 time step	475459200.0	262 time step
462931200.0	215 time step	476150400.0	263 time step
463017600.0	216 time step	476582400.0	264 time step
463190400.0	217 time step	476668800.0	265 time step
463363200.0	218 time step	476841600.0	266 time step
463449600.0	219 time step	477187200.0	267 time step
463622400.0	220 time step	477705600.0	268 time step
463795200.0	221 time step	477792000.0	269 time step
463881600.0	222 time step	477878400.0	270 time step
464054400.0	223 time step	478051200.0	271 time step
464400000.0	224 time step	478137600.0	272 time step
465091200.0	225 time step	478310400.0	273 time step
466473600.0	226 time step	478656000.0	274 time step
467769600.0	227 time step	479347200.0	275 time step
467856000.0	228 time step	479433600.0	276 time step
468028800.0	229 time step	479520000.0	277 time step
468115200.0	230 time step	479692800.0	278 time step
468201600.0	231 time step	480038400.0	279 time step
468288000.0	232 time step	480729600.0	280 time step
468374400.0	233 time step	480816000.0	281 time step
468547200.0	234 time step	480902400.0	282 time step
468806400.0	235 time step	481075200.0	283 time step
468892800.0	236 time step	481248000.0	284 time step

the median transmissivity value of -5.95 ($\log_{10}$ meters squared per second) was used as the cutoff between the high and low transmissivity categories. The categorical simulation determined the transmissivity categorical variable (that is, high transmissivity or low transmissivity) for each grid block in the model domain. Once determined, sequential Gaussian simulation was subsequently used to obtain grid-block transmissivity values separately for the high and low transmissivity grid blocks.

One hundred CS transmissivity fields were generated and subsequently calibrated to the observed steady-state and transient-state freshwater head data using the approach detailed in Section TFIELD.3. A plot of each calibrated field is contained in Attachment A. Once calibrated, the 100 CS transmissivity fields were analyzed to determine the quality of the fit to the observed heads and to investigate the variability of the transmissivity fields. As in LaVenue and RamaRao (1992), an ensemble mean calculation was performed across the realizations to determine the average transmissivity value at each grid block. The resulting ensemble transmissivity field (Figure TFIELD-30) has features that are very similar to the 1992 ensemble mean transmissivity field. Outside the WIPP site area, the reentry of high transmissivities from the Nash Draw area occurs south of the WIPP site near the H-7 borehole and the high-transmissivity zone within the WIPP site boundary, as represented in the ensemble mean field (Figure TFIELD-30), and extends northward from the P-17 borehole where it narrowly lies between the P-17 and H-17 boreholes. Entering the controlled area from the south, the high-transmissivity zone widens significantly extending westward to the H-3 and H-19 boreholes and eastward beyond the H-11 and DOE-1 boreholes.

Figures TFIELD-31 through TFIELD-33 are examples of three calibrated fields. These fields are taken from random seeds 40, 69, and 77, respectively. They were chosen to illustrate different characteristics. For example, the transmissivities for each of these fields in the vicinity of the H-1 borehole are low. However, in field 40 the conditional simulation also placed a very high transmissivity zone between H-1 and H-3, whereas in field 69 a much lower transmissivity rests between H-1 and H-3. This variability is due to the uncertainty in the location of high transmissivity field zones within the WIPP site boundary, and is the reason for simulating high and low categories across the model domain. As observed in these three figures, the higher transmissivities are connected in a much more tortuous fashion than previously determined in the 1992 study. The finer grid, coupled with the model grid blocks being specified with categorical indicators and separately optimized, enables the code to produce transmissivity fields that may have distinct contrasts in transmissivity between neighboring grid blocks.

TFIELD.4.2.2 Ensemble Steady-State and Transient Head Differences

The differences between the calculated and observed steady-state heads were determined in order to summarize the fit of each realization to the steady-state data. A scatterplot of the ensemble-mean calculated heads versus observed heads is illustrated in Figure TFIELD-34a. The mean heads agree well with the observed steady-state heads and are lower than those calculated in the 1992 model. This difference is probably due to the ability of this version of

GRASP-INV to optimize independently the transmissivity of the regions of the model associated with high and low transmissivities. Figure TFIELD-34b contains a histogram of the differences of the heads shown in Figure TFIELD-34a. As shown, most of the differences between the mean-calculated and observed heads fall between -0.5 and 1.0 meters. The simulation with the worst steady-state head fit is shown to have a head difference falling between 2.0 and 2.5 meters. This particular realization illustrates a situation in which the CS field contained features that significantly reduced the ability of the GRASP-INV code to calibrate the field to steady-state conditions with 50 calibration steps. Although GRASP-INV could theoretically bring the head field into agreement with the observed data by adding more than the allowed 50 points to reduce head differences, the tradeoff would be a loss in the predictive capability of the code because of the extensive modifications required to produce a perfect fit. Thus, for the purpose of the code in the performance assessment, restricting the calibration procedure to 50 steps appears to be suitable despite occasional differences between the head field and observed data.

The ensemble mean transient heads were also calculated across the realizations and compared to the measured transient heads. Figures TFIELD-35 through TFIELD-38 depict the hydrographs for the time period 1981 through 1990. The calculated heads match the measured heads excellently for effects of the regional scale pumping tests at H-3, WIPP-13, and H-11. As in previous modeling studies of the Culebra (LaVenue et al. 1989; LaVenue and RamaRao 1992), the drawdown of the boreholes responding to pumping at H-11 is correct but the drawdown recovery time is too slow. This discrepancy indicates that the storativity used for this part of the model may be too high. In addition, the drawdowns associated with the shaft construction are under-predicted by the model, which is probably caused by the way in which the shaft effects are simulated. Because of the parsity of leakage data from the shafts, only shaft pressures could be specified for most of the simulation time period. This condition leads to a problem when the transmissivity varies at the shaft location from one realization to the next. A relatively low transmissivity value in the shaft area reduces the area affected by drawdown due to an atmospheric pressure in the shaft.

The transient heads calculated from the pumping tests that occurred in 1995 and 1996 are illustrated in Figures TFIELD-39 through TFIELD-42. The fit to the drawdowns caused by pumping at H-11 and H-19 is excellent. This agreement indicates that the transmissivities in the southern portion of the WIPP site are represented well by the model. As discussed in Section TFIELD.4.1.5, the drawdowns associated with the H-19 tracer test were not used during model calibration. The calculated drawdowns were, however, used to verify that the calibration produced transmissivity fields useful for predicting hydraulic response in the Culebra. The calculated and observed drawdowns during the H-19 tracer test (December 1995 through March 1996 on Figures TFIELD-39 and TFIELD-40) agree well, which verifies the calibrated transmissivities. In addition, the calculated drawdowns due to pumping at WQSP-2 are approximately the same as the measured drawdowns. The most significant difference occurs at the WIPP-12 borehole where the calculated drawdown is too large.

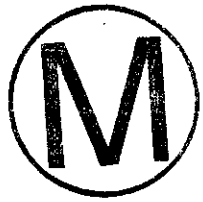

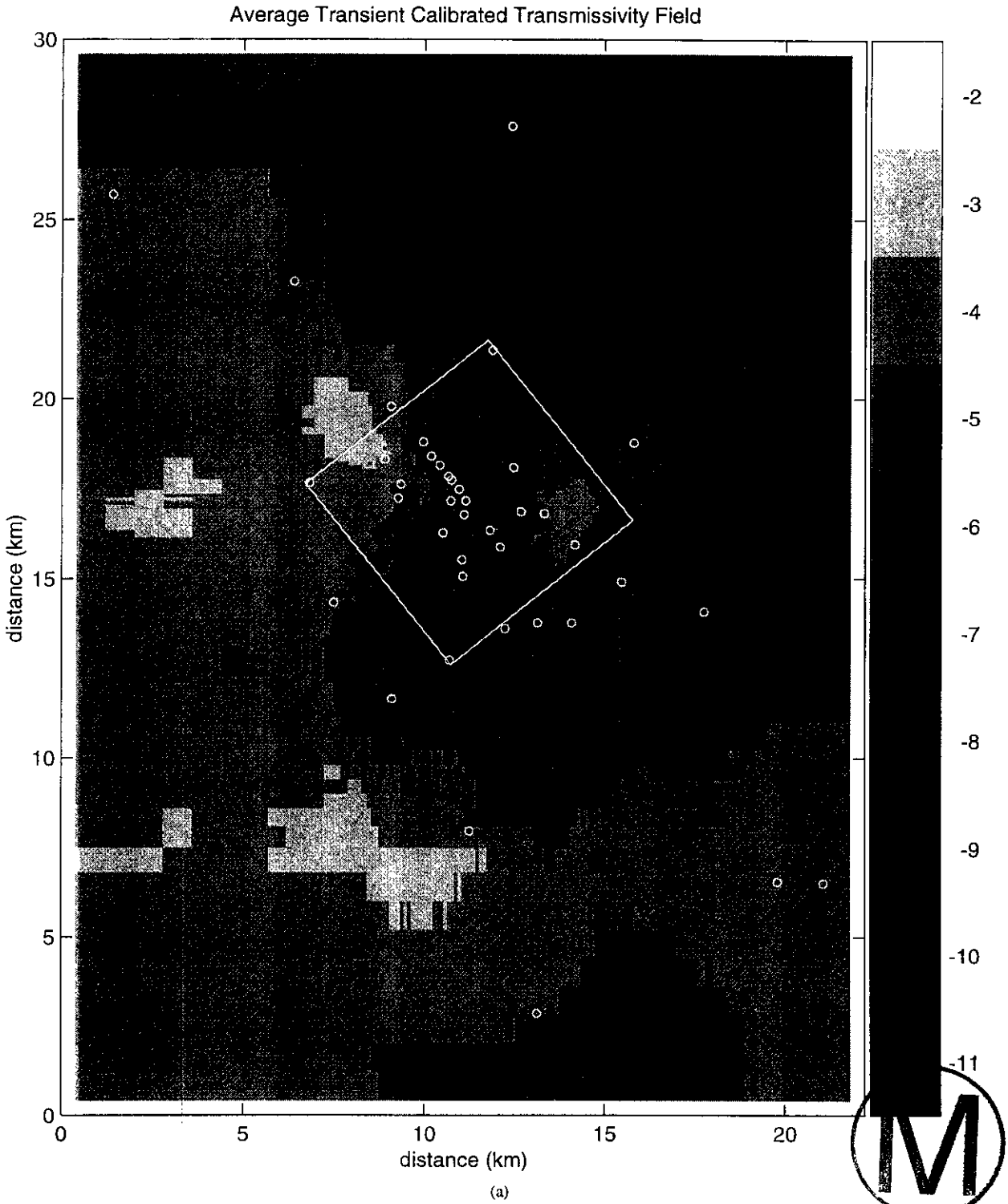

(a)

On the plot, the direction North is parallel to the east/west boundaries of the WIPP site and thus is pointed at the upper left corner of the figure.

Figure TFIELD-30. Ensemble Transmissivity Field resulting from a Mean Calculation Performed across the Realizations for (a) the Full-Scale Model and (b) the WIPP Site Boundary Area

1 THIS PAGE INTENTIONALLY LEFT BLANK

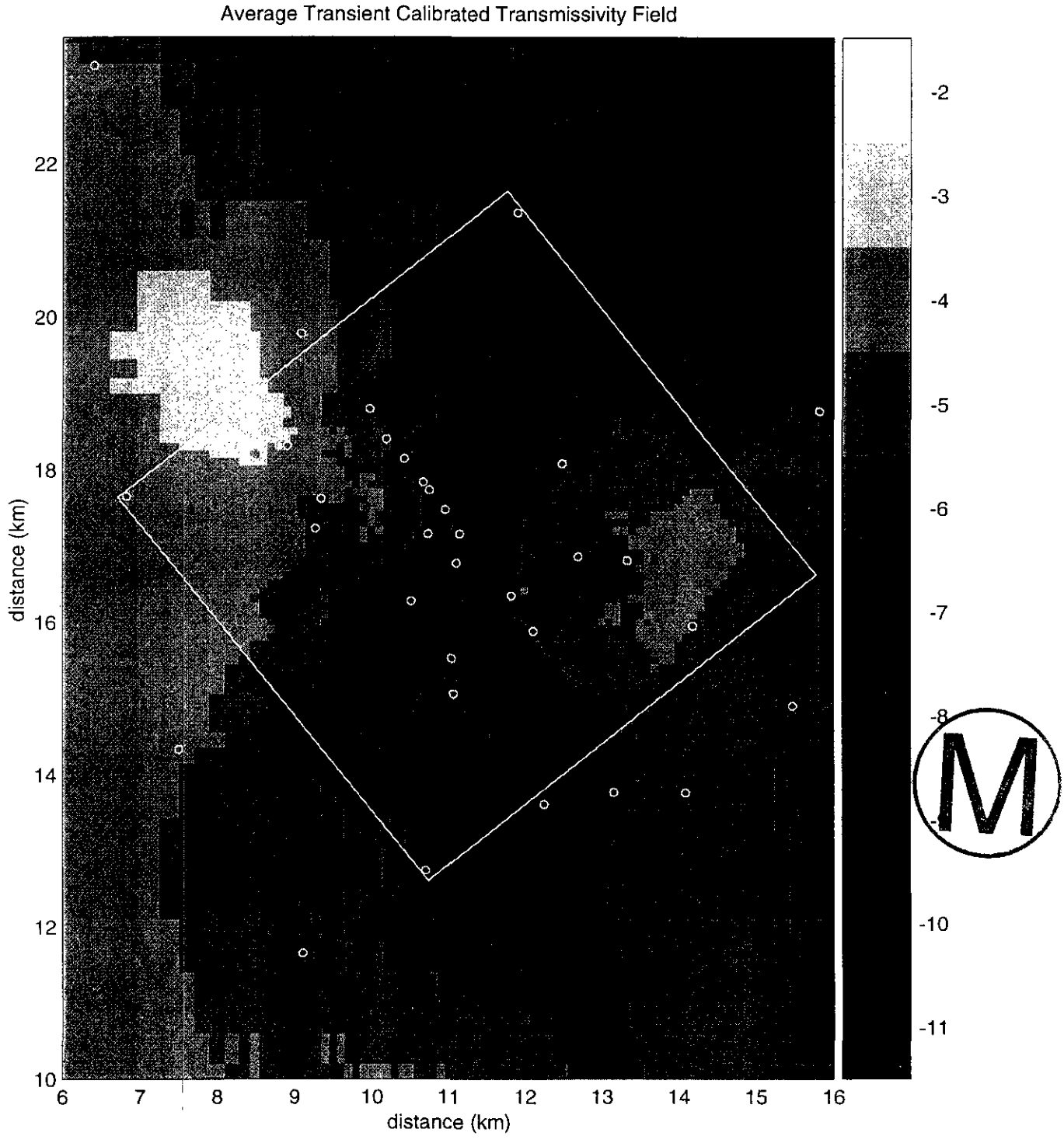

(b)

On the plot, the direction North is parallel to the east/west boundaries of the WIPP site and thus is pointed at the upper left corner of the figure.

Figure TFIELD-30. Ensemble Transmissivity Field resulting from a Mean Calculation Performed across the Realizations for (a) the Full-Scale Model and (b) the WIPP Site Boundary Area (Continued)

1 THIS PAGE INTENTIONALLY LEFT BLANK

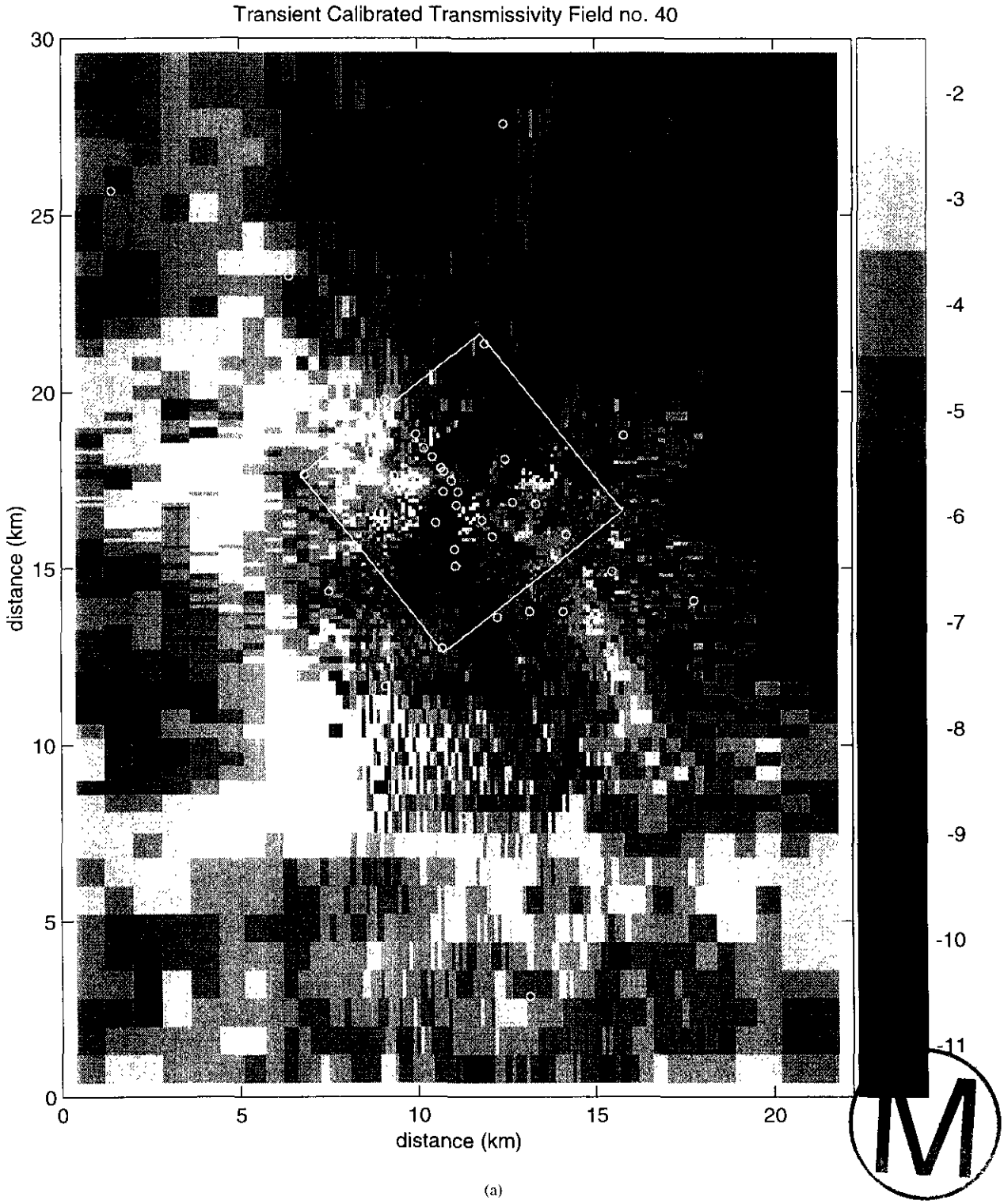

(a)

On the plot, the direction North is parallel to the east/west boundaries of the WIPP site and thus is pointed at the upper left corner of the figure.

Figure TFIELD-31. Calibrated Transmissivity Field for Realization Number 40 for (a) the Full-Scale Model and (b) the WIPP Site Boundary Area

1 THIS PAGE INTENTIONALLY LEFT BLANK

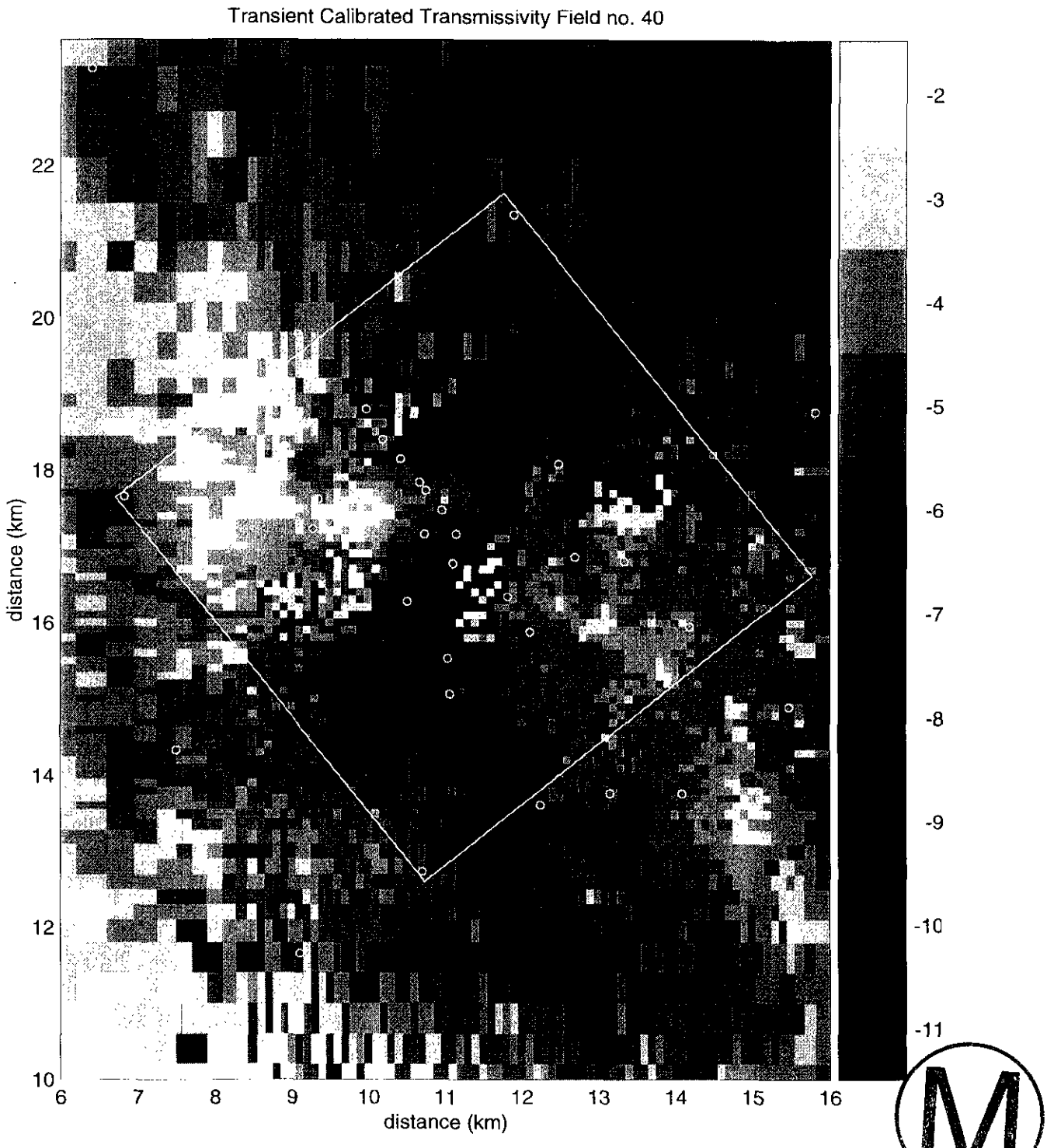

(b)

On the plot, the direction North is parallel to the east/west boundaries of the WIPP site and thus is pointed at the upper left corner of the figure.

Figure TFIELD-31. Calibrated Transmissivity Field for Realization Number 40 for (a) the Full-Scale Model and (b) the WIPP Site Boundary Area (Continued)

1 THIS PAGE INTENTIONALLY LEFT BLANK

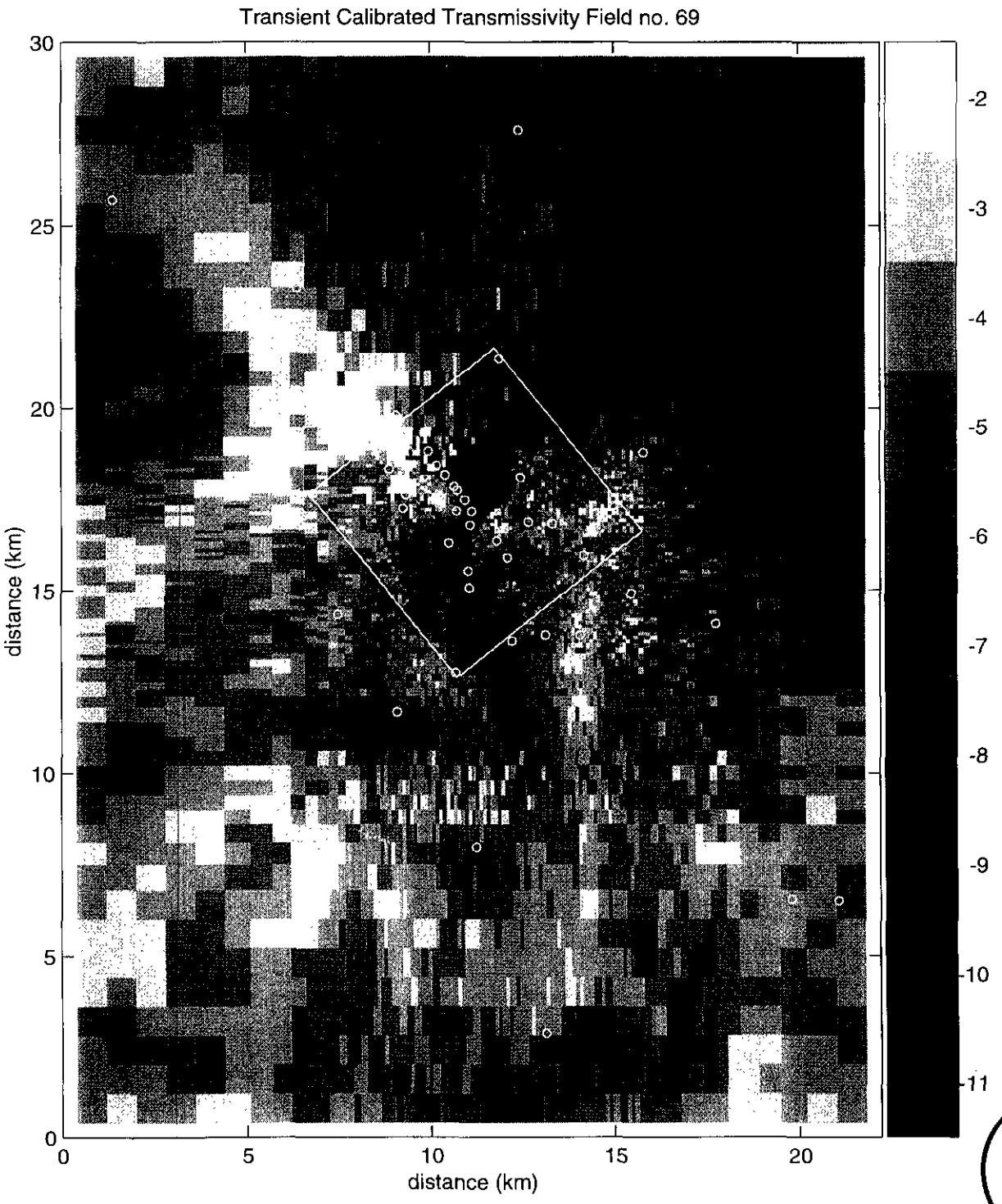

(a)

(On the plot, the direction North is parallel to the east/west boundaries of the WIPP site and thus is pointed at the upper left corner of the figure.)

Figure TFIELD-32. Calibrated Transmissivity Field for Realization Number 69 for (a) the Full-Scale Model and (b) the WIPP Site Boundary Area

1 THIS PAGE INTENTIONALLY LEFT BLANK

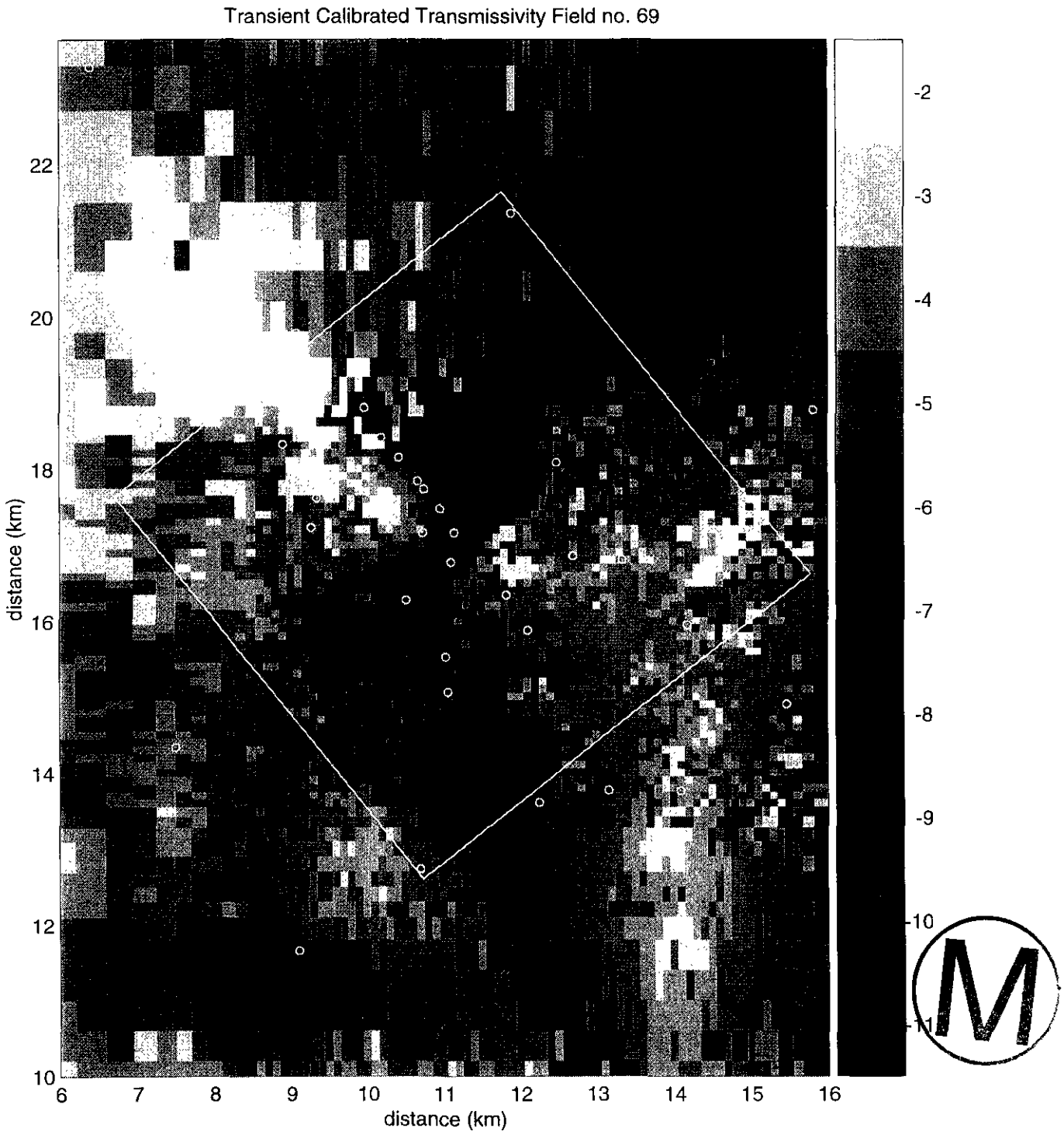

(b)

(On the plot, the direction North is parallel to the east/west boundaries of the WIPP site and thus is pointed at the upper left corner of the figure.)

Figure TFIELD-32. Calibrated Transmissivity Field for Realization Number 69 for (a) the Full-Scale Model and (b) the WIPP Site Boundary Area (Continued)

1 THIS PAGE INTENTIONALLY LEFT BLANK

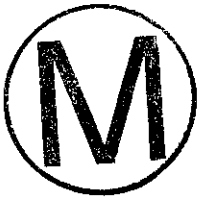

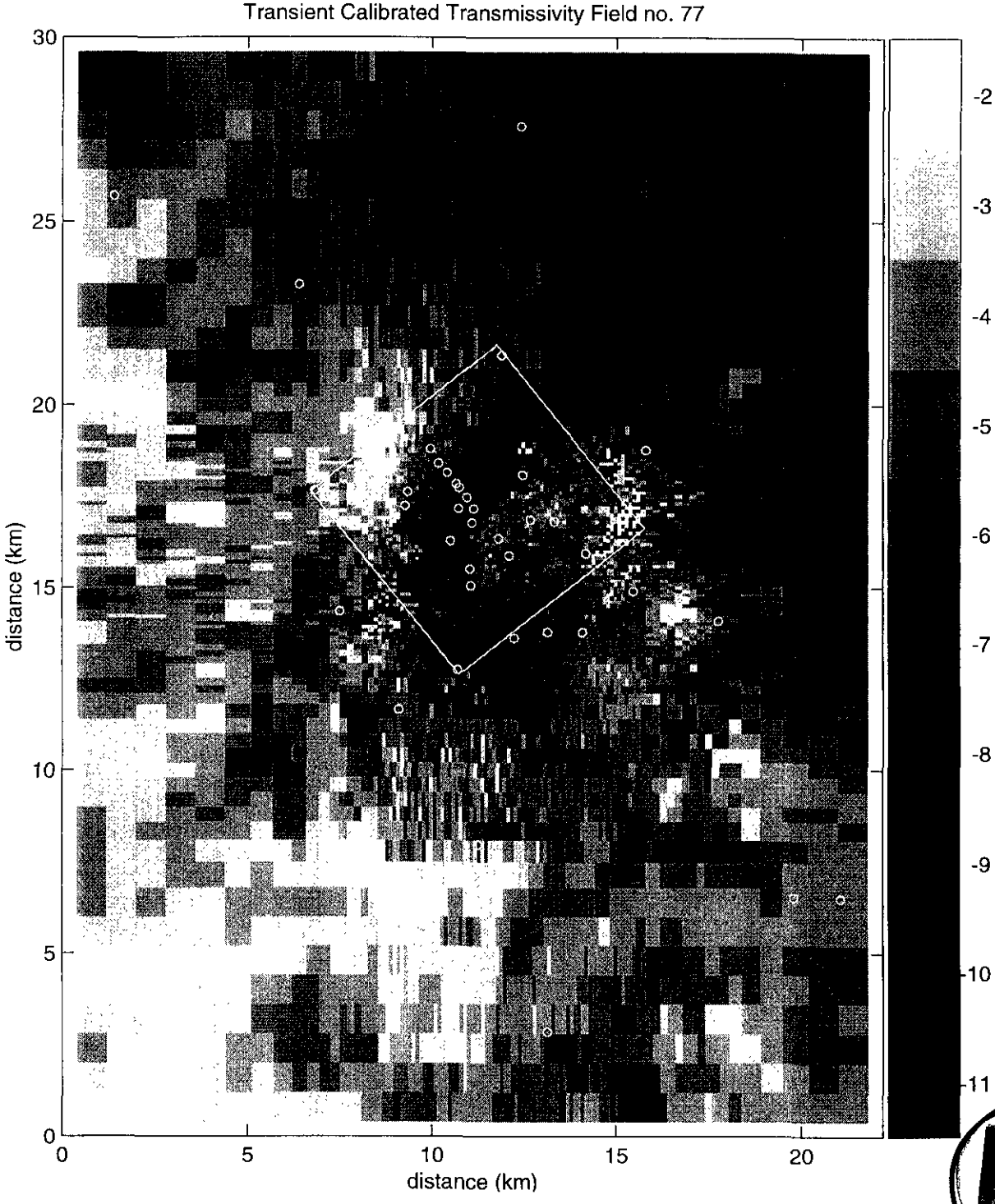

(a)

(On the plot, the direction North is parallel to the east/west boundaries of the WIPP site and thus is pointed at the upper left corner of the figure.)

Figure TFIELD-33. Calibrated Transmissivity Field for Realization Number 77 for (a) the Full-Scale Model and (b) the WIPP Site Boundary Area

1 THIS PAGE INTENTIONALLY LEFT BLANK

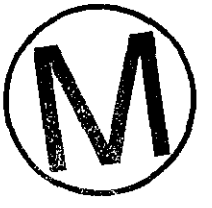

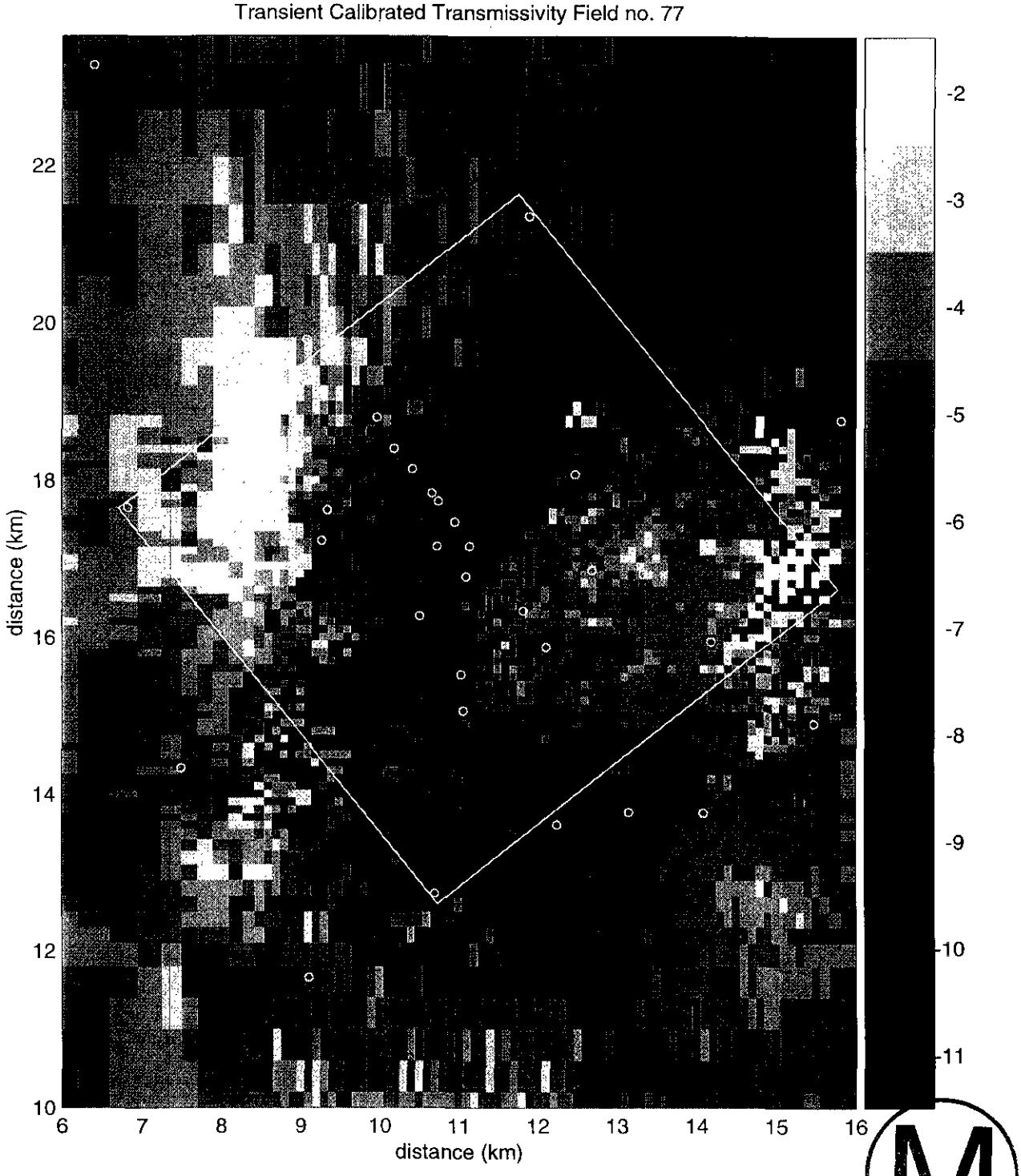

(b)

(On the plot, the direction North is parallel to the east/west boundaries of the WIPP site and thus is pointed at the upper left corner of the figure.)

Figure TFIELD-33. Calibrated Transmissivity Field for Realization Number 77 for (a) the Full-Scale Model and (b) the WIPP Site Boundary Area (Continued)

1 THIS PAGE INTENTIONALLY LEFT BLANK

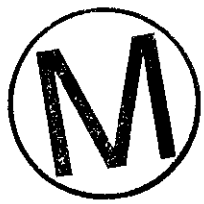

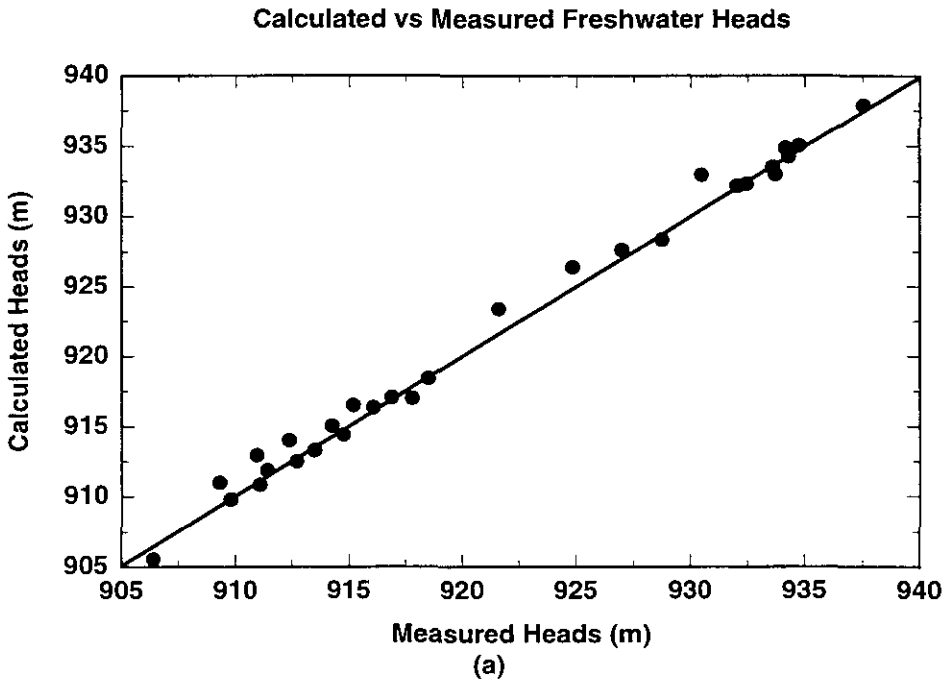

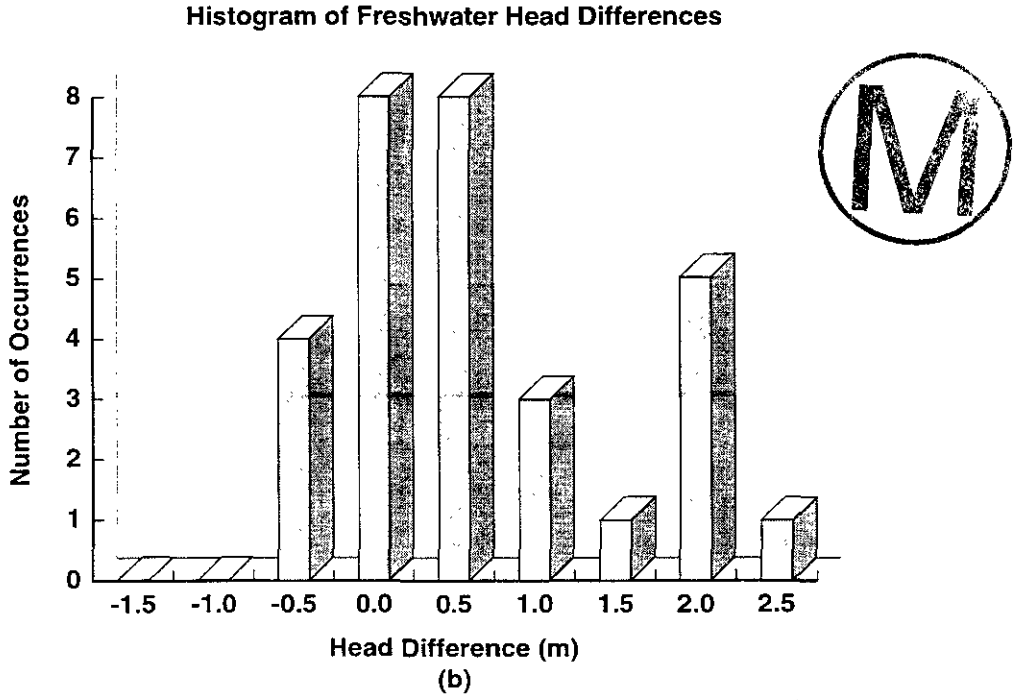

Figure TFIELD-34. (a) Scatterplot of Ensemble-Mean Steady-State Heads versus Measured Heads and (b) Histogram of Differences between Calculated Heads and Measured Heads

THIS PAGE INTENTIONALLY LEFT BLANK

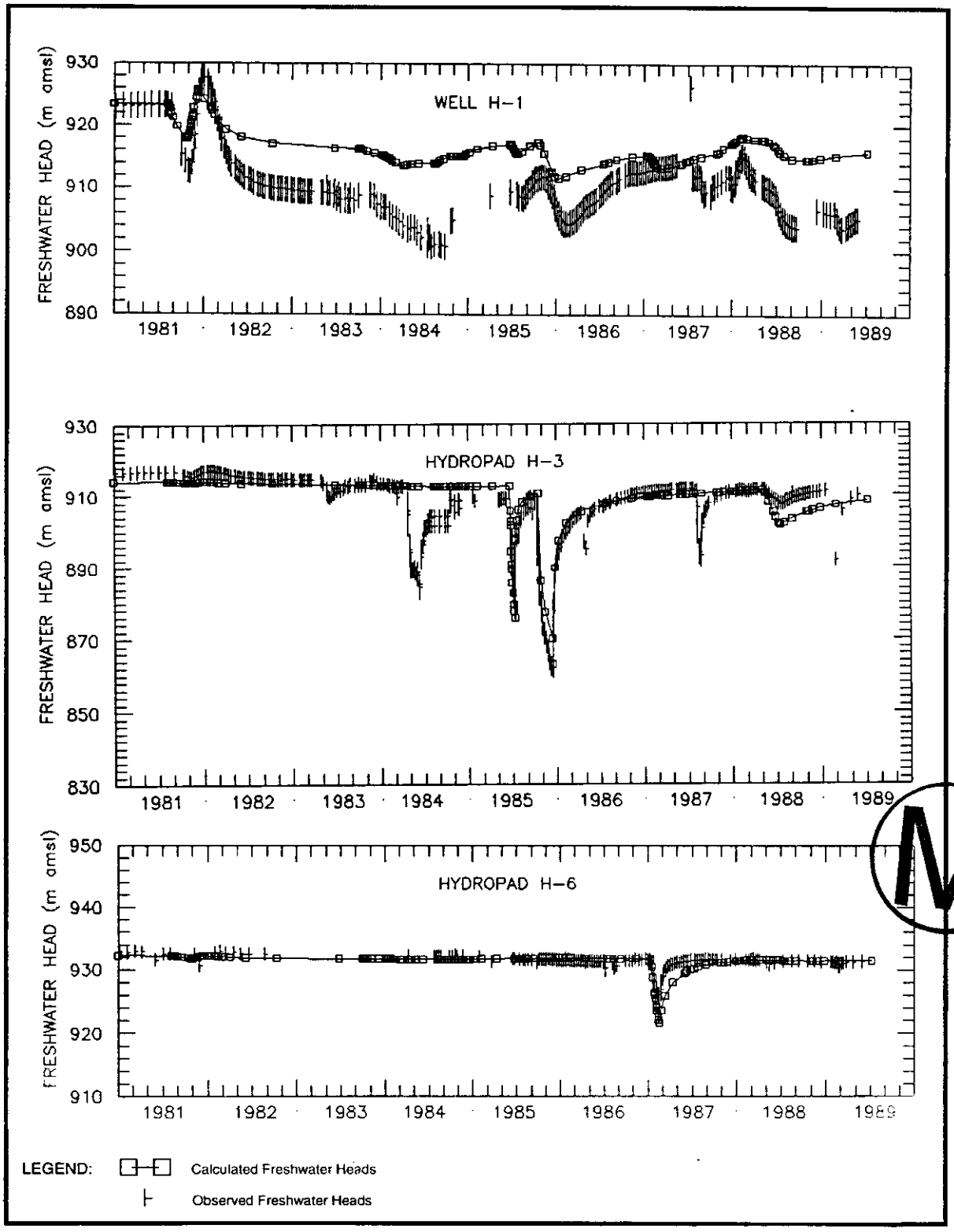

Figure TFIELD-35. Calculated and Measured Heads from 1981 to 1990 at WIPP Boreholes H-1, H-3, and H-6

1 THIS PAGE INTENTIONALLY LEFT BLANK

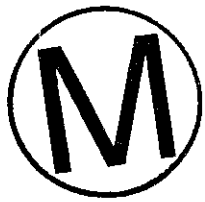

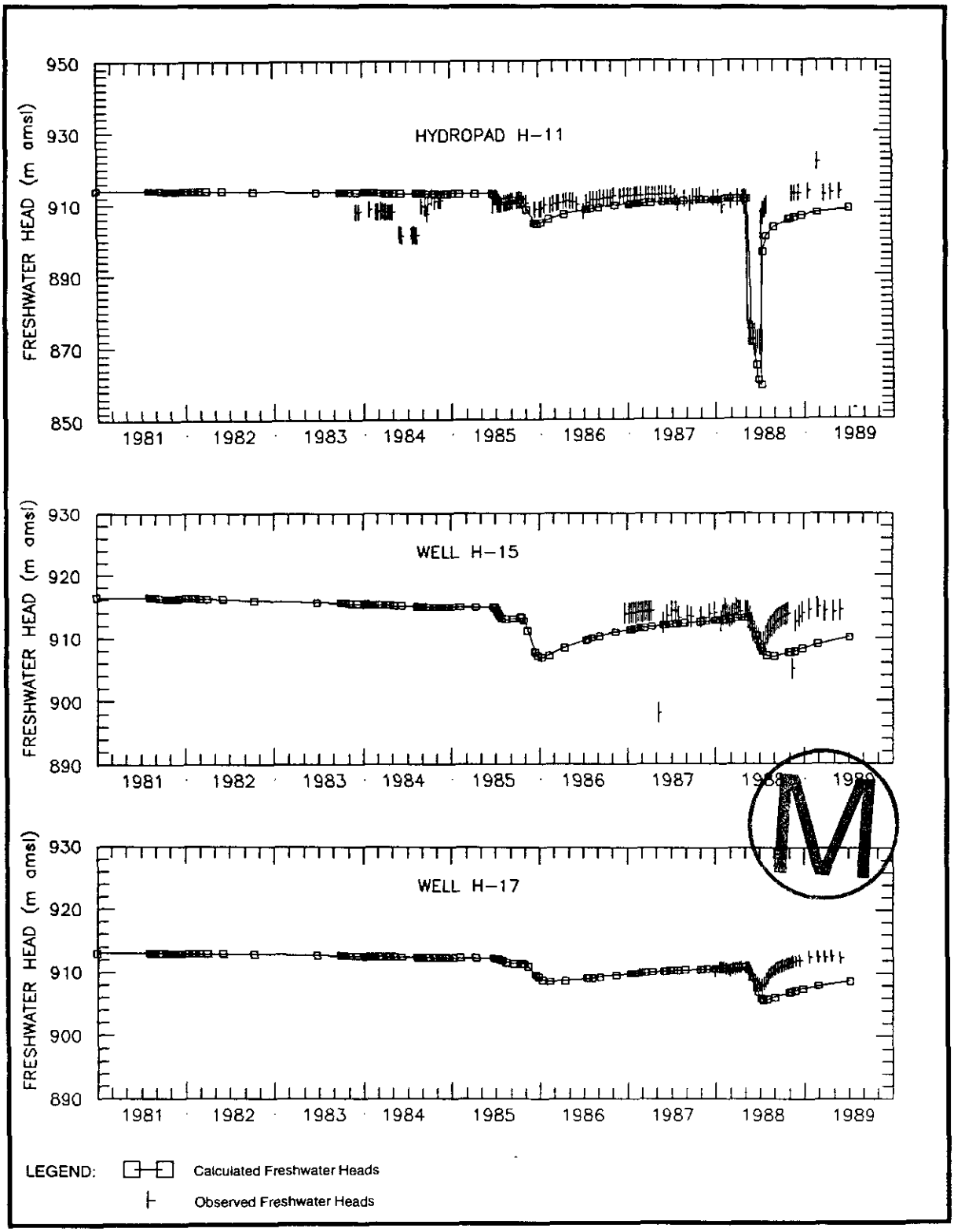

Figure TFIELD-36. Calculated and Measured Heads from 1981 to 1990 at WIPP Boreholes H-11, H-15, and H-17

1 THIS PAGE INTENTIONALLY LEFT BLANK

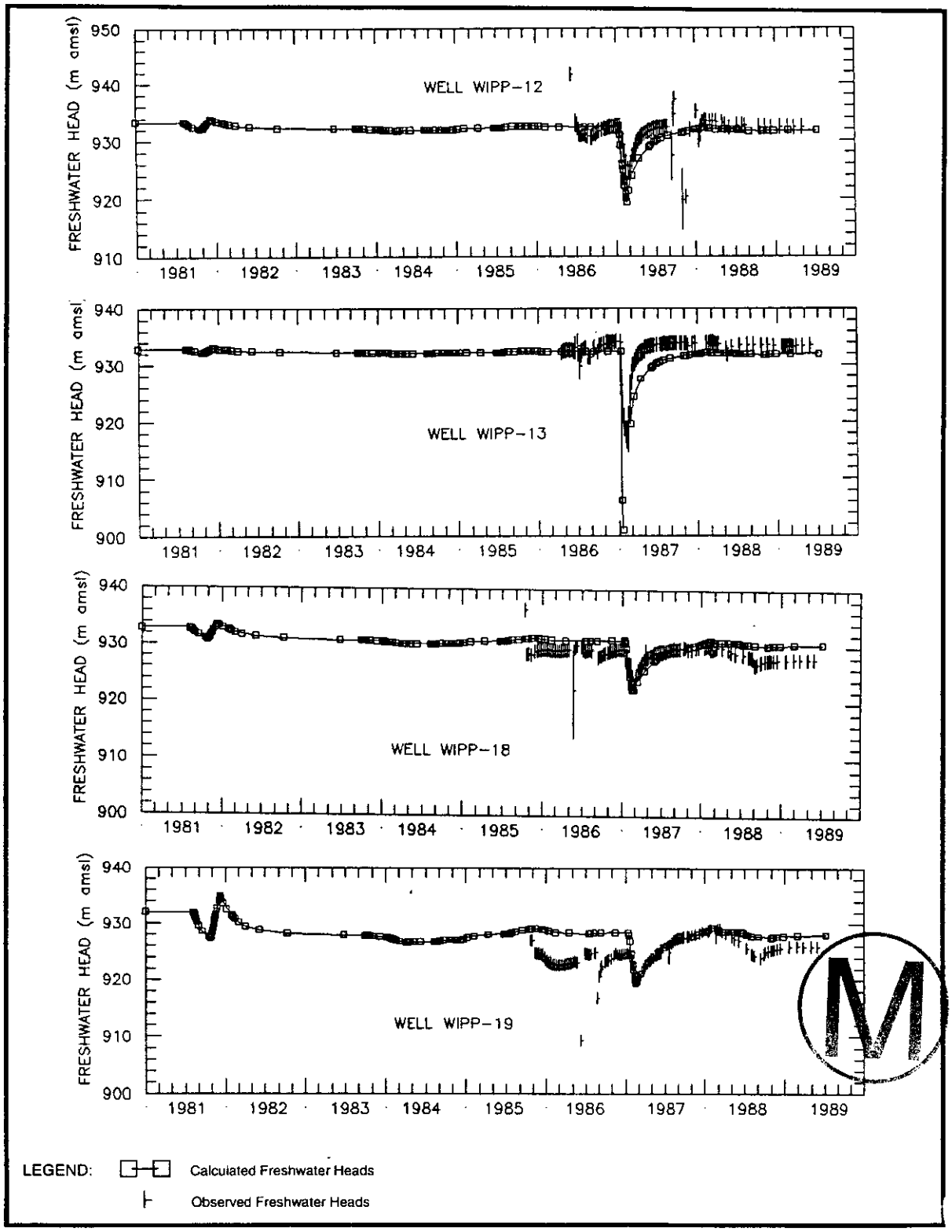

Figure TFIELD-37. Calculated and Measured Heads from 1981 to 1990 at WIPP Boreholes WIPP-12, WIPP-13, WIPP-18, and WIPP-19

1 **THIS PAGE INTENTIONALLY LEFT BLANK**

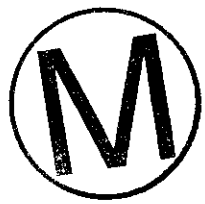

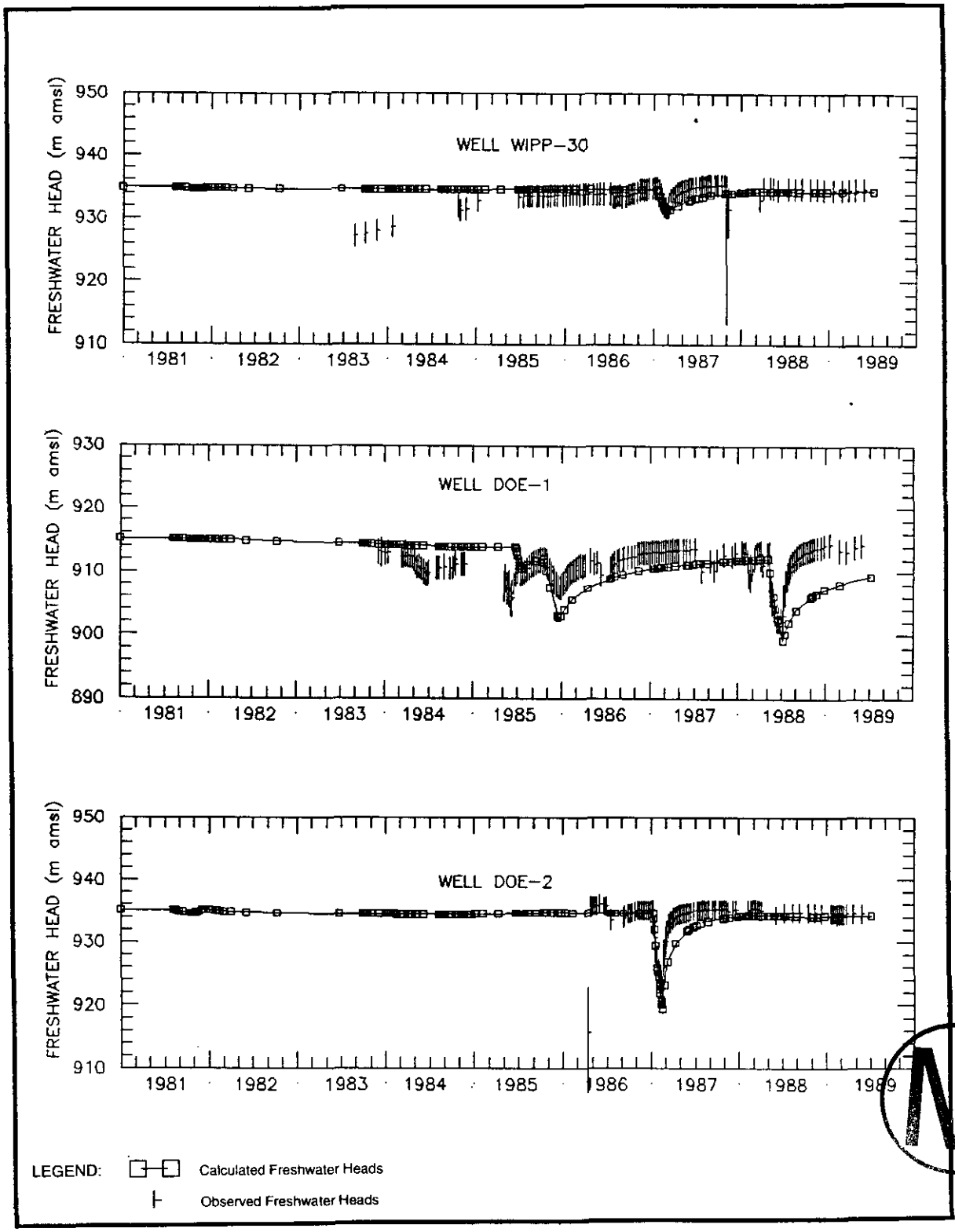

Figure TFIELD-38. Calculated and Measured Heads from 1981 to 1990 at WIPP Boreholes WIPP-30, DOE-1, and DOE-2

1 THIS PAGE INTENTIONALLY LEFT BLANK

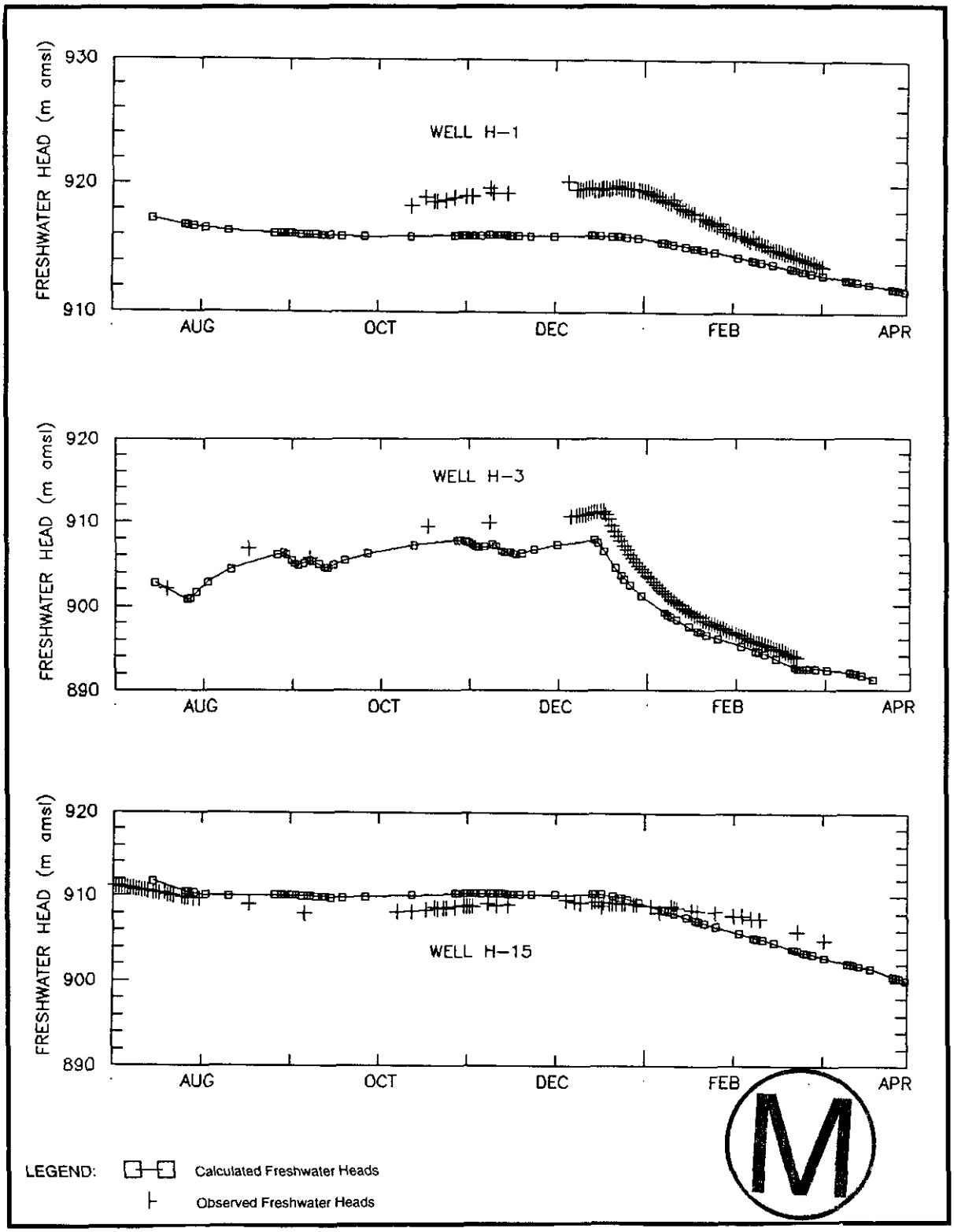

Figure TFIELD-39. Calculated and Measured Heads from 1995 to April 1996 at WIPP Boreholes H-1, H-3, and H-15

1 **THIS PAGE INTENTIONALLY LEFT BLANK**

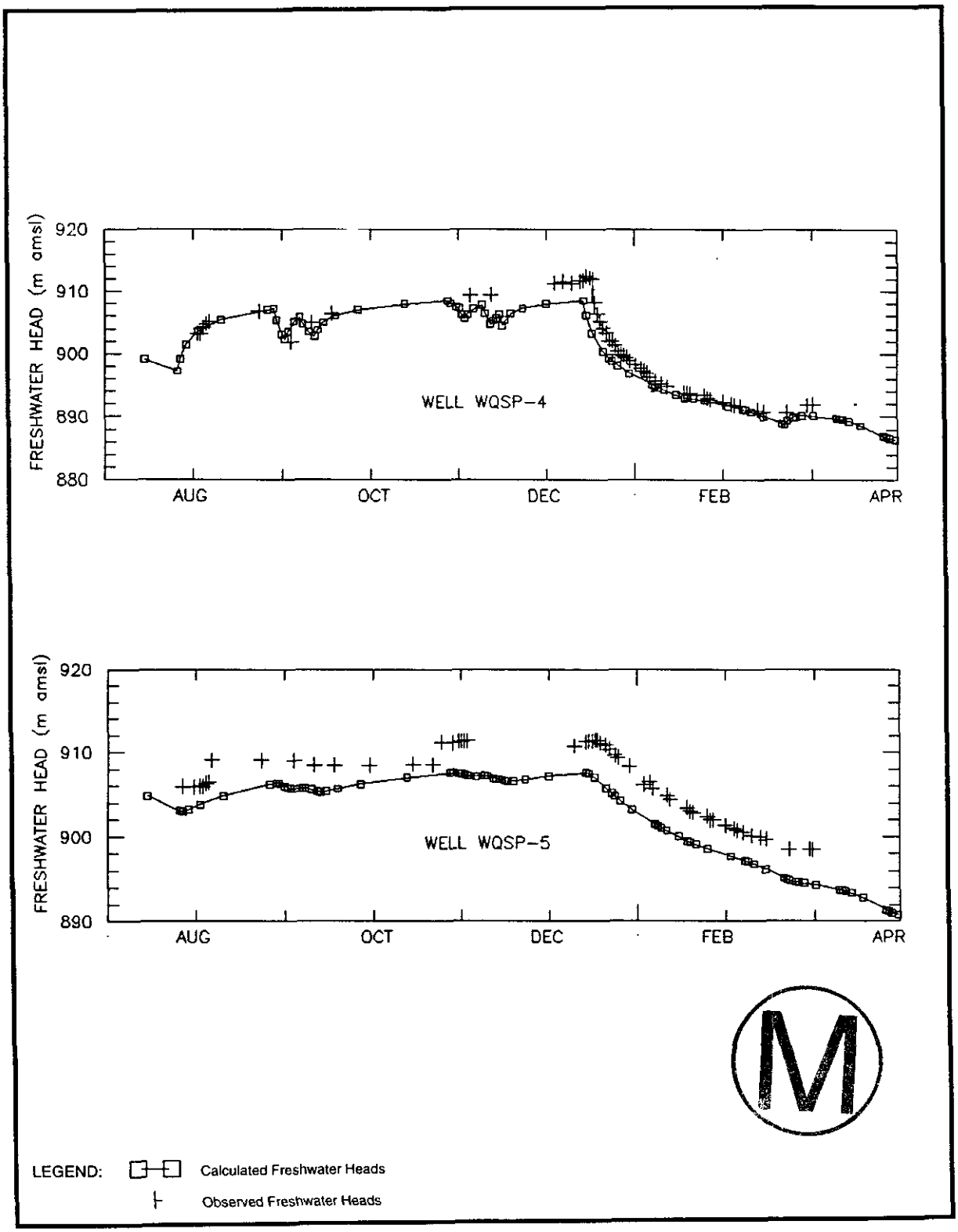

Figure TFIELD-40. Calculated and Measured Heads from 1995 to April 1996 at WIPP Boreholes WQSP-4 and WQSP-5

1 THIS PAGE INTENTIONALLY LEFT BLANK

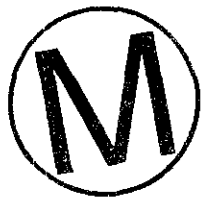

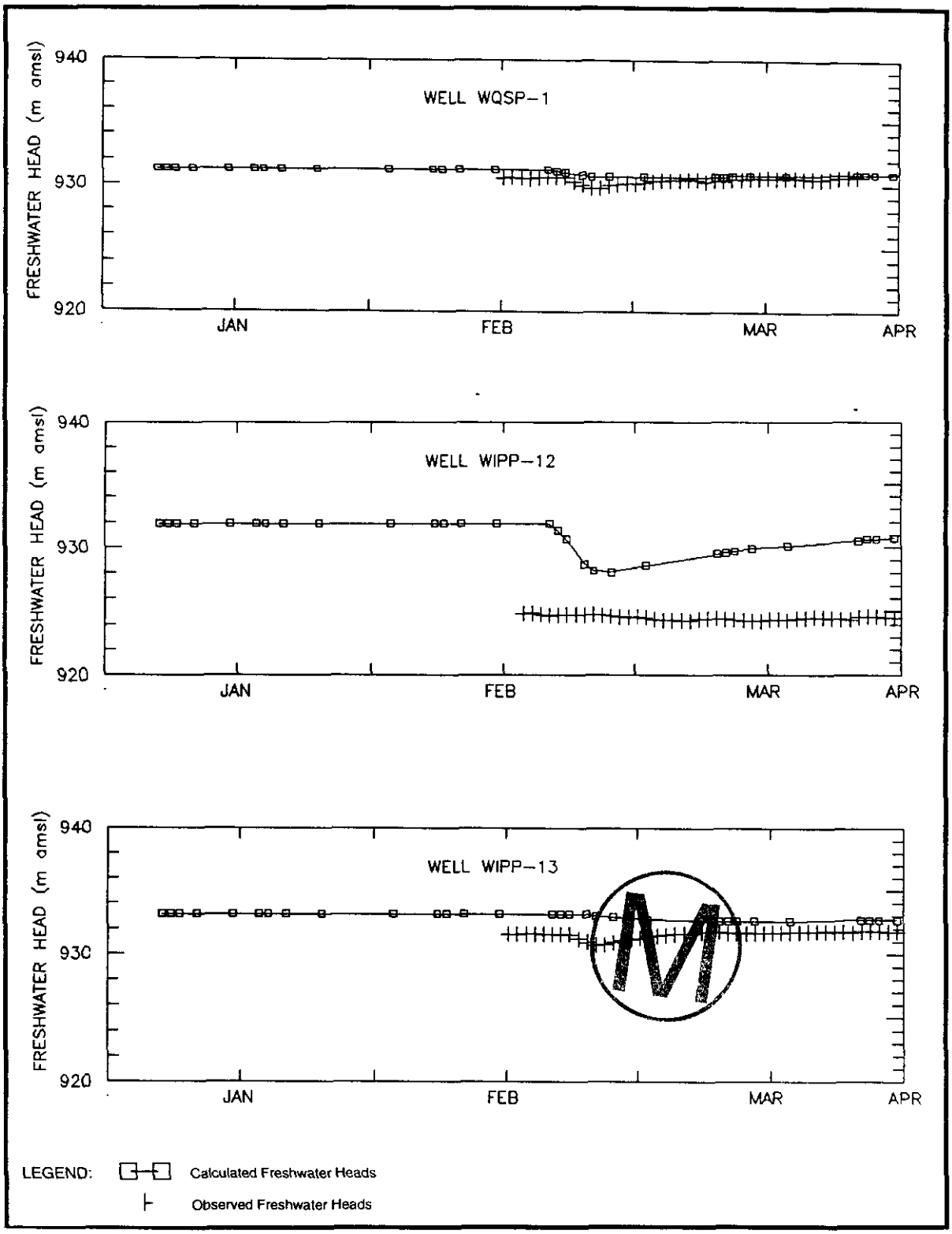

Figure TFIELD-41. Calculated and Measured Heads from 1995 to April 1996 at WIPP Boreholes WQSP-1, WIPP-12, and WIPP-13

1 THIS PAGE INTENTIONALLY LEFT BLANK

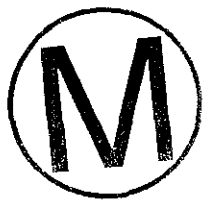

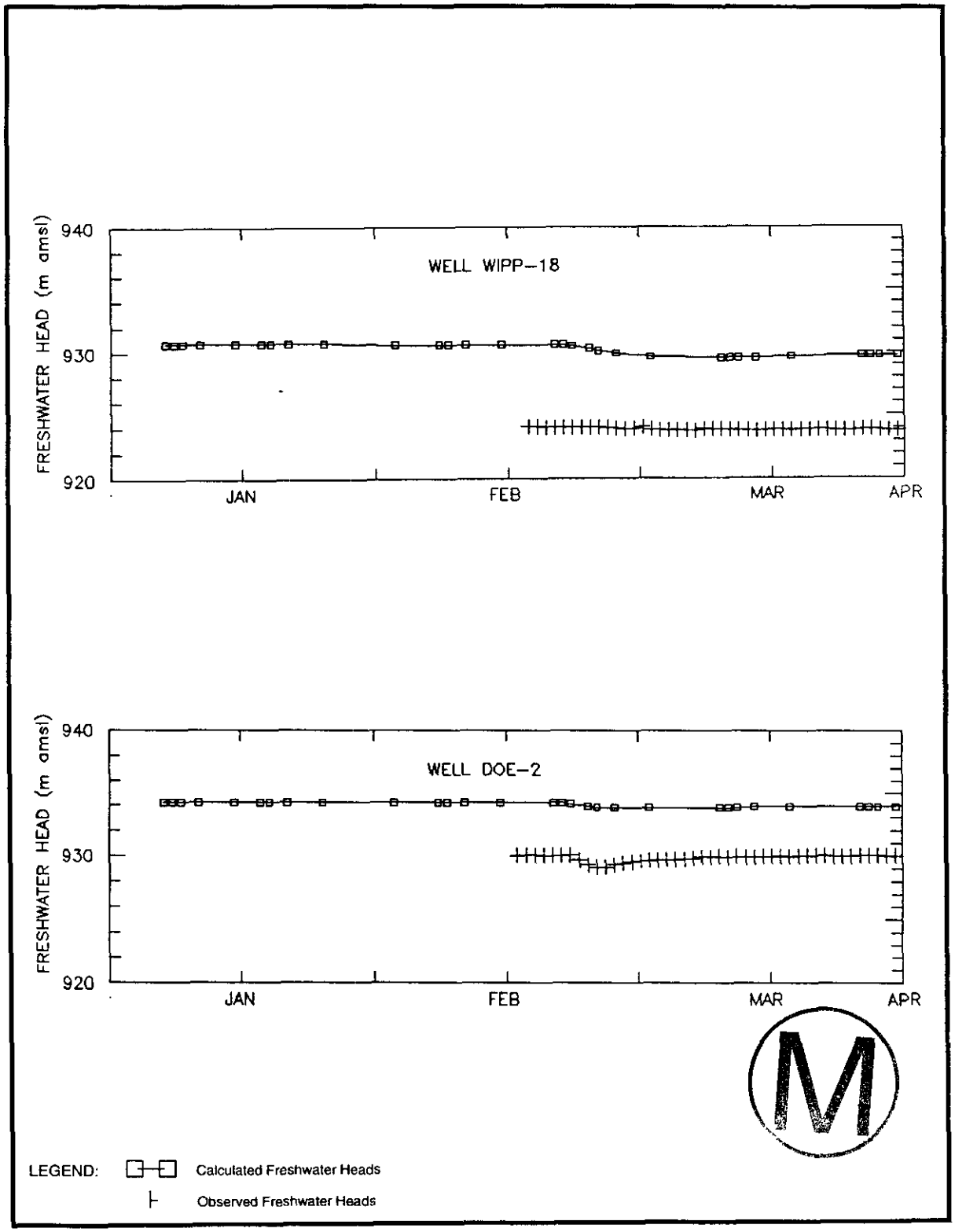

Figure TFIELD-42. Calculated and Measured Heads from 1995 to April 1996 at WIPP Boreholes WIPP-18 and DOE-2

1 **THIS PAGE INTENTIONALLY LEFT BLANK**

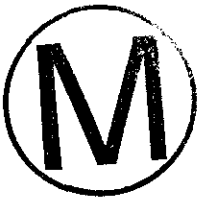

In general, the GRASP-INV code calibrated the CS transmissivity fields to the observed steady-state and transient heads better than in the LaVenue and RamaRao (1992) study. As mentioned above, the improved calibration is probably due to the increased flexibility of the code to optimize the properties independently for the higher transmissivity and lower transmissivity portions of the model.

TFIELD.5 Conclusions

Calibration of 100 CS transmissivity fields was successfully accomplished by the GRASP-INV code. The ability of the GRASP-INV code to optimize the properties of the areas associated with diagenetically altered (that is, higher) transmissivity and unaltered (that is, lower) transmissivity in the Culebra separately improved the capability of the model to obtain good agreement between the observed and calculated steady-state and transient heads (see also Chapter 2.0 and Appendix FAC for reasons why transmissivity varies). The 100 transmissivity fields incorporate the effects of variable elevation and variable fluid-density upon the flow fields and will be subsequently used by the SECOFL2D code to calculate groundwater travel times to the WIPP site boundary. The transmissivity fields generated in this study have a much higher variability than those produced in the 1992 performance assessment. This variability is due to a finer grid in the WIPP site area and to the simulation of the uncertain location of high transmissivity and low transmissivity zones within the model domain. These two conditions have produced higher transmissivities that are connected in a much more tortuous fashion than previously determined in the 1992 study.

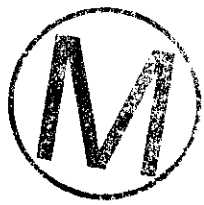

REFERENCES

Beauheim, R.L. 1986. *Hydraulic-Test Interpretations for Well DOE-2 at the Waste Isolation Pilot Plant (WIPP) Site*. SAND86-1364. Albuquerque, NM: Sandia National Laboratories. WPO 27656

Beauheim, R.L. 1987a. *Analysis of Pumping Tests of the Culebra Dolomite Conducted at the H-3 Hydropad at the Waste Isolation Pilot Plant (WIPP) Site*. SAND86-2311. Albuquerque, NM: Sandia National Laboratories. WPO 28468

Beauheim, R.L. 1987b. *Interpretation of the WIPP-13 Multipad Pumping Test of the Culebra Dolomite at the Waste Isolation Pilot Plant (WIPP) Site*. SAND87-2456. Albuquerque, NM: Sandia National Laboratories. WPO 28512

Beauheim, R.L. 1987c. *Interpretations of Single-Well Hydraulic Tests Conducted At and Near the Waste Isolation Pilot Plant (WIPP) Site, 1983-1987.* SAND87-0039. Albuquerque, NM: Sandia National Laboratories. WPO 27679

Beauheim, R.L. 1989. *Interpretation of H-11b4 Hydraulic Tests and the H-11 Multipad Pumping Test of the Culebra Dolomite at the Waste Isolation Pilot Plant (WIPP) Site.* SAND89-0536. Albuquerque, NM: Sandia National Laboratories. WPO 24154

Beauheim, R.L. 1996. "Culebra H-19 Hydraulic Test Analyses." Albuquerque, NM: Sandia National Laboratories. (Copy on file in the Sandia WIPP Central Files, Sandia National Laboratories, Albuquerque, NM as WPO 38401.)

Beauheim, R.L., T.F. Dale, and J.F. Pickens. 1991. *Interpretations of Single-Well Hydraulic Tests of the Rustler Formation Conducted in the Vicinity of the Waste Isolation Pilot Plant Site, 1988-1989.* SAND89-0869. Albuquerque, NM: Sandia National Laboratories. WPO 25862

Capilla, J.E., J.J. Gómez-Hernández, and A. Sahuquillo. 1992. "Conditioning of Transmissivity Fields to Piezometric Data." Presentation at INTRAVAL Meeting, San Antonio, TX, November, 1992. (Copy on file in the Sandia WIPP Central Files, Albuquerque, NM.)

Carrera J., and S.P. Neuman. 1986. Estimation of Aquifer Parameters Under Transient and Steady State Conditions, 2, Uniqueness, Stability, and Solution Algorithms, *Water Resources Research,* Vol. 22, No. 2, 211-227.

Cauffman, T.L., A.M. LaVenue, and J.P. McCord. 1990. *Ground-Water Flow Modeling of the Culebra Dolomite. Volume II: Data Base.* SAND89-7068/2. Albuquerque, NM: Sandia National Laboratories. WPO 10551

Certes, C., and G. de Marsily. 1991. Application of the Pilot Point Method to the Identification of Aquifer Transmissivities, *Advances in Water Resources*, Vol. 14, No. 5, 284-300.

Chapman, J.B., 1986. *Stable Isotopes in Southeastern New Mexico Groundwater: Implications for Dating Recharge in the WIPP Area. New Mexico Environmental Evaluation Group*, EEG-35. Santa Fe, NM: Environmental Evaluation Group. 76 p.

Chavent, G. 1971. Analyse fonctionnelle et identification de coefficients repartis des les equations aux derivees partielles. Doctoral dissertation. University of Paris. 158 p.

Cooper, J.B., 1962. *Ground-Water Investigations of the Project Gnome Area, Eddy and Lea Counties, New Mexico*. U.S. Geological Survey TEI-802, Open-File Report, 67 p., 17 Figures.

Cooper, J.B., and V.M. Glanzman. 1971. *Geohydrology of Project Gnome Site, Eddy County, New Mexico*. U.S. Geological Survey Professional Paper 712-A. Washington, DC: United States Government Printing Office. 24 p.

de Marsily, G., C. Lavedan, M. Boucher, and G. Fasanino. 1984. Interpretation of Interference Tests in a Well Field Using Geostatistical Techniques to Fit the Permeability Distribution in a Reservoir Model, in *Geostatistics for Natural Resources Characterization, Second NATO Advanced Study Institute, GEOSTAT 1983, Tahoe City, California*, edited by G. Verly, M. David, A.G. Journel, and A. Marechal, pp. 831-849, D. Reidel, Hingham, Mass.

Deutsch, C.V., and A.G. Journel. 1992. *GSLIB, Geostatistical Software Library and User's Guide*. New York: Oxford University Press.

EPA (Environmental Protection Agency). 1985. "40 CFR Part 191: Environmental Standards for the Management and Disposal of Spent Nuclear Fuel, High-Level and Transuranic Radioactive Wastes," *Federal Register*. Vol. 50, no. 182, 38066-38089. WPO 39132

Finley, N.C., and M. Reeves. 1981. *SWIFT Self-Teaching Curriculum: Illustrative Problems to Supplement the User's Manual for the Sandia Waste Isolation Flow and Transport Model (SWIFT)*. SAND81-0410, NUREG/CR-1968. Albuquerque, NM: Sandia National Laboratories. 69 p. (Available from the National Technical Information Service (NTIS), 555 Port Royal Road, Springfield, VA 22161, 703-487-4640 as NUREG/CR-1968.)

Gomez-Hernandez, J.J. and E.F. Cassiraga. 1994. *Theory and Practice of Sequential Simulation. Geostatistical Simulations*, Kluwer, Dordrecht, p. 111-134.

Gómez-Hernández, J.J., and X.-H. Wen. 1993. "Gaussian Optimism." Presentation at INTRAVAL Meeting, Berkeley, CA, March 15-16, 1993. (Copy on file in the Sandia WIPP Central Files, Sandia National Laboratories, Albuquerque, NM.)

Isaaks, E. and R. Srivastava. 1989. *An Introduction to Applied Geostatistics.* New York, NY: Oxford University Press. 578 p.

Journel, A.J., and Ch.J. Huijbregts. 1978. *Mining Geostatistics.* New York, NY: Academic Press. 610 p.

Keidser, A., and D. Rosbjerg. 1991. A Comparison of Four Inverse Approaches to Groundwater Flow and Transport Parameter Identification, *Water Resources Research,* Vol. 27, No. 9, 2219-2232.

Kennedy, W., Jr. and J. Gentle. 1980. *Statistical Computing.* New York, NY: Marcel Dekker, Inc. 591 p.

Lambert, S.J., 1987. *Feasibility Study: Applicability of Geochronologic Methods Involving Radiocarbon and Other Nuclides to the Groundwater Hydrology of the Rustler Formation. Sandia National Laboratories.* SAND86-1054. Albuquerque, NM: Sandia National Laboratories. WPO 24475

Lambert, S.J., and J.A. Carter. 1987. *Uranium-Isotope Systematics in Groundwaters of the Rustler Formation, Northern Delaware Basin, Southeastern New Mexico. I: Principles and Preliminary Results.* SAND87-0388. Albuquerque, NM: Sandia National Laboratories. WPO 24453

Lambert, S.J., and D.M. Harvey. 1987. *Stable-Isotope Geochemistry of Groundwaters in the Delaware Basin of Southeastern New Mexico.* SAND87-0138. Albuquerque, NM: Sandia National Laboratories. WPO 24150

Lappin, A.R. 1988. *Summary of Site-Characterization Studies Conducted From 1983 Through 1987 at the Waste Isolation Pilot Plant (WIPP) Site, Southeastern New Mexico.* SAND88-0157. Albuquerque, NM: Sandia National Laboratories. WPO 24945

LaVenue, A.M., and J.F. Pickens. 1992. Application of a Coupled Adjoint Sensitivity and Kriging Approach to Calibrate a Groundwater Flow Model, *Water Resources Research.* Vol. 28, No. 6, 1543-1569.

LaVenue, A.M., and B.S. RamaRao. 1992. *A Modeling Approach to Address Spatial Variability within the Culebra Dolomite Transmissivity Field.* SAND92-7306. Albuquerque, NM: Sandia National Laboratories. WPO 23889

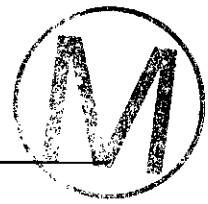

LaVenue, A.M., M. Reeves, and B.S. RamaRao. 1989. "An Application of Coupled Adjoint-Sensitivity and Kriging Techniques to Calibrate a Groundwater Flow Model in the Vicinity of a Nuclear Waste Repository," *Abstracts, 28th International Geological Congress, Washington, DC, July 9-19, 1989.* SAND88-7150A. Vol. 28, No. 2, 2-250 through 2-251. WPO 30106

Neuman, S.P. 1980. Adjoint-State Finite Element Equations for Parameter Estimation, *Finite Elements in Water Resources, Third International Conference, University of Mississippi, University, MS, May 1980.* Eds. S.Y. Wang, C.V. Alonso, C.A. Brebbia, W.G. Gray, and G.F. Pinder. University, MS: School of Engineering, University of Mississippi. 2:66 through 2:75.

Niou, S., and J. Pietz. 1987. "A Statistical Inverse Analysis of the H-3 Multipad Pumping Test." Prepared for Westinghouse Electric Corporation. Albuquerque, NM: International Technology Corporation. (Copy on file in the Sandia WIPP Central Files, Sandia National Laboratories, Albuquerque, NM as WPO 38864.)

Powers, D.W., S.J. Lambert, S-E. Shaffer, L.R. Hill, and W.D. Weart, eds. 1978. *Geological Characterization Report, Waste Isolation Pilot Plant (WIPP) Site, Southeastern New Mexico.* SAND78-1596. Albuquerque, NM: Sandia National Laboratories. Vols. 1-2. WPO 5448-Vol. 1, WPO 26829-26530 (Vol. 2)

RamaRao, B.S., and M. Reeves. 1990. *Theory and Verification for the GRASP II Code for Adjoint-Sensitivity Analysis of Steady-State and Transient Ground-Water Flow.* Contractor Rep. SAND89-7143J. Albuquerque, NM: Sandia National Laboratories. WPO 26000

Reeves, M., D.S. Ward, N.D. Johns, and R.M. Cranwell. 1986. *Theory and Implementation for SWIFT II, the Sandia Waste Isolation Flow and Transport Model, Release 4.84.* SAND83-1159 and NUREG/CR-3328. Albuquerque, NM: Sandia National Laboratories. WPO 28363

Reeves, M., D.S. Ward, P.A. Davis, and E.J. Bonano. 1987. *SWIFT II Self-Teaching Curriculum: Illustrative Problems for the Sandia Waste-Isolation Flow and Transport Model for Fractured Media.* SAND84-1586 and NUREG/CR-3925. Albuquerque, NM: Sandia National Laboratories.

Sykes, P.F., J.J. Wilson, and R.W. Andrews. 1985. Sensitivity Analysis for Steady State Groundwater Flow Using Adjoint Operators, *Water Resources Research,* Vol. 21, No. 3, 359-371.

Ward, D.S., M. Reeves, and L. E. Duda. 1984. *Verification and field comparison of the Sandia Waste-Isolation Flow and Transport Model (SWIFT).* SAND83-1154. Albuquerque, NM: Sandia National Laboratories. (NTIS available).

Wilson, J.L., B.S. RamaRao, and J.A. McNeish. 1986. *GRASP: A Computer Code to Perform Post-SWENT Adjoint Sensitivity Analysis of Steady-State Ground-Water Flow.* BMI/ONWI-625. Prepared for Office of Nuclear Waste Isolation. Columbus, OH: Battelle Memorial Institute.

WIPP Performance Assessment Department. 1992a. *Preliminary Performance Assessment for the Waste Isolation Pilot Plant, December 1992, Volume 1: Third Comparison with 40 CFR 191, Subpart B.* SAND92-0700/1. Albuquerque, NM: Sandia National Laboratories. WPO 20762

WIPP Performance Assessment Department. 1992b. *Preliminary Performance Assessment for the Waste Isolation Pilot Plant, December 1992, Volume 2: Third Comparison with 40 CFR 191, Subpart B.* SAND92-0700/2. Albuquerque, NM: Sandia National Laboratories. WPO 20805

Yeh, W. W-G. 1986. Review of Parameter Identification Procedures in Groundwater Hydrology: Inverse Problem, *Water Resources Research.* Vol. 22, No. 2, 95-108.

ATTACHMENTS

Attachment A: Calibrated Transmissivity Fields

Attachment B: WIPP Performance Assessment. User's Manual for GRASP-INV, Version 2.01. WPO 30636